

Boron Segregation in $\text{Si}_{1-x-y}\text{Ge}_x\text{C}_y$ and $\text{Si}_{1-y}\text{C}_y$ Alloys and
Application to P-Channel MOSFETs

Eric J. Stewart

A DISSERTATION
PRESENTED TO THE FACULTY
OF PRINCETON UNIVERSITY
IN CANDIDACY FOR THE DEGREE
OF DOCTOR OF PHILOSOPHY

RECOMMENDED FOR ACCEPTANCE
BY THE DEPARTMENT OF
ELECTRICAL ENGINEERING

JUNE 2004

© Copyright by Eric J. Stewart, 2004. All rights reserved.

Abstract

$\text{Si}_{1-x-y}\text{Ge}_x\text{C}_y$ alloys are of great interest for scaled Si-based devices. Adding germanium to silicon allows for the adjustment of both bandgap and strain, making possible devices such as the heterojunction bipolar transistor (HBT) and strained-Si MOSFET. Introducing small amounts of substitutional carbon can also adjust strain and bandgap, and has been shown to dramatically reduce the diffusion of boron and phosphorus atoms, allowing for increased control over dopant profiles. This has been important for the scaling of HBTs. Several factors, however, limit the usefulness of carbon, and many other issues remain unexplored. Carbon has a very low solubility in silicon and $\text{Si}_{1-x}\text{Ge}_x$ and can form undesirable silicon carbide (SiC) precipitates, degrading the properties of the films. Possible atomic interactions between carbon and other dopants during thermal processing are largely unknown, and may have important technological implications for diffusion and electrical properties. There has also been very little investigation of carbon in polycrystalline silicon films.

This work addresses several of these issues. First, a new application of $\text{Si}_{1-x-y}\text{Ge}_x\text{C}_y$ alloys for controlling dopant diffusion is presented, that of as a gate material for scaled p-channel MOSFETs. Devices with thin layers of polycrystalline $\text{Si}_{1-x-y}\text{Ge}_x\text{C}_y$ in the gate are shown to have increased threshold voltage stability vs. conventional devices and good electrical characteristics. Boron segregates to the polycrystalline $\text{Si}_{1-x-y}\text{Ge}_x\text{C}_y$ layers during post-implant anneals, reducing diffusion out of the gate and into the substrate. This new boron segregation effect is then examined in detail. Boron is found to segregate to both polycrystalline and single-crystal $\text{Si}_{1-x-y}\text{Ge}_x\text{C}_y$ and $\text{Si}_{1-y}\text{C}_y$ (no

germanium) during thermal anneals. Electrical measurements show no boron deactivation for low carbon concentrations, even with extensive annealing, indicating that inactive boron tied up with carbon-related defects is not driving the segregation. In addition, diffusion experiments indicate that boron is not becoming immobilized at carbon-related traps. Gradients of interstitial silicon, caused by substitutional carbon, are proposed as a driving force for the boron segregation. This hypothesis is supported by simulation results using coupled point defect-dopant diffusion models.

Acknowledgements

Thank you to all who helped make this thesis possible. First, to my advisor, Jim Sturm, for his exceptional amount of insight and support towards my thesis work. His excitement for research, unique ability to communicate difficult concepts to others in a fundamental way, and dedication to the development of his students, made him an excellent advisor. Thanks also to Prof. Lyon and Prof. Wagner for reviewing this thesis.

Many thanks to fellow students at Princeton, both past and present. The members of Sturm group created a very friendly lab environment, where everyone was always willing to be interrupted to help out each other. Thanks to all the RTCVD people – Haizhou Yin, Xiang-Zheng Bo, and Rebecca Peterson – for their camaraderie during many hours of searching for leaks, fixing burnboxes, etc. Special appreciation goes to Malcolm Carroll for all of his help with this thesis, and for countless discussions on a wide range of topics – in particular, for the ability to view almost every physics problem from a completely different angle as me, yet still enjoy the (often very long) process of working the problem out. Thanks to my parents, and all of my family, for their inspiration and encouragement over the years. And finally, to Bridget, for all of her support, and for filling my time at Princeton with so many good memories and, of course, pets.

Contents

Abstract	iii
1 Introduction	1
2 $\text{Si}_{1-x-y}\text{Ge}_x\text{C}_y$ and $\text{Si}_{1-y}\text{C}_y$ Alloys	4
2.1 Introduction	4
2.2 $\text{Si}_{1-x}\text{Ge}_x$ alloys	4
2.3 Carbon in silicon and $\text{Si}_{1-x}\text{Ge}_x$	9
2.4 $\text{Si}_{1-x-y}\text{Ge}_x\text{C}_y$ alloys	12
2.5 $\text{Si}_{1-y}\text{C}_y$ alloys	15
2.6 Growth of $\text{Si}_{1-x-y}\text{Ge}_x\text{C}_y$ and $\text{Si}_{1-y}\text{C}_y$ at Princeton	15
2.7 Summary	19
2.8 References	20
3 Suppression of Boron Penetration in P-Channel MOSFETs Using Polycrystalline $\text{Si}_{1-x-y}\text{Ge}_x\text{C}_y$ Gate Layers	22
3.1 Introduction	22
3.2 MOSFETs with undoped polycrystalline $\text{Si}_{1-x-y}\text{Ge}_x\text{C}_y$ gate layers	24
3.3 Mechanism of reduced boron penetration	33
3.3.1 Boron diffusion and segregation in polycrystalline $\text{Si}_{1-x-y}\text{Ge}_x\text{C}_y$..	33
3.3.2 Simulations of the effect of lower boron diffusivity in polycrystalline $\text{Si}_{1-x-y}\text{Ge}_x\text{C}_y$	36
3.3.3 MOSFETs with <i>in-situ</i> doped polycrystalline $\text{Si}_{1-x-y}\text{Ge}_x\text{C}_y$ gates	40
3.3.4 Proximity of polycrystalline $\text{Si}_{1-x-y}\text{Ge}_x\text{C}_y$ to gate oxide	44
3.3.5 Fluorine trapping	47

3.4 Summary	49
3.5 References	50
4 Boron Segregation and Electrical Properties in Polycrystalline Si_{1-x-y}Ge_xC_y and Si_{1-y}C_y	51
4.1 Introduction	51
4.2 Boron segregation in polycrystalline Si _{1-x-y} Ge _x C _y	52
4.3 Test for SIMS artifacts	58
4.4 Boron segregation in polycrystalline Si _{1-y} C _y (no Ge)	60
4.5 Electrical properties of boron-doped polycrystalline Si _{1-x-y} Ge _x C _y	63
4.5.1 Data	63
4.5.2 Discussion	66
4.6 Effect of segregation on the suppression of boron penetration in MOS structures	72
4.7 Summary	77
4.8 References	78
5 Boron Segregation and Driving Mechanisms in Single-Crystal Si_{1-x-y}Ge_xC_y and Si_{1-y}C_y	79
5.1 Introduction	79
5.2 Boron segregation to single-crystal Si _{1-x-y} Ge _x C _y	80
5.3 Boron segregation to single-crystal Si _{1-y} C _y	84
5.4 Potential mechanisms for boron segregation in Si _{1-x-y} Ge _x C _y alloys	87
5.4.1 Boron segregation to single-crystal Si _{1-x} Ge _x	87
5.4.2 Strain energy	87
5.4.3 Bandgap effects	89
5.4.4 Direct Ge-B interactions	90
5.4.5 Effect of slower boron diffusivity	90
5.4.6 Boron trapping at carbon-related defects	96

5.5	Electrical properties of single-crystal boron-doped $\text{Si}_{1-x-y}\text{Ge}_x\text{C}_y$ and $\text{Si}_{1-y}\text{C}_y$	97
5.6	Reversibility of boron segregation	101
5.7	Effect of boron on carbon diffusion	104
5.8	Summary	107
5.9	References	109
6	Interstitial-Gradient Driven Segregation to $\text{Si}_{1-x-y}\text{Ge}_x\text{C}_y$ and $\text{Si}_{1-y}\text{C}_y$ Alloys	110
6.1	Introduction	110
6.2	Carbon diffusion in crystalline silicon	111
6.2.1	Diffusion by interstitial mechanism	111
6.2.2	Substitutional carbon as a silicon interstitial sink	115
6.3	Modeling of the coupled diffusion of carbon and silicon interstitials	116
6.4	Boron diffusion in silicon	121
6.4.1	Diffusion by interstitial mechanism	121
6.4.2	Boron segregation to regions of low interstitial concentration ..	123
6.5	Modeling of boron segregation due to interstitial gradients	124
6.5.1	Test structure for simulations	124
6.5.2	Comparison of simulation with data	128
6.6	Relevance of interstitial gradient models for boron segregation in polycrystalline layers	131
6.7	Summary	132
6.8	References	134
7	Conclusion	135
7.1	Summary	135
7.2	Future work	136

Appendix A: Growth conditions for alloy layers used in this thesis	138
Appendix B: Sample RTCVD growth sequences	139
Appendix C: Publications and presentations resulting from this thesis	150

List of Figures

2.1	Lattice constant of $\text{Si}_{1-x}\text{Ge}_x$ alloys as a function of germanium fraction	5
2.2	Illustration of lattice configurations of $\text{Si}_{1-x}\text{Ge}_x$ alloys grown on silicon	7
2.3	Band alignment of $\text{Si}_{1-x}\text{Ge}_x$ and $\text{Si}_{1-x-y}\text{Ge}_x\text{C}_y$ alloys grown on silicon.	8
2.4	Dependence of substitutional carbon incorporation on growth conditions	11
2.5	Reduced boron diffusion in $\text{Si}_{1-x-y}\text{Ge}_x\text{C}_y$ compared to $\text{Si}_{1-x}\text{Ge}_x$	14
2.6	Bandgap alignment and reduced boron diffusion in $\text{Si}_{1-y}\text{C}_y$ compared to silicon .	16
2.7	Schematic of Princeton Rapid Thermal Chemical Vapor Deposition Reactor . . .	17
3.1	Illustration of boron penetration problem in p-channel MOSFETs	23
3.2	Threshold voltage stability of polycrystalline $\text{Si}/\text{Si}_{1-x-y}\text{Ge}_x\text{C}_y$ -gated MOSFETs .	26
3.3	I_D - V_D plot for polycrystalline $\text{Si}/\text{Si}_{1-x-y}\text{Ge}_x\text{C}_y$ gate device	28
3.4	Comparison of subthreshold characteristics.	29
3.5	Comparison of effective mobility as a function of anneal time.	30
3.6	Comparison of effective mobility as a function of gate voltage.	32
3.7	Boron profiles in the gates after 20-minute anneal.	34
3.8	Boron profiles in the gates after 100-minute anneal.	35
3.9	Simulations of threshold voltage vs. anneal time including fluorine effects . . .	38
3.10	Simulated effect of reduced boron diffusivity on threshold voltage stability . . .	39
3.11	Threshold voltage stability of <i>in-situ</i> doped polycrystalline $\text{Si}_{1-x-y}\text{Ge}_x\text{C}_y$ gates .	42
3.12	Subthreshold characteristics for <i>in-situ</i> doped gates.	43
3.13	Threshold voltage stability for polycrystalline $\text{Si}/\text{Si}_{1-x-y}\text{Ge}_x\text{C}_y/\text{Si}$ gate structures .	45
3.14	Carbon profiles in polycrystalline $\text{Si}/\text{Si}_{1-x-y}\text{Ge}_x\text{C}_y/\text{Si}$ gate structures	46
3.15	Fluorine profiles in the polycrystalline $\text{Si}/\text{Si}_{1-x-y}\text{Ge}_x\text{C}_y$ gate structure	48
4.1	Boron segregation to polycrystalline $\text{Si}_{1-x-y}\text{Ge}_x\text{C}_y$	54
4.2	Boron segregation in multi-layer polycrystalline $\text{Si}/\text{Si}_{1-x-y}\text{Ge}_x\text{C}_y$ structure	56
4.3	Dependence of segregation on carbon content and temperature	57
4.4	Boron profiles in structures to test for SIMS artifacts	59
4.5	Boron segregation to polycrystalline $\text{Si}_{1-y}\text{C}_y$	61
4.6	Enhanced carbon diffusion in polycrystalline $\text{Si}_{1-y}\text{C}_y$	62
4.7	Dopant activation and mobility for as-grown polycrystalline $\text{Si}_{1-x-y}\text{Ge}_x\text{C}_y$	65
4.8	Electrical properties of polycrystalline $\text{Si}_{1-x-y}\text{Ge}_x\text{C}_y$ as a function of annealing .	67
4.9	Resistivity of polycrystalline $\text{Si}_{1-x-y}\text{Ge}_x\text{C}_y$ as a function of doping level	68
4.10	Simulation of the effect of segregation on threshold voltage stability	74
4.11	Simulated boron profiles in the gates with or without segregation	75
5.1	Structures used to study segregation to single-crystal $\text{Si}_{1-x-y}\text{Ge}_x\text{C}_y$	81
5.2	Boron segregation to single-crystal $\text{Si}_{1-x-y}\text{Ge}_x\text{C}_y$	83
5.3	Structure used to study segregation to single-crystal $\text{Si}_{1-y}\text{C}_y$	85
5.4	Boron segregation to single-crystal $\text{Si}_{1-y}\text{C}_y$	86
5.5	Summary of previous reports of boron segregation to single-crystal $\text{Si}_{1-x}\text{Ge}_x$. . .	88
5.6	Appearance of segregation to material with low diffusivity	91

5.7	Diffusion potentials for two materials with difference diffusivities	94
5.8	Sheet resistance of as-grown $\text{Si}_{1-x-y}\text{Ge}_x\text{C}_y$ and $\text{Si}_{1-y}\text{C}_y$ as a function as carbon . . .	98
5.9.	Sheet resistance of $\text{Si}_{1-x-y}\text{Ge}_x\text{C}_y$ and $\text{Si}_{1-y}\text{C}_y$ as a function of annealing	99
5.10	Reversibility of boron segregation to single-crystal $\text{Si}_{1-y}\text{C}_y$	103
5.11	Enhanced diffusion and precipitation of carbon in the presence of boron	105
5.12	Integrated carbon for different anneals as a function of boron	106
6.1	Illustration of interstitials and vacancies in a silicon lattice	112
6.2	Illustration of carbon diffusion by interstitialcy mechanism	114
6.3	Comparison of experimental and simulated carbon diffusion	120
6.4	Simulation of boron segregation to $\text{Si}_{1-y}\text{C}_y$ layers due to interstitial gradients . . .	126
6.5	Dependence of simulated boron segregation on anneal time	127
6.6	Comparison of experimental and simulated boron segregation for low carbon . .	129
6.7	Comparison of experimental and simulated boron segregation for high carbon .	130

Chapter 1: Introduction

The scaling of silicon-based semiconductor devices continues to drive increased performance and reduced cost for many applications including microprocessors and wireless communications. In many ways, the ability to fabricate smaller devices controls the scaling process. One critical area is that of dopant profiles - the ability to place a specific amount of impurity in one region of a device, and keep it there during the entire fabrication process. The most challenging examples include regions where very thin, heavily-doped layers must be created, such as the base of an n-p-n Heterojunction Bipolar Transistor (HBT) or the source/drain regions of Metal Oxide Semiconductor Field Effect Transistors (MOSFETs). After the creation of such profiles, high-temperature processing must often be done (such as an activation anneal following an implant) to complete the fabrication. During these steps dopant diffusion inevitably causes the profiles to broaden, making it extremely difficult to maintain the sharp profiles needed to achieve high-performance devices. In addition, many other steps essential to the fabrication process, such as ion-implantation and oxidation, are known to dramatically enhance the diffusion of impurities, making it additionally challenging to stop unwanted broadening.

One promising technique to overcome these limitations is through materials advancements - in particular, new materials that can be easily integrated into the silicon-based fabrication processes. It has been shown that by adding small amounts of carbon (~0.1-1.0%) to either silicon or $\text{Si}_{1-x}\text{Ge}_x$, the diffusivity of boron and phosphorus atoms can be reduced by orders of magnitude below normal levels. This provides a mechanism by which diffusion can be controlled without altering processing conditions. By adding

carbon to regions of a device where diffusion must be minimized, sharp profiles can be maintained even during high-temperature processing. This has been crucial in the continued scaling of high performance HBT's; other potential applications include MOSFET channels and source/drains.

Several factors, however, limit the usefulness of carbon. Carbon has a very low solubility in silicon and $\text{Si}_{1-x}\text{Ge}_x$ and is therefore unstable. High levels of substitutional carbon, needed for the desired effect of reduced dopant diffusion, can be lost during thermal annealing to undesirable $\beta\text{-SiC}$ precipitates. Carbon has also been shown to degrade the electrical properties of silicon and $\text{Si}_{1-x}\text{Ge}_x$ films in some cases. In addition, many effects of carbon are still not understood or have not been investigated. Possible atomic interactions between carbon and other dopants during thermal processing are largely unknown, and may have important technological implications, as it is essential that both the carbon and dopants remain on substitutional lattice sites and do not form defects. The exact mechanism by which carbon controls dopant diffusion, while a subject of many studies, is still not fully understood; in particular, whether carbon-dopant interactions are playing a role is not fully known. There has also been very little investigation of carbon in polycrystalline films.

This work addresses several of these issues. After a review of $\text{Si}_{1-x-y}\text{Ge}_x\text{C}_y$ and $\text{Si}_{1-y}\text{C}_y$ alloys (Chapter 2), a new application of $\text{Si}_{1-x-y}\text{Ge}_x\text{C}_y$ for controlling dopant diffusion is presented, that of as a gate material for p-channel MOSFETs (Chapter 3). Polycrystalline $\text{Si}_{1-x-y}\text{Ge}_x\text{C}_y$ gate layers are shown to substantially increase the threshold voltage stability of scaled devices, compared to all polysilicon-gate devices, by reducing boron diffusion from the gates. This serves as a motivation to investigate the effect of

carbon on the electrical properties of polycrystalline $\text{Si}_{1-x-y}\text{Ge}_x\text{C}_y$ and $\text{Si}_{1-y}\text{C}_y$ films (Chapter 4). A new effect, that of carbon-induced boron segregation into $\text{Si}_{1-x-y}\text{Ge}_x\text{C}_y$ and $\text{Si}_{1-y}\text{C}_y$ layers, is observed and characterized. In Chapter 5, a variety of methods are used to examine potential carbon-boron defect formation during thermal annealing, as a possible cause for this segregation. Finally, in Chapter 6, a new driving force for dopant segregation is presented, that of interstitial gradients. This is promising for technological applications, as it reveals that boron segregation into $\text{Si}_{1-x-y}\text{Ge}_x\text{C}_y$ can be explained from diffusion theory alone, without having to invoke carbon-related defect formation.

Chapter 2: $\text{Si}_{1-x-y}\text{Ge}_x\text{C}_y$ and $\text{Si}_{1-y}\text{C}_y$ Alloys

2.1 Introduction

In this chapter the properties, motivations, and methods of growth for $\text{Si}_{1-x-y}\text{Ge}_x\text{C}_y$ and $\text{Si}_{1-y}\text{C}_y$ alloys are reviewed. Since historically $\text{Si}_{1-x}\text{Ge}_x$ alloys were researched first and led to much of the work with carbon, these are first discussed. Then the properties of carbon in silicon, including its incorporation at high levels for $\text{Si}_{1-x-y}\text{Ge}_x\text{C}_y$ and $\text{Si}_{1-y}\text{C}_y$ alloys, and its effect on strain, bandgap, and diffusion, are reviewed. Finally, the growth of these alloys by the Rapid Thermal Chemical Vapor Deposition (RTCVD) technique at Princeton is described.

2.2 $\text{Si}_{1-x}\text{Ge}_x$ alloys

The ability to integrate $\text{Si}_{1-x}\text{Ge}_x$ alloys with silicon integrated circuit processing has enabled them to have a large impact on Si-based electronics. Silicon and germanium are isoelectronic, have the same crystalline lattice structure (diamond), and are completely miscible with each other (the fraction of germanium and silicon can be varied over the whole range). As a result, the properties of $\text{Si}_{1-x}\text{Ge}_x$ alloys can be varied between that of silicon and germanium by adjusting the germanium fraction x . For example, germanium has a larger lattice constant than silicon - 0.568 nm vs. 0.543 nm, respectively [1]. As a result, a $\text{Si}_{1-x}\text{Ge}_x$ alloy can be tailored to have a lattice constant in between these two, as shown in Figure 2.1. Similarly, the bandgap of a $\text{Si}_{1-x}\text{Ge}_x$ layer can

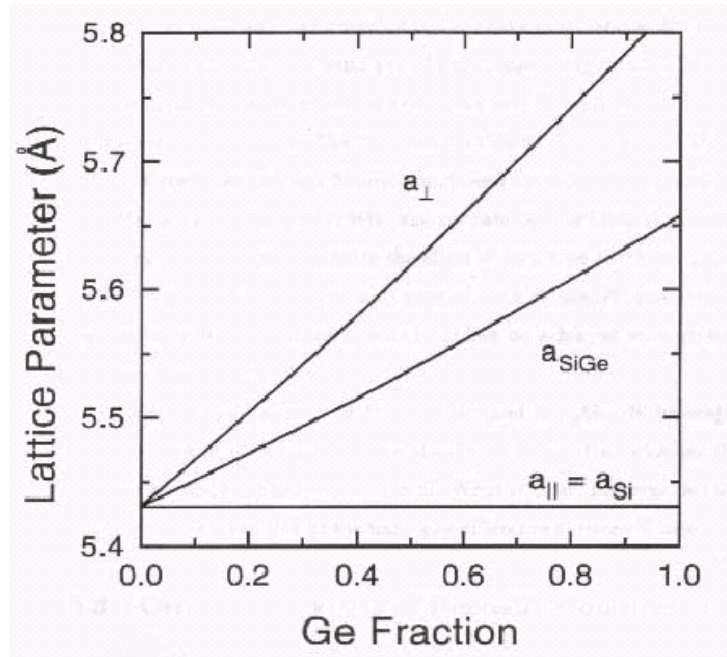


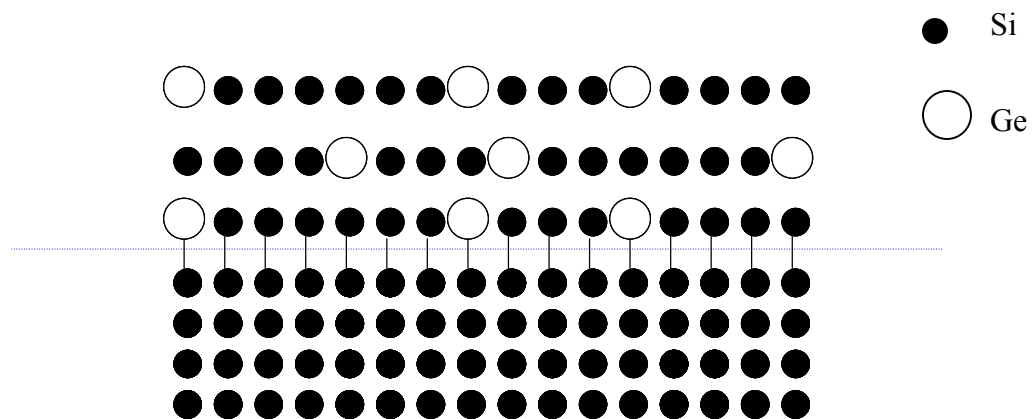
Figure 2.1: Lattice constant of relaxed $Si_{1-x}Ge_x$ alloys (a_{SiGe}), as well as the vertical (a_{\perp}) and horizontal ($a_{||}$) lattice constant for strained $Si_{1-x}Ge_x$ layers grown on silicon.

be adjusted between that of silicon (1.12 eV) and germanium (0.67 eV) [2, 3].

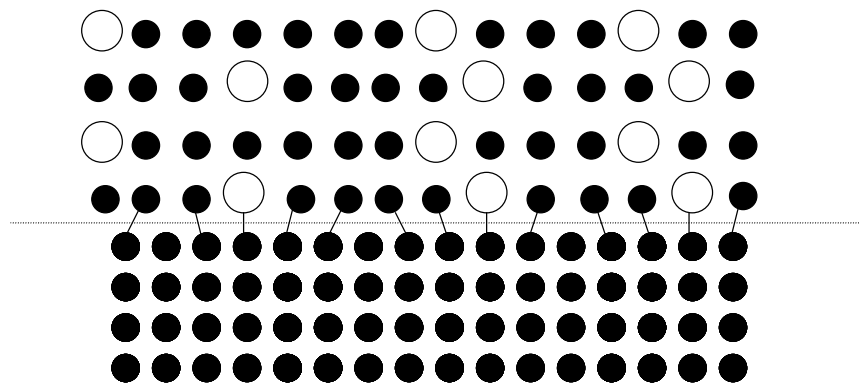
For typical device applications, layers of $\text{Si}_{1-x}\text{Ge}_x$ are grown epitaxially on silicon substrates. Due to the lattice mismatch, there are two ways that the $\text{Si}_{1-x}\text{Ge}_x$ layer can arrange itself, shown in Figure 2.2. If the thickness of the $\text{Si}_{1-x}\text{Ge}_x$ layer is small, the horizontal lattice constant will match to the silicon substrate, resulting in compressive strain in that direction (Figure 2.2(a)). The vertical lattice constant will increase. This is referred to as pseudomorphic growth. If the thickness of the layer exceeds a certain value (called the critical thickness, t_c), the strain energy will exceed the energy required to form misfit dislocations at the interface, and the layer will begin to relax towards its unstrained state (Figure 2.2(b)) [4]. The critical thickness becomes smaller as the strain, and hence germanium content, increases. This mode of growth is generally considered undesirable, as the defects will degrade the quality of the layer for device applications. However, if defects can be minimized, a relaxed $\text{Si}_{1-x}\text{Ge}_x$ layer can be useful substrate for certain device applications.

For pseudomorphic growth, the strain in the $\text{Si}_{1-x}\text{Ge}_x$ layer will alter its properties compared to relaxed $\text{Si}_{1-x}\text{Ge}_x$. For example, the bandgap is additionally reduced below its relaxed value. For relaxed $\text{Si}_{1-x}\text{Ge}_x$ layers, the bandgap decreases by ~ 4 meV per atomic percent germanium, for small germanium content ($<40\%$) [3]. However, for strained layers, the reduction is ~ 7 meV/at.% Ge [2]. The bandgap offset has been shown to be largely accommodated at the valence band, as shown in Figure 2.3. $\text{Si}_{1-x}\text{Ge}_x$ also has several other properties significant for device applications, such as a lower boron diffusion coefficient compared to silicon [5].

Historically, the most technologically important application of $\text{Si}_{1-x}\text{Ge}_x$ has been



(a)



(b)

Figure 2.2: Illustration of lattice configuration for $\text{Si}_{1-x}\text{Ge}_x$ alloys for (a) strained pseudomorphic growth, and (b) relaxed growth containing misfit dislocations at the interface.

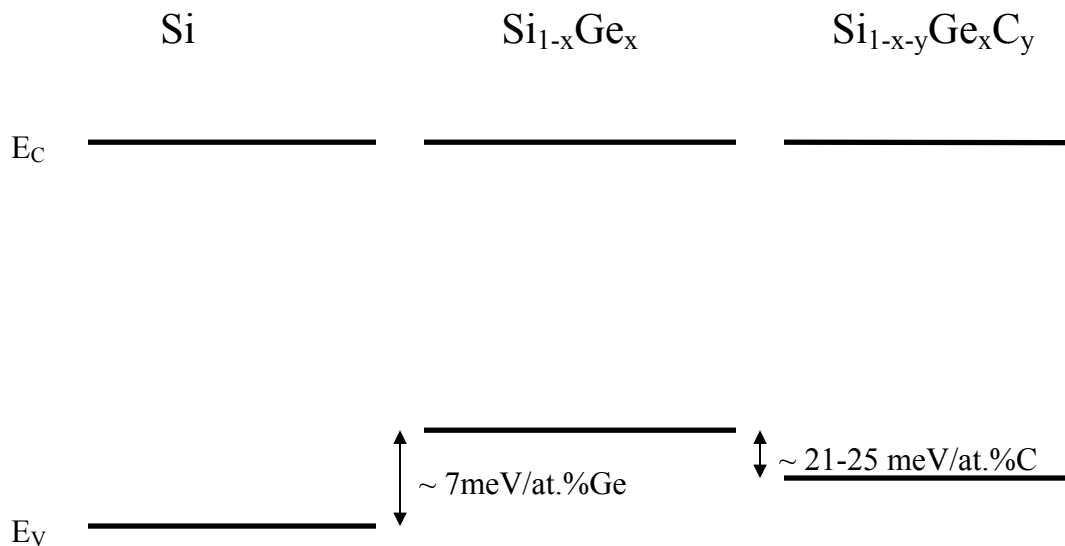


Figure 2.3: Band alignment of pseudomorphic $\text{Si}_{1-x}\text{Ge}_x$ and $\text{Si}_{1-x-y}\text{Ge}_x\text{C}_y$ alloys grown on (100) silicon substrates, with low Ge content ($x < 0.4$), compared to silicon. The conduction band offsets are considered to be negligible. It is also assumed that the $\text{Si}_{1-x-y}\text{Ge}_x\text{C}_y$ layers are still in compression, that is, that the Ge/C ratio is less than 10.

as a strained p-type base for a Heterojunction Bipolar Transistor (HBT) [7]. The bandgap offset in the $\text{Si}_{1-x}\text{Ge}_x$ base layer allows for a higher gain in the device, which can be traded off for heavier base doping, reduced emitter doping, or a graded base structure with a built-in field. $\text{Si}/\text{Si}_{1-x}\text{Ge}_x/\text{Si}$ HBTs are currently being manufactured with far superior performance compared to their silicon counterparts. More recently, relaxed $\text{Si}_{1-x}\text{Ge}_x$ layers are being used as substrates for the growth of tensile-strained silicon layers. Tensile-strained silicon can have enhanced mobilities (compared to relaxed silicon), and is being considered as a channel material to increase the drive currents of MOSFETs [8]. Other potential applications include using the $\text{Si}_{1-x}\text{Ge}_x$ layer itself in MOSFET channels or source/drains.

Polycrystalline $\text{Si}_{1-x}\text{Ge}_x$ has also been studied for use as a MOSFET gate [9]. Boron-doped polycrystalline $\text{Si}_{1-x}\text{Ge}_x$ layers are known to have lower resistivity than polysilicon, due to both a larger grain size and reduced carrier trapping at grain boundaries [10]. MOSFETs with polycrystalline $\text{Si}_{1-x}\text{Ge}_x$ gates have reduced gate depletion effects compared to conventional polysilicon-gated devices. In addition, the ability to tailor the work function by adjusting the germanium fraction also allows for the adjustment of threshold voltage. Polycrystalline $\text{Si}_{1-x}\text{Ge}_x$ has also been investigated for thin-film transistor applications [11].

2.3 Carbon in silicon and $\text{Si}_{1-x}\text{Ge}_x$

Carbon is isoelectronic to silicon and germanium, and can crystallize in a diamond structure. The bandgap of carbon is much larger (5.5 eV) and the lattice

constant much smaller (0.355 nm) than either silicon or germanium. However, carbon is not completely miscible with silicon in the same manner as germanium. In fact, the solid solubilities of substitutional carbon at the melting temperature in silicon ($\sim 3 \times 10^{17} \text{ cm}^{-3}$) and germanium ($\sim 10^8 - 10^9 \text{ cm}^{-3}$) are both very low [12, 13]. At higher concentrations, the thermodynamically stable state for carbon mixed with silicon is silicon carbide (SiC).

Over the past decade or so, however, growth techniques have been developed to incorporate carbon on substitutional silicon lattice sites well above its solubility limit, not in the SiC phase. In this case the layers are referred to as $\text{Si}_{1-y}\text{C}_y$ or $\text{Si}_{1-x-y}\text{Ge}_x\text{C}_y$, with y denoting the carbon fraction. These growth techniques typically rely on a low deposition temperature and high growth rate, taking advantage of the enhanced surface solubility of carbon [14]. Both Chemical Vapor Deposition (CVD) and Molecular Beam Epitaxy (MBE) have been used, with typical deposition temperatures ranging from 525-625°C for CVD and 400-500°C for MBE, and growth rates of $\sim 5-10 \text{ nm/min}$ [15,16]. Substitutional carbon concentrations as high as 2.5% have been successfully incorporated. These layers are metastable, however, and if subjected to long thermal annealing carbon can come out of substitutional lattice sites and into more energetically favorable SiC precipitates [17, 18].

The fraction of carbon incorporated substitutionally in silicon and $\text{Si}_{1-x}\text{Ge}_x$ films can be measured using X-ray diffraction (XRD) and Fourier Transform Infrared Spectroscopy (FTIR) measurements, which detect the difference in strain caused by the

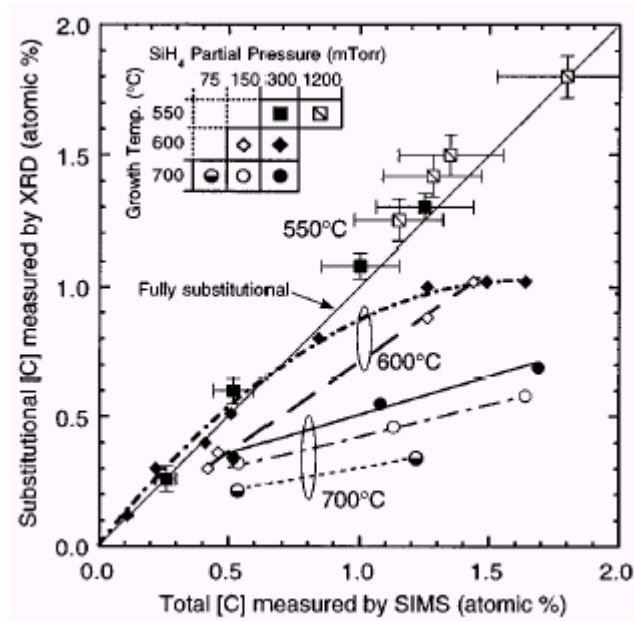


Figure 2.4: Substitutional carbon content (measured by XRD) vs. total carbon content (measured by SIMS) for $\text{Si}_{1-y}\text{C}_y$ films grown by Chemical Vapor Deposition at different temperatures and SiH_4 partial pressures. From reference [15].

carbon (discussed in next section), and the presence of substitutional carbon bonding, respectively. Figure 2.4 shows substitutional carbon concentration (measured by XRD) as a function of total carbon (measured by SIMS) for $\text{Si}_{1-y}\text{C}_y$ layers grown at different temperatures and pressures by CVD [15]. As can be seen, low temperature growth is very important to obtain high fractions of substitutional carbon. Most of the work in this thesis is based on recipes developed at Princeton to incorporate substitutional carbon in the 0.1-1.0% range [16, 29].

2.4 $\text{Si}_{1-x-y}\text{Ge}_x\text{C}_y$ alloys

When substitutional carbon is added to $\text{Si}_{1-x}\text{Ge}_x$, its small size will reduce the average lattice constant of the alloy, counteracting the effect of the germanium. This reduces the lattice mismatch to silicon, and hence the strain of a pseudomorphic layer. This is useful, as the critical thickness of the layer, for a given germanium content, will be increased by adding carbon. One carbon atom has been experimentally observed to compensate the strain of ~8-12 germanium atoms [19, 20]. As a result, for example, a $\text{Si}_{1-x-y}\text{Ge}_x\text{C}_y$ alloy with 20% germanium and 2% carbon will be approximately lattice matched to silicon and macroscopically strain-free.

Carbon also alters the bandgap of $\text{Si}_{1-x}\text{Ge}_x$. In strained layers, most reports show that carbon increases the bandgap by ~ 21-25 meV/at.%C, mostly by lowering the valence band [21, 22] (Figure 2.3). This increase can be partially explained by the carbon compensating strain. However, if only the effect of strain on the bandgap is considered, carbon would be expected to increase the bandgap closer to ~ 45 meV/at.%C, more than

is seen experimentally. As a result, it appears that the intrinsic effect of carbon (not considering its effect on strain) is to *decrease* the bandgap by ~ 20 meV/at.%C.

Most significantly for this work, high levels of substitutional carbon (0.1-1.0%) have been shown to dramatically reduce the diffusivity of the technologically important dopants boron and phosphorus [23]. Figure 2.5 shows the diffusivity of boron in a $\text{Si}_{1-x-y}\text{Ge}_x\text{C}_y$ layer compared to $\text{Si}_{1-x}\text{Ge}_x$ when subjected to thermal annealing in N_2 at temperatures between 800-950°C. Note the 8X reduction over $\text{Si}_{1-x}\text{Ge}_x$ at 850°C. In addition, $\text{Si}_{1-x-y}\text{Ge}_x\text{C}_y$ has also been shown to be effective at reducing the enhanced dopant diffusion due to oxidation and the transient enhanced diffusion which occurs after ion-implantation, as well as reducing diffusion in regions nearby (not inside) the $\text{Si}_{1-x-y}\text{Ge}_x\text{C}_y$ layer itself [24]. This is related to the mechanism by which carbon reduces dopant diffusion, through the sinking of silicon interstitials (which boron and phosphorus depend on to diffuse). A full discussion of the mechanism by which carbon reduces dopant diffusion is deferred until Chapter 6.

The most important technological application so far of $\text{Si}_{1-x-y}\text{Ge}_x\text{C}_y$ has been as a base for an npn HBT [25]. Despite the reduction of boron diffusivity in $\text{Si}_{1-x}\text{Ge}_x$, npn HBTs with $\text{Si}_{1-x}\text{Ge}_x$ bases still suffer from undesirable boron out-diffusion during processing, resulting in performance degradations. $\text{Si}_{1-x-y}\text{Ge}_x\text{C}_y$ can almost completely eliminate the boron out-diffusion from the base, resulting in greater device performance for the same processing conditions. As a result, the $\text{Si}_{1-x-y}\text{Ge}_x\text{C}_y$ base has been very important for the continued scaling of HBT devices. $\text{Si}_{1-x-y}\text{Ge}_x\text{C}_y$ has also been investigated for use in MOSFET channels and source/drains [26, 27].

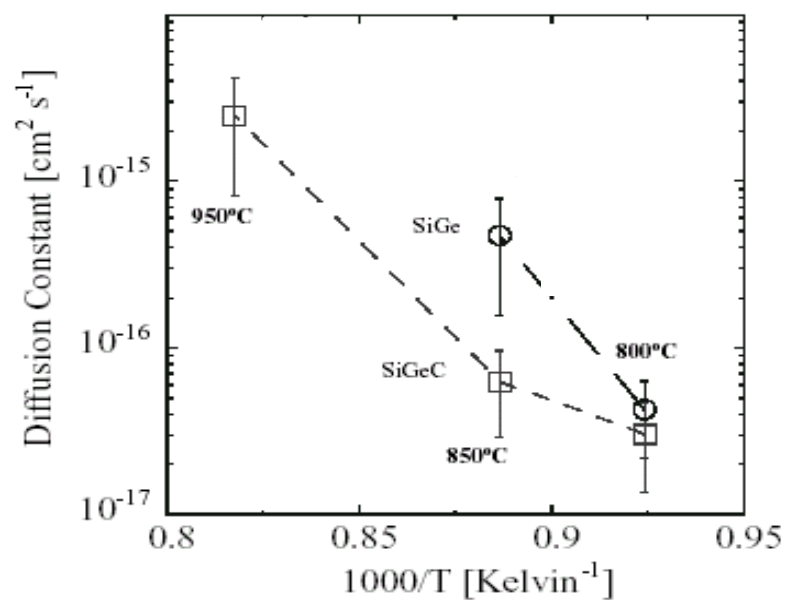


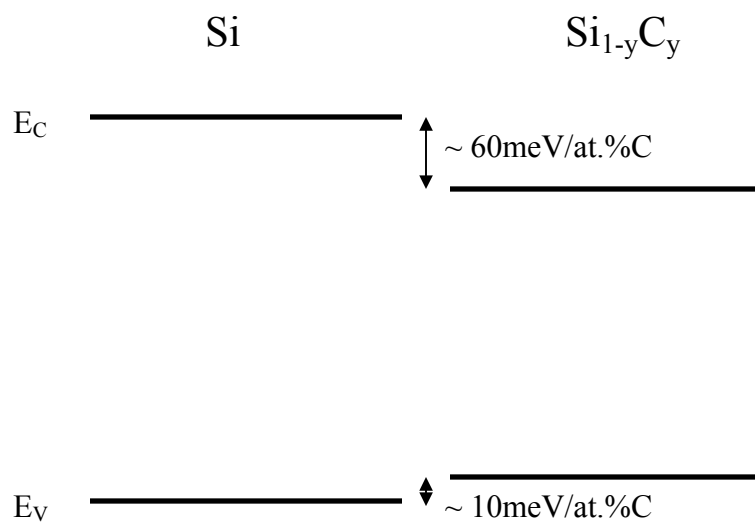
Figure 2.5: Reduced diffusivity of boron in $\text{Si}_{0.795}\text{Ge}_{0.2}\text{C}_{0.005}$ compared to $\text{Si}_{0.8}\text{Ge}_{0.2}$ during 15-minute furnace anneals in N_2 at temperatures between 800-950°C. From reference [23].

2.5 $\text{Si}_{1-y}\text{C}_y$ alloys

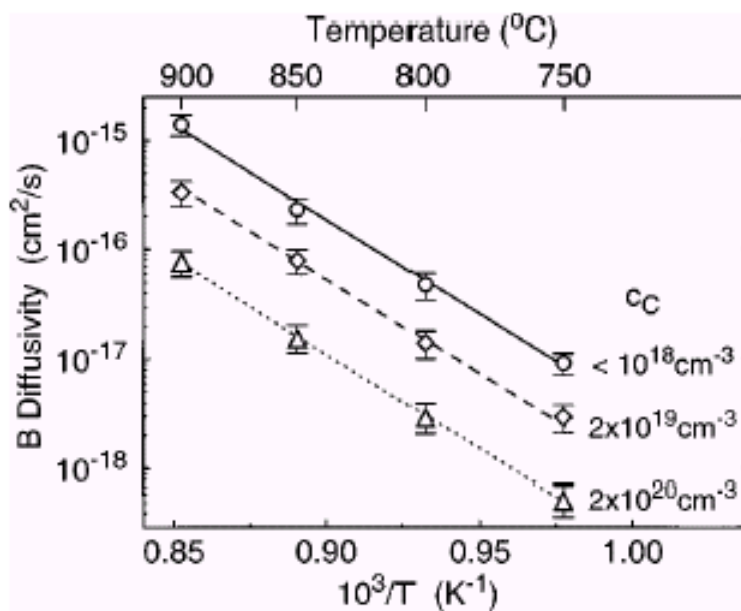
When carbon is added to silicon, the overall lattice constant is reduced. As a result, when a pseudomorphic $\text{Si}_{1-y}\text{C}_y$ layer is grown on silicon (below critical thickness), the layer will be stretched in the horizontal direction, or under macroscopic tensile strain. This tensile strain will also affect the bandgap. The bandgap for a $\text{Si}_{1-y}\text{C}_y$ layer compared to silicon is illustrated in Figure 2.6(a), with offsets in both the conduction and valence band. $\text{Si}_{1-y}\text{C}_y$ alloys have also been shown to dramatically reduce boron diffusion, similar to $\text{Si}_{1-x-y}\text{Ge}_x\text{C}_y$ [28]. Figure 2.6(b) shows the diffusivity as a function of temperature and carbon content. Similar to Figure 2.5, adding 0.4% substitutional carbon can reduce the boron diffusivity by more than an order of magnitude. $\text{Si}_{1-y}\text{C}_y$ alloys have also been considered for use in n-MOSFET channels, as it is known that tensile strain may enhance the mobility. However, decreases in mobility due to carbon-related scattering may cancel any improvement from the strain [29].

2.6 Growth of $\text{Si}_{1-x-y}\text{Ge}_x\text{C}_y$ and $\text{Si}_{1-y}\text{C}_y$ at Princeton

All of the structures and devices containing $\text{Si}_{1-x-y}\text{Ge}_x\text{C}_y$ and $\text{Si}_{1-y}\text{C}_y$ in this work were grown by Rapid Thermal Chemical Vapor Deposition (RTCVD) at Princeton. Figure 2.7 shows a schematic of the Princeton reactor. The growth chamber consists of a vacuum-sealed quartz tube surrounded by a reflector box, inside of which is a bank of tungsten-halogen lamps. The wafer sits on a quartz stand inside the chamber. Radiation



(a)



(b)

Figure 2.6: (a) Bandgap alignment [29] and (b) reduced boron diffusivity [28] as a function of temperature and carbon content (C_C), for tensile-strained $\text{Si}_{1-y}\text{C}_y$ alloys.

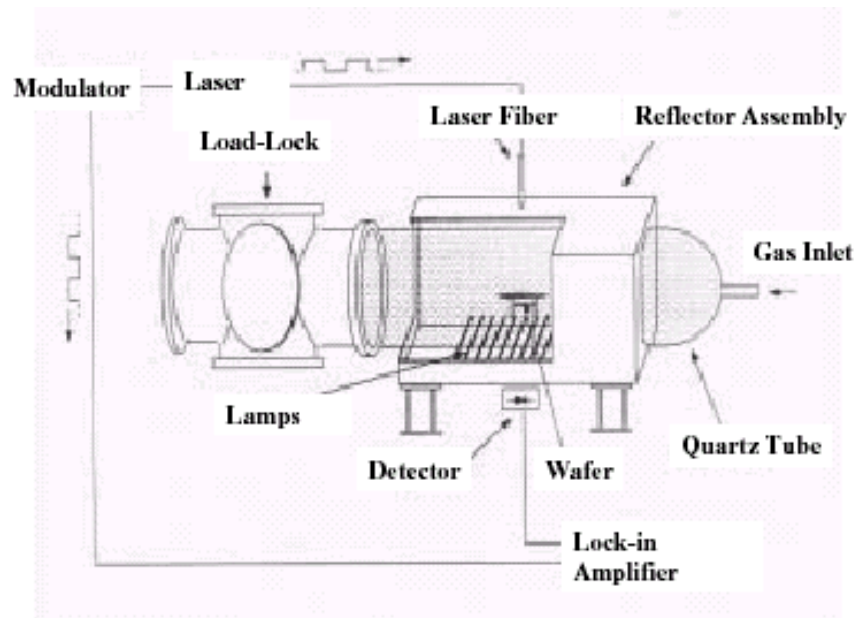


Figure 2.7: Schematic of the Princeton Rapid Thermal Chemical Vapor Deposition (RTCVD) reactor. From reference [30].

from the lamps is absorbed directly by the wafer causes the wafer heating. The temperature of the wafer is extracted by measuring the absorbance of 1.3 and 1.55 μm laser light being shined through the wafer and detected at the bottom of the reflector box [31]. Using a feedback control loop, the power of the lamps is adjusted to obtain the desired temperature. Source gases are injected from the right side of the diagram and pumped out on the left, and pressure is controlled using a butterfly valve and a pressure sensor in the chamber for feedback control.

For a standard epitaxial growth run, a 4" silicon wafer is first wet-chemically cleaned using a [3:1] $\text{H}_2\text{SO}_4/\text{H}_2\text{O}_2$ soak, followed by a \sim [50:1] deionized water/HF dip. After a N_2 blow dry, it is then directly placed on the quartz stand in the load lock of the reactor. After purging the load lock several times with high purity N_2 , the quartz stand and wafer are loaded into the main chamber and sealed off from the load lock. Hydrogen is injected at 3 lpm, the temperature is ramped up to $\sim 1000^\circ\text{C}$, and the pressure increased to 250 Torr for 2 minutes to desorb any SiO_2 from the wafer surface. After this bake step, the pressure is reduced to 6 Torr, and dichlorosilane injected at 26 sccm for 5 minutes to grow a thick ($\sim 500\text{nm}$) silicon buffer layer. At this point, silicon, $\text{Si}_{1-x}\text{Ge}_x$, $\text{Si}_{1-x-y}\text{Ge}_x\text{C}_y$, and $\text{Si}_{1-y}\text{C}_y$ alloys are deposited, at temperatures ranging (in this work) from $575\text{-}750^\circ\text{C}$. The silicon growth was done using silane or dichlorosilane at 700 or 750°C , respectively. Deposition of $\text{Si}_{1-x}\text{Ge}_x$ and $\text{Si}_{1-x-y}\text{Ge}_x\text{C}_y$ layers was performed at 625°C , also using silane or dichlorosilane as silicon sources, and germane, methysilane, and diborane as sources for germanium, carbon, and boron, respectively. $\text{Si}_{1-y}\text{C}_y$ layers were grown at 625°C but using disilane as a silicon source. For polycrystalline material, layers were grown on oxidized silicon wafers using the same recipes but without buffer layers, and

sometimes without the high-temperature bake as well. A summary of the growth conditions for several important recipes used in this work is provided in Appendix A, and is referred to where appropriate in the rest of this thesis.

2.7 Summary

In summary, the growth, properties, and applications of $\text{Si}_{1-x-y}\text{Ge}_x\text{C}_y$ alloys were reviewed. $\text{Si}_{1-x-y}\text{Ge}_x\text{C}_y$ alloys are of great interest for their ability to control dopant profiles in silicon-based devices, through the effect of substitutional carbon on boron and phosphorus diffusion. Low temperature growth is important for the incorporation of high levels of substitutional carbon. However, many aspects of carbon-containing films important for technological applications, such as the interaction of carbon with dopants, its effect on the electrical properties of both single-crystal and polycrystalline layers, and a full understanding of dopant diffusion and segregation, are not well understood. In the next chapter, a new application for $\text{Si}_{1-x-y}\text{Ge}_x\text{C}_y$, as a gate material for p-channel MOSFETs, is demonstrated. The following chapters then investigate a number of the above issues to gain a greater fundamental knowledge of $\text{Si}_{1-x-y}\text{Ge}_x\text{C}_y$ and $\text{Si}_{1-y}\text{C}_y$, so we can understand their potential uses for gates and other applications.

2.8 References

- [1] J. Dismukes, L. Ekstrom, and R. Paff, *Journal of Physical Chemistry*, vol. 68, p. 3021 (1964).
- [2] D.V. Lang, R. People, J.C. Bean, and A.M. Sergent, *Applied Physics Letters*, vol. 47(12), p. 1333-1335 (1985).
- [3] R. Braunstein, A. Moore, and F. Herman, *Physical Review*, vol. 109, p. 695 (1958).
- [4] C. Van de Walle and R. Martin, *Physical Review B*, vol. 34, p. 5621 (1986).
- [5] P. Kuo, J.L. Hoyt, J.F. Gibbons, J.E. Turner, R.D. Jacowitz, and T.I. Kamins, *Applied Physics Letters*, vol. 62(6), p. 612-614 (1993).
- [6] J.P. Liu and H.J. Osten, *Applied Physics Letters*, vol. 76, p. 3546 (2000).
- [7] J.C. Sturm, R.V. Schwartz, E.J. Prinz, and H. Manoharan, *Journal of Vacuum Science and Technology B*, vol. 9, p. 2011 (1991).
- [8] K. Rim, J.L. Hoyt, and J.F. Gibbons, *IEEE Transactions on Electron Devices*, vol. 47(7), p. 1406-1415 (2000).
- [9] C. Salm, D.T. van Veen, D.J. Gravesteijn, J. Holleman, and P.H. Woerlee, *Journal of the Electrochemical Society*, vol. 144 (10), p. 3665-3673 (1997).
- [10] T.J. King, J.P. McVittie, K.C. Saraswat, and J.R. Pfiester, *IEEE Transactions on Electron Devices*, vol. 41(2), p. 228-232 (1994).
- [11] T.J. King and K.C. Saraswat, *Tech. Dig. Int. Electron Device Meeting*, p. 567-570 (1991).
- [12] G. Davies and R.C. Newmann, "Carbon in Monocrystalline Silicon", in *Handbook on Semiconductors*, T.S. Moss, Ed., 1994, p. 1558.
- [13] R.I. Space and G.A. Slack, *Journal of Chemical Physics*, vol. 30, p. 1551 (1959).
- [14] J. Tersoff, *Physical Review Letters*, vol. 74, p. 5080 (1995).
- [15] T.O. Mitchell, J.L. Hoyt, and J.F. Gibbons, *Applied Physics Letters*, vol. 71, p. 1688 (1997).
- [16] C.W. Liu, A. St. Amour, J.C. Sturm, Y.R.J. Lacroix, M.L.W. Thewalt, C.W. Magee, and D. Eaglesham, *Journal of Applied Physics* **80**, 3043 (1996).
- [17] L.V. Kulik, D.A. Hits, M.W. Dashiell, and J. Kolodzey, *Applied Physics Letters*, vol. 72(16), p. 1972-1974 (1998).
- [18] P. Warren, J. Mi, F. Overney, and M. Dutoit, *Journal of Crystal Growth*, vol. 157, p. 414-419 (1995).
- [19] S.C. Jain, H.J. Osten, B. Dietrich, and H. Ruecker, *Semiconductor Science and Technology*, vol. 10, p. 1289 (1995).
- [20] J.L. Hoyt, T.O. Mitchell, K. Rim, V. Singh, and J.F. Gibbons, *Thin Solid Films*, vol. 10, p. 1289 (1995).
- [21] A. St. Amour, C.W. Liu, J.C. Sturm, Y. Lacroix, and M.L.W. Thewalt, *Applied Physics Letters*, vol. 67(26), p. 3915-3917 (1995).
- [22] C.L. Chang, L.P. Rokhinson, and J.C. Sturm, *Applied Physics Letters*, vol. 73(24), p. 3568-3570 (1998).
- [23] M.S. Carroll, L.D. Lanzerotti, and J.C. Sturm, *MRS Symp. Proc.* **527**, 417 (1998).
- [24] M.S. Carroll, C.L. Chang, J.C. Sturm, and T. Buyuklimanli, *Applied Physics Letter*, vol. 73(25), p. 3695 (1998).

- [25] L.D. Lanzerotti, J.C. Sturm, E. Stach, and R. Hull, T. Buyuklimanli, and C. Magee, *Applied Physics Letters*, vol. 70(23), p. 3125-3127 (1997).
- [26] I. Ban, M.C. Ozturk, and E.K. Demirlioglu, *IEEE Transactions on Electron Devices*, vol. 44(9), p. 1544-1551 (1997).
- [27] M. Yang, C.L. Chang, M.S. Carroll, and J.C. Sturm, *IEEE Electron Device Letters*, vol. 20(6), p. 301-303 (1999).
- [28] H. Rucker, B. Heinemann, W. Ropke, R. Kurps, D. Kruger, G. Lippert, and H.J. Osten, *Applied Physics Letters*, vol. 73 (12), p. 1682-1684 (1998).
- [29] J.L. Hoyt, "Substitutional Carbon Incorporation and Electronic Characterization of $\text{Si}_{1-y}\text{C}_y/\text{Si}$ and $\text{Si}_{1-x-y}\text{Ge}_x\text{C}_y/\text{Si}$ Heterojunctions", in *Silicon-Germanium Carbon Alloys: Growth, Properties, and Applications*, S.T. Pantelides and S. Zollner, Editors, 2002, p. 59-89.
- [30] M.S. Carroll, Ph.D. Thesis, Princeton University (2001).
- [31] J.C. Sturm and C.M. Reeves, *IEEE Transactions on Electron Devices*, vol. 39(1), p. 81 (1992).

Chapter 3: Suppression of Boron Penetration in P-Channel MOSFETs Using Polycrystalline $\text{Si}_{1-x-y}\text{Ge}_x\text{C}_y$ Gate Layers

3.1 Introduction

For modern p-channel MOSFETs, heavily boron-doped polysilicon is typically used as the gate material. Doping the gate is achieved by ion-implantation with either B^+ or BF_2^+ , followed by an activation anneal. During this anneal the boron atoms also diffuse and distribute themselves throughout the gate. In the past, the gate oxide has been able to block boron atoms from diffusing out of the gate. However, for modern devices with very thin gate oxides, boron can actually diffuse through the gate oxide and down into the channel region during the activation anneal [1]. This boron penetration problem is shown schematically in Figure 3.1. The threshold voltage of the device will be affected by the change in channel doping that results; in this case, the presence of boron atoms in the n-type channel will make the p-MOSFET easier to turn on, and the threshold voltage will shift positive. Boron penetration is very undesirable as it is difficult to control, and gets worse as the gate oxide thickness is reduced or the time or temperature of the post-implant anneal is increased [1].

As mentioned in Chapter 2, $\text{Si}_{1-x-y}\text{Ge}_x\text{C}_y$ alloys have been successfully used in the past to control dopant diffusion in scaled silicon-based devices. In this chapter, we investigate the application of polycrystalline $\text{Si}_{1-x-y}\text{Ge}_x\text{C}_y$ for reducing boron penetration in p-channel MOSFETs. Previously, it has been shown that PMOS capacitors with thin

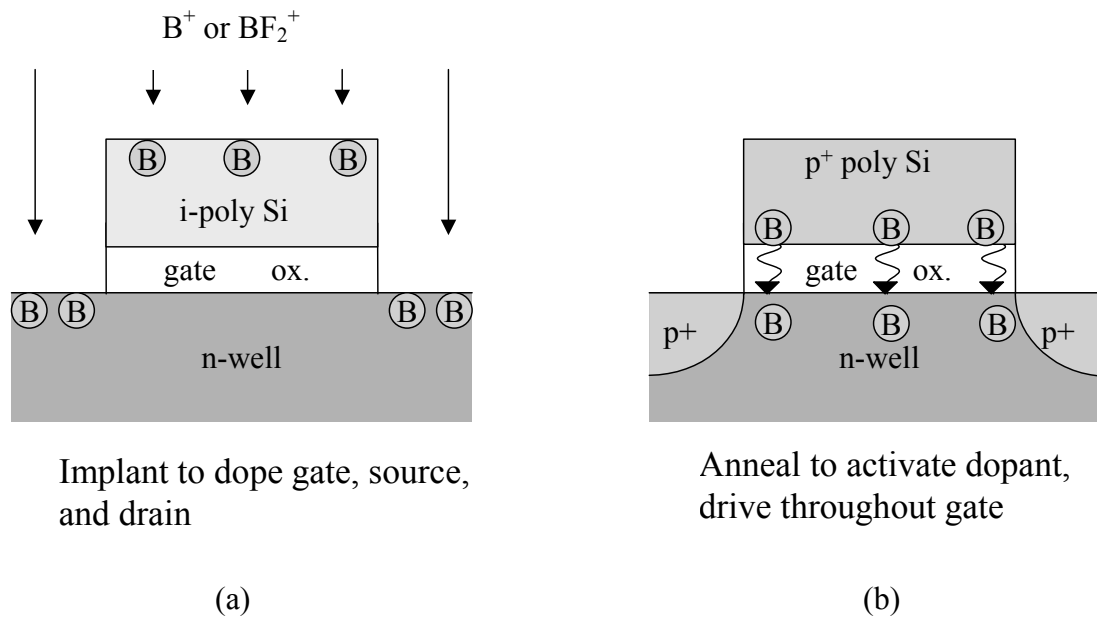


Figure 3.1: Illustration of boron penetration problem in scaled p-channel MOSFETs, showing (a) self-aligned implant, and (b) undesirable boron penetration through the gate oxide and into the substrate during the activation anneal.

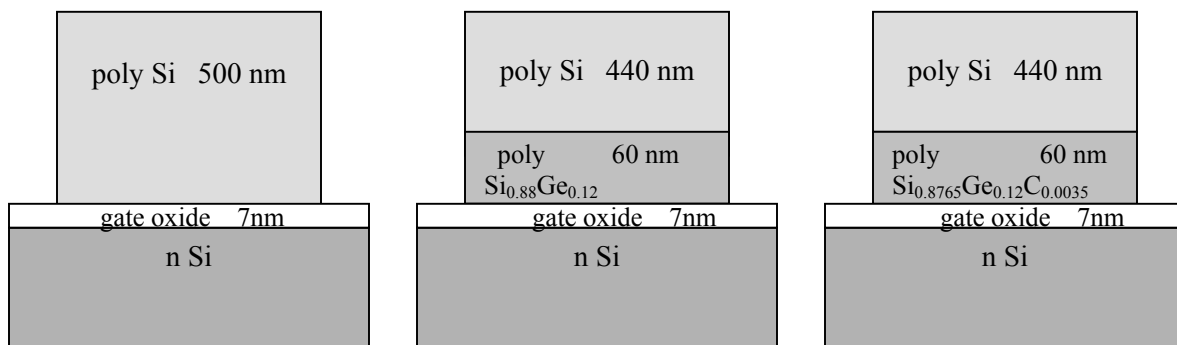
polycrystalline $\text{Si}_{1-x-y}\text{Ge}_x\text{C}_y$ layers in the gates show significantly reduced boron penetration [2]. In this work we find that, consistent with the capacitors, MOSFETs with polycrystalline $\text{Si}_{1-x-y}\text{Ge}_x\text{C}_y$ gate layers have substantially reduced boron penetration and increased threshold voltage stability compared to devices with all polysilicon gates or with polycrystalline $\text{Si}_{1-x}\text{Ge}_x$ gate layers. The performance of the polycrystalline $\text{Si}/\text{Si}_{1-x-y}\text{Ge}_x\text{C}_y$ -gated devices is then characterized and compared with that of the polysilicon or polycrystalline $\text{Si}_{1-x}\text{Ge}_x$ -gated devices. Devices with *in-situ* doped polycrystalline $\text{Si}_{1-x-y}\text{Ge}_x\text{C}_y$ gates, as well as $\text{Si}_{1-x-y}\text{Ge}_x\text{C}_y$ layers positioned away from the gate-oxide interface, are also studied. Finally, the mechanism by which the boron penetration is suppressed is examined in detail.

3.2 MOSFETs with undoped polycrystalline $\text{Si}_{1-x-y}\text{Ge}_x\text{C}_y$ gate layers

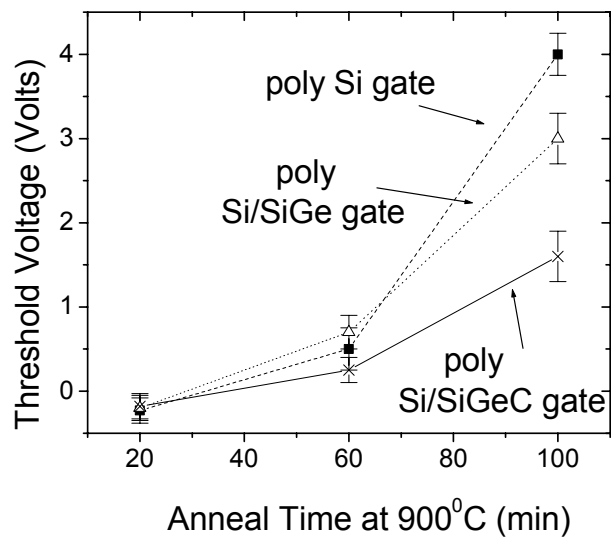
MOSFETs with thin undoped polycrystalline $\text{Si}_{1-x-y}\text{Ge}_x\text{C}_y$ layers in the gates were fabricated. On n-type substrates ($\sim 1 \times 10^{15} \text{ cm}^{-3}$), 500 nm field oxides were first grown and patterned. Gate oxides (7 nm) were then formed by dry oxidation for 10 minutes at 900°C. The wafers were then loaded directly into the RTCVD reactor for polycrystalline gate deposition. An 18% lamp power low-temperature (temperature not precisely calibrated for this lamp power, but should be $\sim 700^\circ\text{C}$) and pressure (6 Torr) H_2 bake was performed instead of the standard high-temperature clean to avoid any potential reaction of H_2 with the thin gate oxide [3]. Polycrystalline Si, $\text{Si}_{1-x}\text{Ge}_x$, and $\text{Si}_{1-x-y}\text{Ge}_x\text{C}_y$ gate layers were then deposited at temperatures between 625-750°C using SiCl_2H_2 and SiH_4 as silicon sources and GeH_4 and SiCH_6 as germanium and carbon sources, respectively.

Polysilicon was grown using recipes Si:1 and Si:2, and polycrystalline $\text{Si}_{1-x}\text{Ge}_x$ and $\text{Si}_{1-x-y}\text{Ge}_x\text{C}_y$ using recipes Si_{1-x}Ge_x:2 and Si_{1-x-y}Ge_xC_y:2, respectively, from Appendix A. Three different gate structures were used, shown in Figure 3.2(a). The bottom 60 nm of each gate was either polycrystalline Si, $\text{Si}_{0.88}\text{Ge}_{0.12}$, or $\text{Si}_{0.8765}\text{Ge}_{0.12}\text{C}_{0.0035}$; the remaining 440 nm was polysilicon, for a total gate thickness of ~500 nm. For gates with polycrystalline $\text{Si}_{1-x}\text{Ge}_x$ or $\text{Si}_{1-x-y}\text{Ge}_x\text{C}_y$ at the oxide interface, a ~1 nm seed layer of polysilicon was first deposited to enhance nucleation on the oxide [4]. The gates were then patterned with gate lengths ranging from 2 μm to 50 μm and, along with the source and drain, subjected to a self-aligned BF_2^+ implant of $2 \times 10^{15} \text{ cm}^{-2}$ at 60 keV. The implant range for these conditions is ~50 nm, so nearly all of the boron is stopped in the top polysilicon layer in all samples. Post-implant anneals were then performed at 900°C in N_2 for either 20, 60, or 100 minutes, to characterize boron penetration effects. A standard backend process completed the device fabrication, consisting of 300-nm PECVD oxide deposition (at 250°C), contact hole and aluminum contact formation, and a 30 min forming gas anneal at 415°C.

Devices with polycrystalline $\text{Si}_{1-x-y}\text{Ge}_x\text{C}_y$ layers in the gates have substantially reduced boron penetration and enhanced threshold voltage stability compared to devices with either polysilicon gates or polycrystalline $\text{Si}_{1-x}\text{Ge}_x$ gate layers. Figure 3.2(b) shows the threshold voltages of the three different gate structures as a function of post-implant anneal time. After a 20 minute anneal, all devices have a threshold voltage of ~-0.2 V. All devices experience positive threshold voltage shifts as anneal time increases, indicating boron penetration into the substrate. However, while the polysilicon and polycrystalline Si/Si_{1-x}Ge_x devices shift by 4.1 and 3.2 volts, respectively, for the



(a)



(b)

Figure 3.2: (a) Structures and (b) threshold voltage vs. post-implant anneal time at 900°C for the three different structures, showing the greatest stability in the polycrystalline $\text{Si}/\text{Si}_{1-x-y}\text{Ge}_x\text{C}_y$ gate.

100-minute anneal time, the polycrystalline Si/Si_{1-x-y}Ge_xC_y devices only shift by 1.8 V. Previously, it has been shown that polycrystalline Si_{1-x}Ge_x gates have reduced boron penetration compared to polysilicon gates [5]. It is clear from Figure 3.2(b), however, that polycrystalline Si_{1-x-y}Ge_xC_y provides even greater stability than polycrystalline Si_{1-x}Ge_x.

Device characteristics for the polycrystalline Si/Si_{1-x-y}Ge_xC_y gates are well behaved. Figure 3.3 shows an I_D-V_D plot for a Si/Si_{1-x-y}Ge_xC_y-gate device after 60 minutes of annealing. Figure 3.4 shows subthreshold characteristics for the three different gate structures after the 100-minute anneal time. In addition to the threshold voltage shifts, this figure shows that the polysilicon and Si/Si_{1-x}Ge_x gate structures cannot be completely turned off (for Figure 3.2(b), threshold voltage was defined by the shift in current characteristic at 50 μA for the polysilicon-gate 100 minute devices). This indicates that so much boron has diffused through the oxide and into the substrate that the resulting p-type layer formed there cannot be fully depleted out. The polycrystalline Si/Si_{1-x-y}Ge_xC_y gate device, however, can be fully turned off and has similar on/off ratios as for shorter anneals.

Effective channel mobility vs. anneal time for the three different structures is plotted in Figure 3.5. Mobilities were extracted from the peak value of a dI_D/dV_g plot with V_{DS}=-0.1, assuming a constant gate capacitance equal to the oxide capacitance, using the equation:

$$\mu_{Eff} = \frac{\frac{dI_D}{dV_G}}{C_{ox} \frac{W}{L} V_{DS}} \quad (3.1)$$

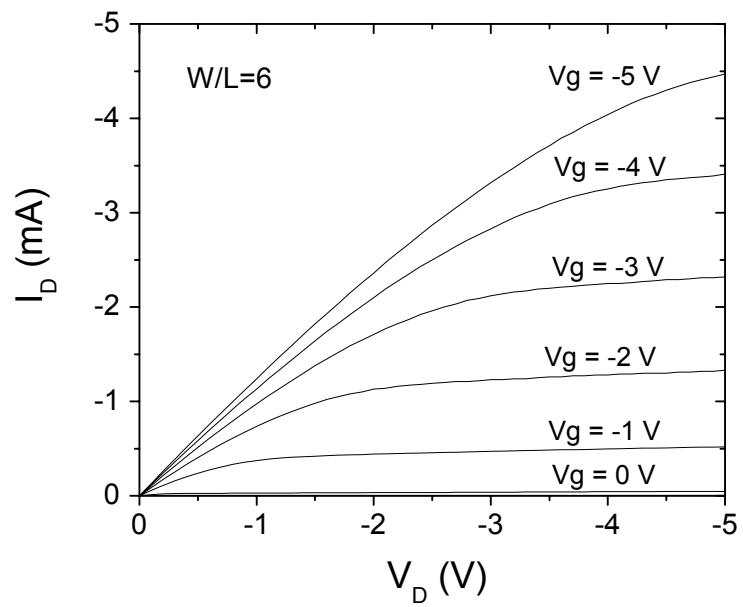


Figure 3.3: I_D - V_D plot for a polycrystalline Si/Si_{1-x-y}Ge_xC_y-gated device annealed for 60 minutes.

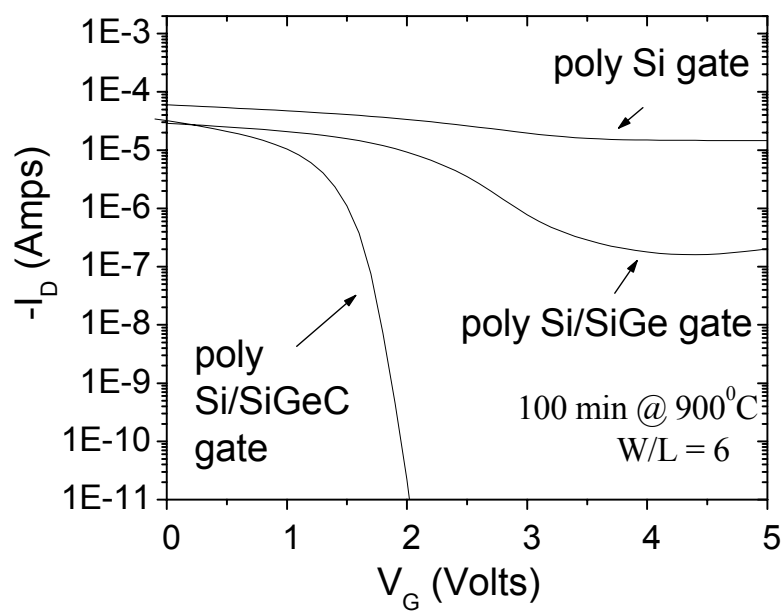


Figure 3.4: Subthreshold characteristics for the three different gate structures after the 100-minute anneal time.

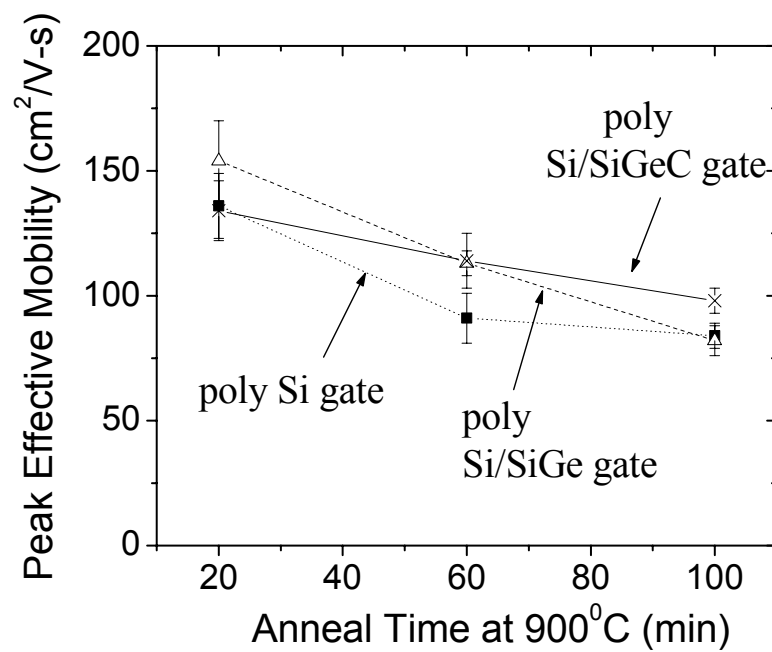
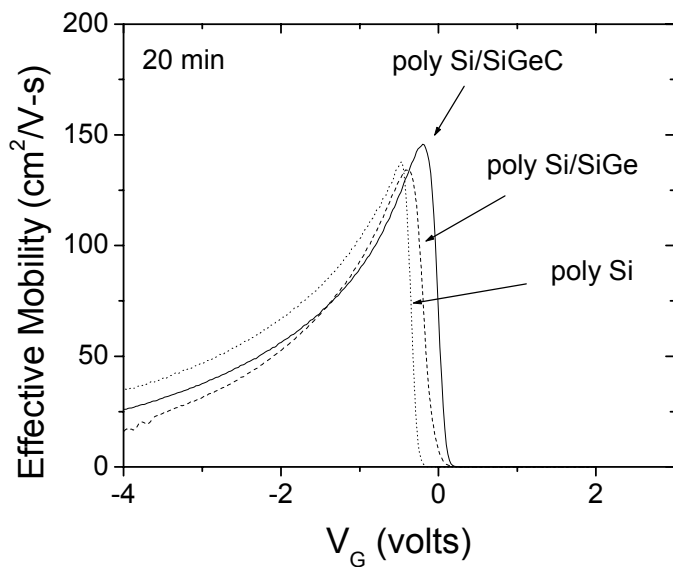


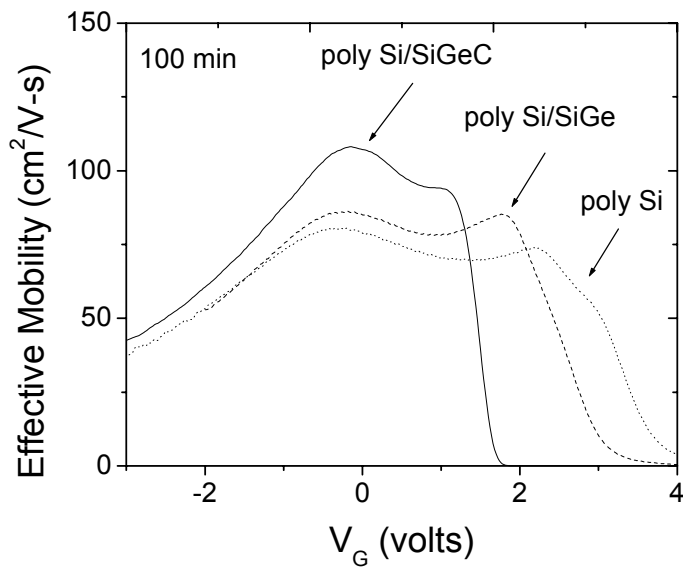
Figure 3.5: Peak effective mobility vs. anneal time, showing comparable performance in the polycrystalline Si/Si_{1-x-y}Ge_xC_y gate devices.

Points represent an average of over 10 devices, with error bars showing the standard deviation. The polycrystalline Si/Si_{1-x-y}Ge_xC_y devices have comparable mobilities vs. the other devices for all anneal times. This indicates that the boron in the Si_{1-x-y}Ge_xC_y gate layers is electrically active. If it were not, then as the devices turn on, gate depletion would occur and create an additional capacitance in series with the oxide, reducing the overall gate-channel capacitance of the device. Since a capacitance of C_{ox} is assumed in Equation (1), this would show up as a drop in effective mobility. However, as seen in Figure 3.5, this does not occur (within error bars). All devices do experience some loss in peak mobility as anneal time is increased. This has been previously observed when large amounts of boron penetration occurs, and some authors have suggested it is due to increased carrier scattering in the channel [1, 6]. However, consistent with reduced boron penetration, the mobility does not decrease as fast in the polycrystalline Si/Si_{1-x-y}Ge_xC_y-gated structures.

Effective mobility vs. gate voltage is plotted in Figure 3.6 for the 20 and 100 minute anneal times. The curves are well-behaved for the 20 minute anneal. However, after 100 minutes of annealing, a broad double-peak begins to appear in all of the devices. This is consistent with the model of boron penetration creating a large p-type layer in the substrate [7]. Initially, as the device turns on (voltage decreased below V_T), holes away from the silicon/SiO₂ interface are carrying the current. These have a smaller effective capacitance (compared to C_{ox}) due to their distance from the interface, and therefore will have a smaller effective mobility when calculated using Equation 3.1. This represents the first peak. Eventually, as gate voltage is decreased further, a surface channel forms, for which the capacitance is now C_{ox} , resulting in the second peak.



(a)



(b)

Figure 3.6: Effective mobility vs. gate voltage after (a) 20 minute and (b) 100 minute anneals. Note the double-peaks which appear in the 100-minute plots, indicating the formation of buried channel devices. This effect is more pronounced in the polycrystalline Si and $\text{Si}_{1-x}\text{Ge}_x$ gated devices, which experience more boron penetration.

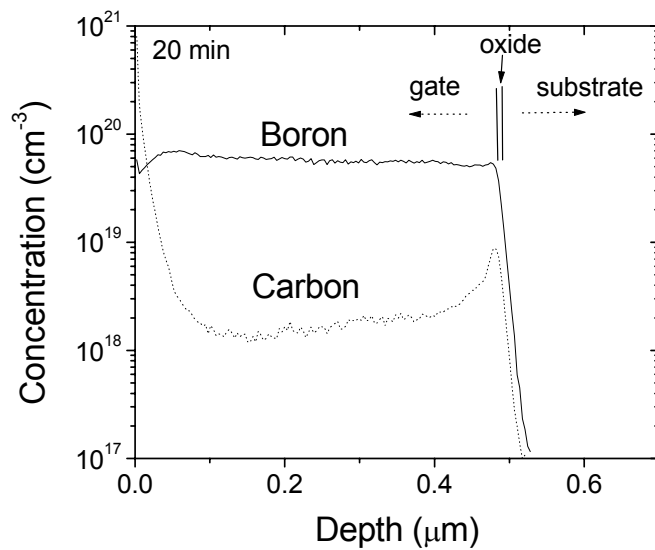
Differences in the actual drift mobility between the two regimes, caused by either surface or ionized impurity scattering, may be causing additional differences between the two peaks. The fact that the double-peaks are more pronounced in the polycrystalline Si and Si/Si_{1-x}Ge_x devices, which experience more boron penetration and therefore have larger buried channels, supports this model.

3.3 Mechanism of reduced boron penetration

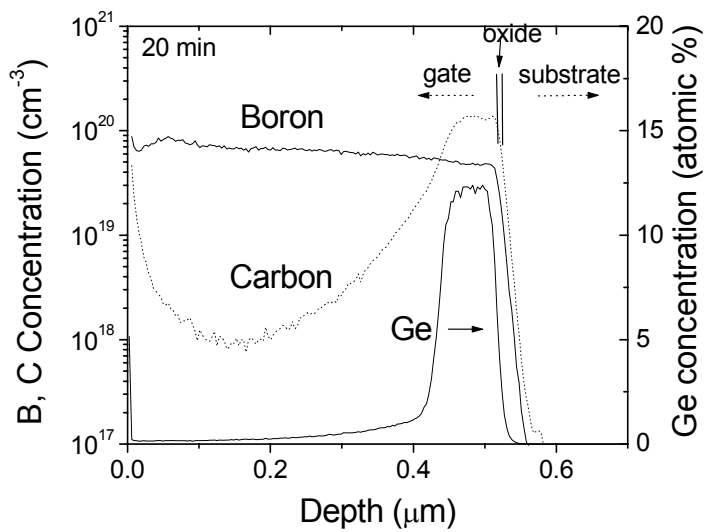
3.3.1 Boron diffusion and segregation in polycrystalline Si_{1-x-y}Ge_xC_y

As discussed in Chapters 1 and 2, boron diffusion in single crystal Si_{1-x-y}Ge_xC_y is known to be much slower than in either single crystal Si or Si_{1-x}Ge_x [8]. Slower boron diffusion has also been reported in polycrystalline Si_{1-x}Ge_x compared to Si [9]. This raises the possibility that in the polycrystalline Si/Si_{1-x-y}Ge_xC_y gate samples, boron is simply taking longer to diffuse through the polycrystalline Si_{1-x-y}Ge_xC_y layer before penetrating into the oxide. This would be undesirable for the performance of the devices, as there would be less dopant at the gate-oxide interface and therefore more gate depletion.

This possibility was first examined using SIMS measurements. Figure 3.7 shows SIMS profiles of boron concentration vs. depth in the gates of the polysilicon and polycrystalline Si/Si_{1-x-y}Ge_xC_y devices after 20 minutes of annealing. In the polysilicon-gate case, the boron concentration has almost flattened out at a level of $\sim 6 \times 10^{19} \text{cm}^{-3}$, with the concentration at the polysilicon/oxide interface = $5.4 \times 10^{19} \text{cm}^{-3}$. In the polycrystalline Si/Si_{1-x-y}Ge_xC_y gate, the profile has mostly flattened out as well; in particular, the boron

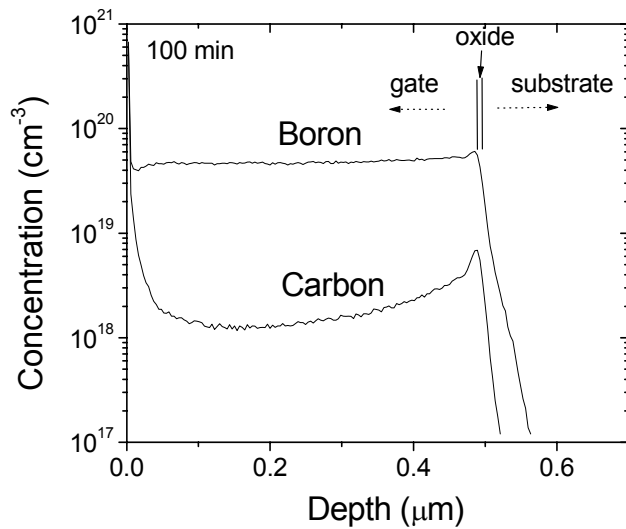


(a)

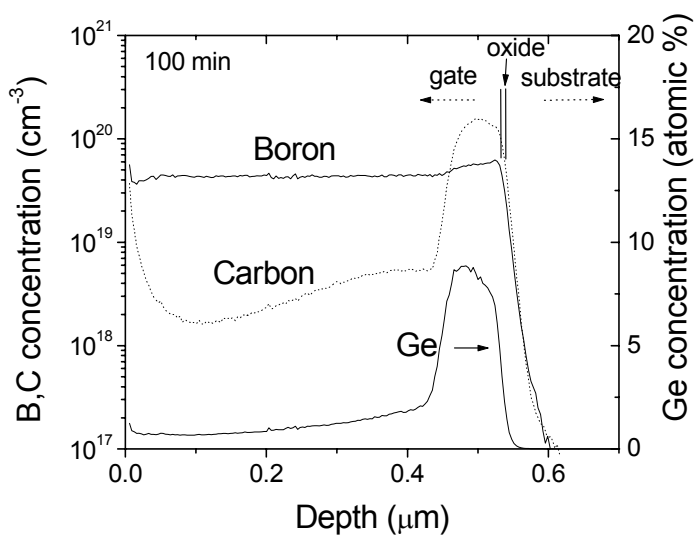


(b)

Figure 3.7: SIMS profiles of boron concentration vs. depth for (a) the all-polysilicon gate, and (b) the polycrystalline $\text{Si}/\text{Si}_{1-x-y}\text{Ge}_x\text{C}_y$ gate, after 20 minutes of annealing at 900°C .



(a)



(b)

Figure 3.8: SIMS profiles of boron concentration vs. depth for (a) the all-polysilicon gate, and (b) the polycrystalline $\text{Si}/\text{Si}_{1-x-y}\text{Ge}_x\text{C}_y$ gate, after 100 minutes of annealing at 900°C .

has been able to diffuse through the entire polycrystalline $\text{Si}_{1-x-y}\text{Ge}_x\text{C}_y$ layer, reaching a concentration of $5.0 \times 10^{19} \text{cm}^{-3}$ at the oxide interface. Clearly, while boron has a very low diffusion coefficient in single-crystal $\text{Si}_{1-x-y}\text{Ge}_x\text{C}_y$ layers, it does not appear to be prevented from diffusing through the polycrystalline $\text{Si}_{1-x-y}\text{Ge}_x\text{C}_y$ layers. This is presumably due to grain boundary mechanisms - i.e. the diffusion of boron along grain boundaries in polycrystalline $\text{Si}_{1-x-y}\text{Ge}_x\text{C}_y$ is much faster than in bulk $\text{Si}_{1-x-y}\text{Ge}_x\text{C}_y$.

Figure 3.8 shows SIMS profiles of the two structures after 100 minutes of annealing. The profile in the polysilicon gate device is once again flat ($\text{Si}/\text{Si}_{1-x}\text{Ge}_x$ samples show similar behavior). However, in the polycrystalline $\text{Si}/\text{Si}_{1-x-y}\text{Ge}_x\text{C}_y$ -gate case, boron is starting to accumulate in the polycrystalline $\text{Si}_{1-x-y}\text{Ge}_x\text{C}_y$ layer, with the ratio of boron concentration in the polycrystalline $\text{Si}_{1-x-y}\text{Ge}_x\text{C}_y$ vs. polysilicon equal to ~ 1.3 . This accumulation in the $\text{Si}_{1-x-y}\text{Ge}_x\text{C}_y$ layers should have the effect of keeping more total boron in the gate for a given anneal time, since more boron remains trapped in the $\text{Si}_{1-x-y}\text{Ge}_x\text{C}_y$ layer and less penetrates into the oxide and substrate. This segregation effect plays a crucial role in the reduction of boron penetration; however, a detailed analysis of this effect, and its implications for MOSFETs, is deferred until the next chapter.

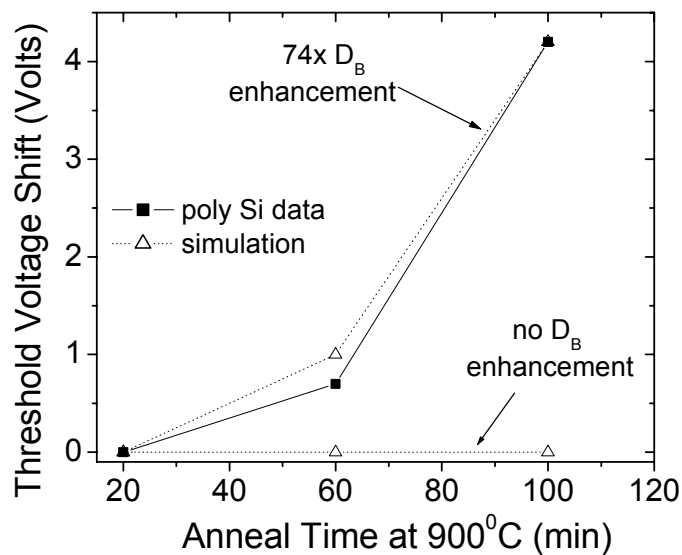
3.3.2 Simulations of the effect of lower boron diffusivity in polycrystalline $\text{Si}_{1-x-y}\text{Ge}_x\text{C}_y$

To further examine the possibility that a reduced diffusivity in the polycrystalline $\text{Si}_{1-x-y}\text{Ge}_x\text{C}_y$ layer may be playing a role, we modeled our devices using the TSUPREM and MEDICI simulators. Structures identical to our MOSFETs were simulated,

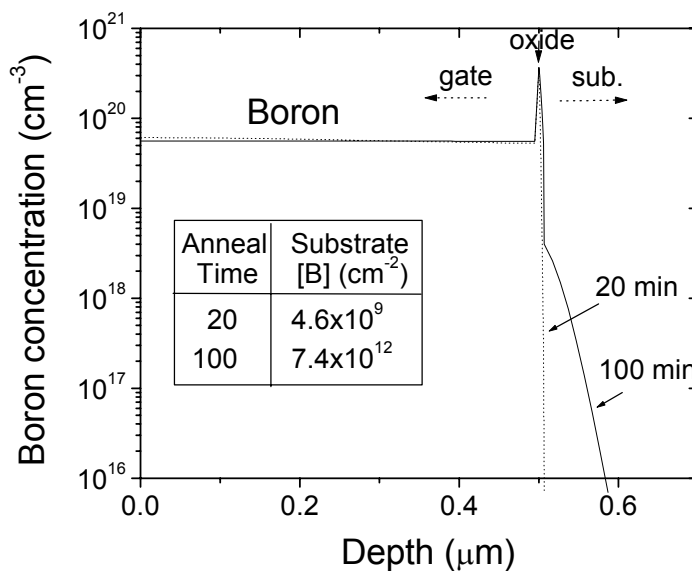
consisting of an n-type substrate ($1 \times 10^{15} \text{ cm}^{-3}$), 7 nm gate oxide, and 500 nm total gate thickness. These were then subjected to the same process conditions as in experiment - a 60 keV BF_2^+ implant at $2 \times 10^{15} \text{ cm}^{-2}$, followed by a post-implant anneal in N_2 at 900°C for either 20, 60 or 100 minutes. The threshold voltages of the modeled boron profiles were then extracted for the different anneal times.

As a control, the all-polysilicon gate structure was first simulated. The effective diffusivity of boron in the polysilicon was set to $7.5 \times 10^{-13} \text{ cm}^2/\text{sec}$ to match our diffusion profiles during the 20-minute anneal. With the polysilicon diffusion now set, we found that the threshold voltage shifts due to boron penetration were heavily under-predicted (Figure 3.9(a)). This is due to the effect of fluorine on boron penetration: it is known that, when BF_2^+ is used instead of B^+ as the implantation species, boron penetration increases dramatically, resulting in much bigger V_T shifts [1]. A device implanted with B^+ sees very little increase in V_T . The fluorine effect has been modeled in the literature as increasing the diffusivity of boron in the gate oxide, with enhancement factors ranging from 30-300X for BF_2^+ doses in the range of 10^{15} - 10^{16} cm^{-2} [1, 10]. Since our devices were implanted with BF_2^+ instead of B^+ , this effect needs to be included in a process simulator such as TSUPREM. We find that increasing D_B in our simulated gate oxides by a factor of 74 gives a reasonable fit for our threshold voltage shifts (Figure 3.9(a)). Figure 3.9(b) shows the simulated profiles of boron in the gates and substrates for structures with the 74X diffusion enhancement. Boron that has penetrated through the oxide is clearly seen in the exponentially decreasing p-type layer in the substrate after the 100-minute simulated anneal.

The polycrystalline $\text{Si}/\text{Si}_{1-x-y}\text{Ge}_x\text{C}_y$ -gate structure was then modeled by making



(a)



(b)

Figure 3.9: (a) Simulated threshold voltage shifts vs. post-implant anneal time for polysilicon-gated devices, with or without a 74X enhancement of boron diffusion in the gate oxide (to simulate the effect of the implanted fluorine). (b) Simulated boron profiles for devices with the 74X diffusion enhancement, annealed for either 20 or 100 minutes. Inset shows the amount of integrated boron in the substrate for the two different anneal times.

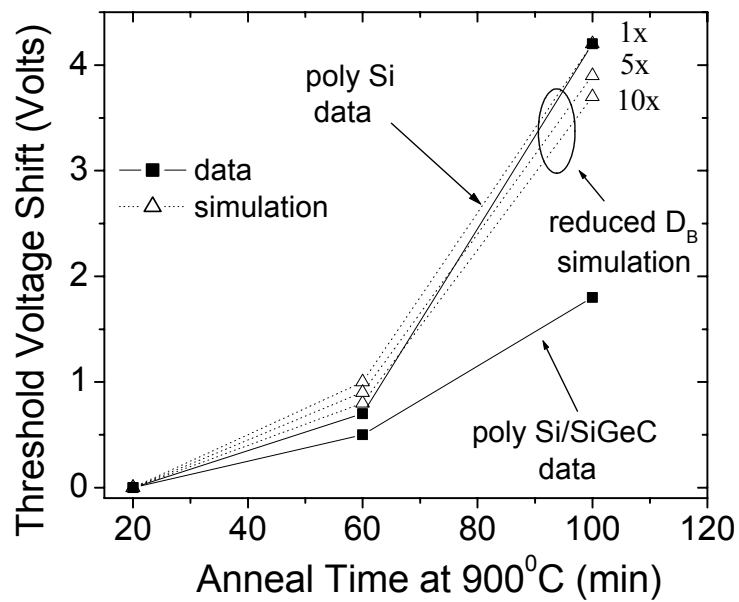


Figure 3.10: Simulated threshold voltage shifts vs. post-implant anneal time for polycrystalline $\text{Si}/\text{Si}_{1-x-y}\text{Ge}_x\text{C}_y$ devices, with different reductions in the boron diffusivity in the polycrystalline $\text{Si}_{1-x-y}\text{Ge}_x\text{C}_y$ layer.

the bottom 60 nm of the gate identical to polysilicon in every way, except that the boron diffusivity is reduced by factors up to 10X. Figure 3.10 shows threshold voltage vs. anneal time for different values of boron diffusivity in the polycrystalline $\text{Si}_{1-x-y}\text{Ge}_x\text{C}_y$ layer. As can be seen, even for a very large reduction of 10X in the diffusivity, the boron penetration is not suppressed nearly as much as in the data. In addition, a 10X reduction in diffusivity is already more than that observed in experiment - the simulator predicts that for a 10X diffusivity reduction, the boron concentration at the poly/oxide interface only reaches $4.6 \times 10^{19} \text{ cm}^{-3}$ after 20 minutes of annealing, while we experimentally observe (Figure 3.7(b)) a value of $5.0 \times 10^{19} \text{ cm}^{-3}$. As a result, we conclude that a reduction in diffusivity is not the primary factor responsible for the reduced boron penetration.

3.3.3 MOSFETs with *in-situ* doped polycrystalline $\text{Si}_{1-x-y}\text{Ge}_x\text{C}_y$ gates

A second set of MOSFETs with *in-situ* doping throughout the gates provides additional evidence that the polycrystalline $\text{Si}_{1-x-y}\text{Ge}_x\text{C}_y$ layer is not just acting as a diffusion barrier [3]. For these devices, ~8nm gate oxides were first grown on unpatterned n-type substrates. Polycrystalline gate deposition was then performed by RTCVD at 625°C and 700°C , using SiH_4 , GeH_4 , SiCH_6 , and B_2H_6 as silicon, germanium, carbon, and boron sources, respectively. Polysilicon was grown using the Si:2 recipe, and polycrystalline $\text{Si}_{1-x-y}\text{Ge}_x\text{C}_y$ the $\text{Si}_{1-x-y}\text{Ge}_x\text{C}_y$:2 recipe, listed in Appendix A. The same low temperature clean and polysilicon seed layer (for polycrystalline $\text{Si}_{1-x-y}\text{Ge}_x\text{C}_y$ gates) used in section 3.2 were employed here. The gate was a single layer consisting of

either *in-situ* boron-doped ($\sim 1 \times 10^{21} \text{ cm}^{-3}$) polysilicon or polycrystalline $\text{Si}_{0.794}\text{Ge}_{0.2}\text{C}_{0.006}$, for a total gate thickness of $\sim 150 \text{ nm}$ [3]. Following deposition, gates were patterned into ring structures to allow for device isolation. Gate, source, and drain for all samples were then simultaneously implanted with $2 \times 10^{15} \text{ cm}^{-2} \text{ BF}_2^+$ at 50 keV and annealed at 900°C in N_2 for 20, 50, or 80 minutes, followed by metal deposition and patterning. As the gates were already doped *in-situ*, the implant was performed to allow fluorine to induce enhanced boron penetration effects. If uniformly distributed, the implant would raise the boron level in the gates by $1.3 \times 10^{20} \text{ cm}^{-3}$.

Again, devices with $\text{Si}_{1-x-y}\text{Ge}_x\text{C}_y$ gates have reduced boron penetration and increased threshold stability compared to devices with all polysilicon gates. Figure 3.11 shows threshold voltage vs. anneal time for these devices. Both devices experience positive threshold voltage shifts with increasing anneal time, indicating boron penetration into the substrate. However, after 20 and 50 minutes of annealing, the polysilicon gates have threshold voltages of 1.8 V and 5.3 V, respectively, whereas the polycrystalline $\text{Si}_{1-x-y}\text{Ge}_x\text{C}_y$ gate threshold voltages remain at 0.0 V and 0.3 V. Similar to section 3.2, the polysilicon-gate 50 minute annealed device cannot be fully turned off, indicating that again enough boron has entered the substrate to prevent it from being fully depleted out (threshold voltage for the polysilicon-gate devices was defined by the shift in current characteristic at $50 \mu\text{A}$ for Figure 3.11). The devices with polycrystalline $\text{Si}_{1-x-y}\text{Ge}_x\text{C}_y$ gates, however, for up to 80 minutes of annealing, maintain constant on/off currents and only shift to $V_T=0.8 \text{ V}$ (Figure 3.12).

Since these devices began with boron doping already in the gates, the primary mechanism of reduced penetration is clearly not the polycrystalline $\text{Si}_{1-x-y}\text{Ge}_x\text{C}_y$ layer

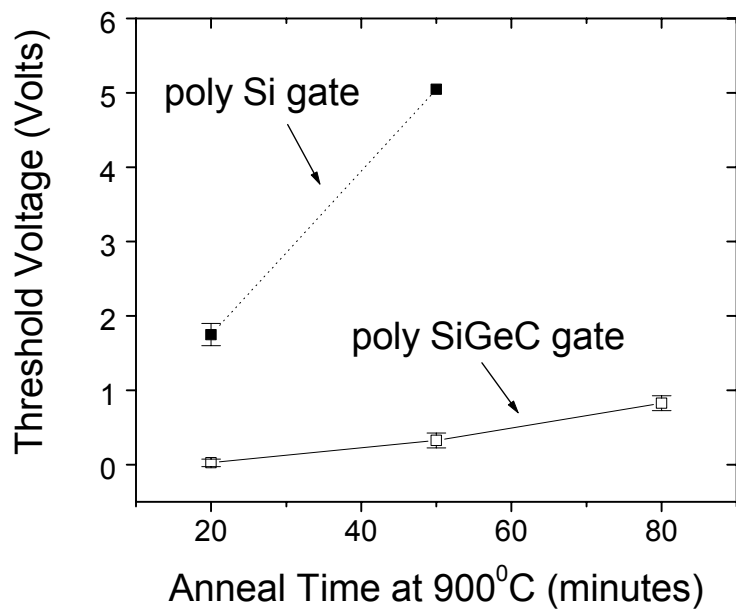


Figure 3.11: Threshold voltage vs. anneal time for MOSFETs with gates doped *in-situ* with boron to a level of $\sim 10^{21} \text{ cm}^{-3}$.

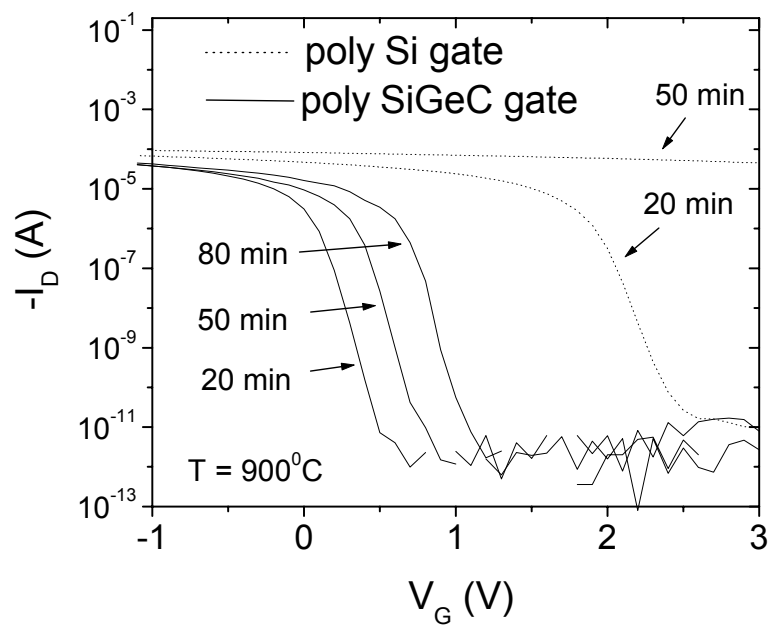


Figure 3.12: Subthreshold characteristics for MOSFETs with initially *in-situ* doped gates.

preventing boron from diffusing down to the gate-oxide interface. This is consistent with the conclusion from the modeling of the devices in the previous section in which the boron in the gate was all introduced by ion implantation. Therefore another mechanism must be responsible for the reduced penetration of boron through the gate oxide.

3.3.4 Proximity of polycrystalline $\text{Si}_{1-x-y}\text{Ge}_x\text{C}_y$ to gate oxide

Another possible mechanism is some sort of interaction of the polycrystalline $\text{Si}_{1-x-y}\text{Ge}_x\text{C}_y$ layer with the gate oxide. For example, perhaps a high level of carbon in SiO_2 (diffusing into the gate oxide from the adjacent polycrystalline $\text{Si}_{1-x-y}\text{Ge}_x\text{C}_y$ layer) reduces the boron diffusivity, thereby reducing the amount of boron getting through the oxide into the substrate.

To investigate this possibility, a set of capacitors were fabricated to test the effectiveness of a gate structure where the polycrystalline $\text{Si}_{1-x-y}\text{Ge}_x\text{C}_y$ layer is positioned away from the gate/oxide interface. On top of unpatterned n-type substrates and ~ 6 nm gate oxides, three different gate structures were deposited, each with a total gate thickness of 500 nm (Figure 3.13(a)). The first two samples were (A) a standard polysilicon gate and (B) a polycrystalline $\text{Si}/\text{Si}_{0.792}\text{Ge}_{0.20}\text{C}_{0.008}$ structure similar to the one used for the MOSFETs of section 3.2. The polycrystalline $\text{Si}_{0.792}\text{Ge}_{0.20}\text{C}_{0.008}$ layer was 60 nm thick. The third sample (C) is similar to B except the $\text{Si}_{0.792}\text{Ge}_{0.20}\text{C}_{0.008}$ layer is positioned 160 nm away from the SiO_2 interface. Polysilicon and polycrystalline $\text{Si}_{1-x-y}\text{Ge}_x\text{C}_y$ were again grown using the Si:2 and $\text{Si}_{1-x-y}\text{Ge}_x\text{C}_y$:2 recipes, respectively, from Appendix A. These samples were all implanted with $2 \times 10^{15} \text{ cm}^{-2} \text{ BF}_2^+$ at 60 keV

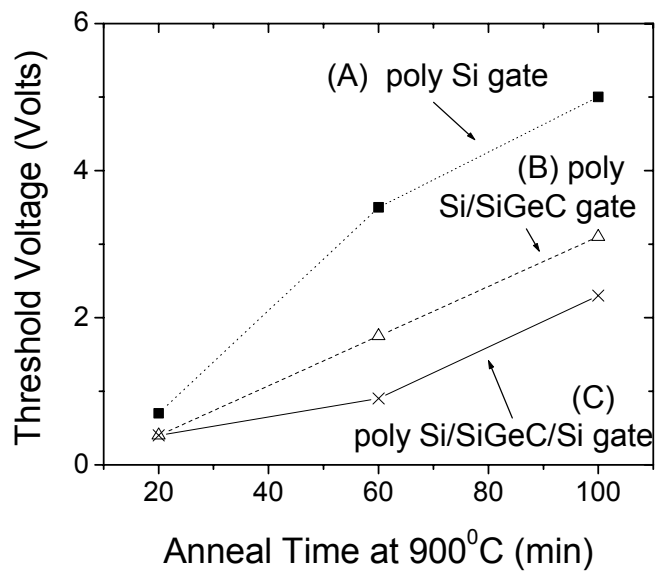
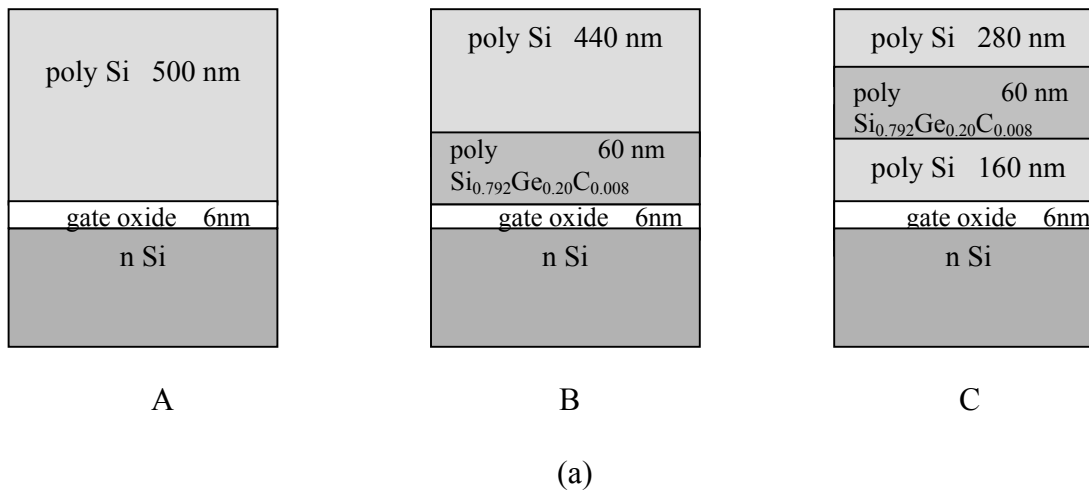


Figure 3.13: (a) Structures and (b) threshold voltage vs. anneal time for capacitor structures A, B, and C.

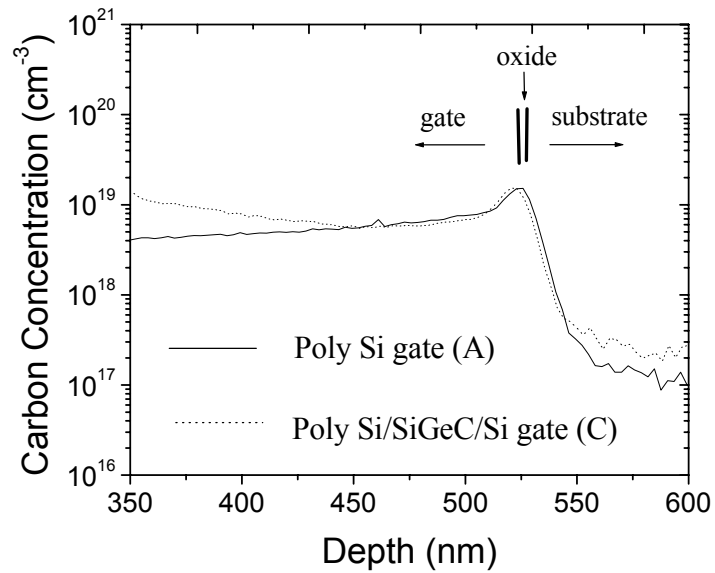


Figure 3.14: SIMS profiles of carbon in the gate oxides of structures A and C after the 60-minute anneal time. For sample C, the polycrystalline $\text{Si}_{1-x-y}\text{Ge}_x\text{C}_y$ layer can't be seen in the figure (off to the left at a depth of ~330 nm).

and annealed at 900°C for different times, and patterned into capacitors. Threshold voltages were extracted using C-V measurements. Figure 3.13(b) shows threshold voltage characteristics of these three samples for different post-implant anneal times. As anticipated, structure B shows increased threshold voltage stability vs. structure A. If this were due to some sort of polycrystalline $\text{Si}_{1-x-y}\text{Ge}_x\text{C}_y$ -gate oxide interaction, structure C would be expected not to show the same effect. However, as can be seen, sample C also strongly reduces boron penetration - in fact, C is better than sample B. This shows that the polycrystalline $\text{Si}_{1-x-y}\text{Ge}_x\text{C}_y$ layer does not have to be adjacent to the gate oxide to be effective in suppressing boron penetration. In particular, the polycrystalline $\text{Si}_{1-x-y}\text{Ge}_x\text{C}_y$ is far enough away from the gate oxide that the carbon levels in the oxide in sample C and sample A (all polysilicon gate) are nearly identical at $\sim 1.5 \times 10^{19} \text{ cm}^{-3}$ (Figure 3.14).

3.3.5 Fluorine trapping

As mentioned earlier, fluorine plays an important role in enhancing the boron penetration in our devices. Fluorine from the BF_2^+ implant diffuses down into the oxide and enhances the diffusivity of boron there. This effect had to be included in our simulation of the control (polysilicon gate) MOSFET to reproduce the observed threshold voltage shifts (Figure 3.9(a)). If no fluorine effects are present, the devices should be much more stable. This raises the possibility that if the polycrystalline $\text{Si}_{1-x-y}\text{Ge}_x\text{C}_y$ layer were acting as a fluorine trap, allowing less fluorine into the gate oxide, this might explain the reduction in the boron penetration. However, SIMS profiles of fluorine in the different structures do not support this hypothesis. Figure 3.15 compares structure A (all

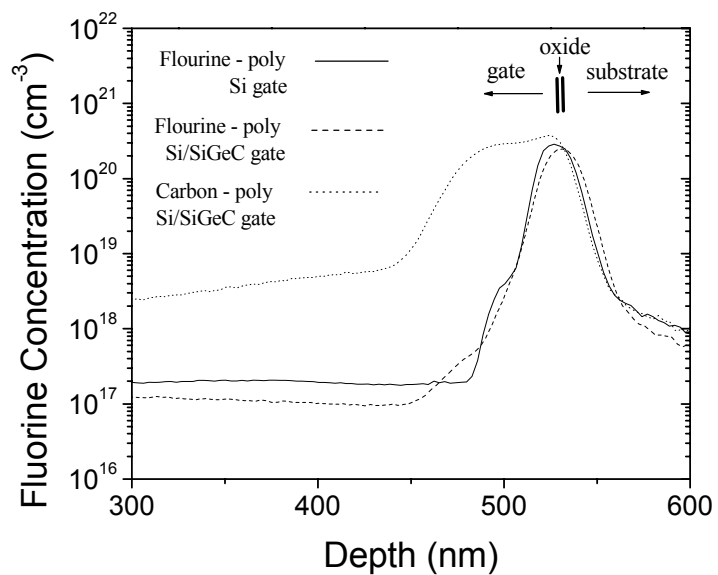


Figure 3.15: Fluorine profiles in the gates of sample “A” (all polysilicon gate) vs. sample “B” (polycrystalline $\text{Si}/\text{Si}_{1-x-y}\text{Ge}_x\text{C}_y$ gate) after 60 minutes of annealing. The carbon profile indicates where the polycrystalline $\text{Si}_{1-x-y}\text{Ge}_x\text{C}_y$ layer is for that sample.

polysilicon) vs. structure B (polycrystalline Si/Si_{1-x-y}Ge_xC_y) from the previous section. If polycrystalline Si_{1-x-y}Ge_xC_y were acting as a fluorine barrier or trap, fluorine would either be seen to (i) pile up in the Si_{1-x-y}Ge_xC_y layer or (ii) be unable to diffuse through it, resulting in less getting into the oxide to enhance boron diffusivity. Neither of these effects is observed. No fluorine peak is observed in the polycrystalline Si_{1-x-y}Ge_xC_y layer, and the integrated fluorine in the gate oxide is very similar in the two samples. Therefore, the polycrystalline Si_{1-x-y}Ge_xC_y is not acting as a fluorine trap, and differences in the fluorine behavior cannot be used to explain the differences in boron penetration through the gate oxide.

3.4 Summary

In summary, we find that polycrystalline Si_{1-x-y}Ge_xC_y gate layers are effective at reducing boron penetration and enhancing the threshold voltage stability of p-channel MOSFETs. Devices with polycrystalline Si_{1-x-y}Ge_xC_y gate layers are well-behaved and have comparable performance vs. conventional devices. Effects such as fluorine trapping, possible interaction of the polycrystalline Si_{1-x-y}Ge_xC_y with the gate oxide, or a reduced boron diffusivity in polycrystalline Si_{1-x-y}Ge_xC_y, are not sufficient to explain the reduced penetration. The accumulation of boron in the polycrystalline Si_{1-x-y}Ge_xC_y layers appears to be responsible for the reduction of boron diffusing into the substrate. In the next chapter, we investigate this segregation effect in detail and discuss its implications for the use of polycrystalline Si_{1-x-y}Ge_xC_y in p-channel MOSFETs.

3.5 References

- [1] J.R. Pfiester, F.K. Baker, T.C. Mele, H. Tseng, P.J. Tobin, J.D. Hayden, J.W. Miller, C.D. Gunderson, and L.C. Parrillo, *IEEE Trans. Electron Devices*, vol. 37, p. 1842-1850 (1990).
- [2] C.L. Chang and J.C. Sturm, *Applied Physics Letters*, vol. 74 (17), p. 2501-2503 (1999).
- [3] C.L. Chang, Ph.D. Thesis, Princeton University (1998).
- [4] M. Cao, A. Wang, and K. Saraswat, *Journal of the Electrochemical Society*, vol. 142 (5), p. 1566-1572 (1995).
- [5] W.-C. Lee, B. Watson, T.-J. King, and C. Hu, *IEEE Electron Device Letters*, vol. 20, p. 232-234 (1999).
- [6] B.Y.Kim, I.M. Liu, H.F. Luan, M. Gardner, J. Fulford, and D.L. Kwong, *Microelectronic Engineering*, vol. 36, p. 313-316 (1997).
- [7] J.S.T. Huang and G.W. Taylor, *IEEE Transactions on Electron Devices*, vol. 22, p. 995-1001 (1975).
- [8] M.S. Carroll, L.D. Lanzerotti, and J.C.Sturm, *Mat. Res. Soc. Symp. Proc.*, vol. 527, p. 417-422 (1998).
- [9] C. Salm, D.T. van Veen, D.J. Gravesteijn, J. Holleman, and P.H. Woerlee, *Journal of the Electrochemical Society*, vol. 144 (10), p. 3665-3673 (1997).
- [10] T. Aoyama, K. Suzuki, H. Tashiro, Y. Toda, T. Yamazaki, K. Takasaki, and T. Ito, *Journal of Applied Physics*, vol. 77(1), p. 417-419 (1995).

Chapter 4: Boron segregation and electrical properties in polycrystalline $\text{Si}_{1-x-y}\text{Ge}_x\text{C}_y$ and $\text{Si}_{1-y}\text{C}_y$

4.1 Introduction

As shown in the previous chapter, p-channel MOSFETs with polycrystalline $\text{Si}_{1-x-y}\text{Ge}_x\text{C}_y$ gate layers have increased threshold voltage stability vs. conventional devices and comparable device performance. Preferential boron segregation from polysilicon to polycrystalline $\text{Si}_{1-x-y}\text{Ge}_x\text{C}_y$ appears to play a key role in suppressing boron out-diffusion from the gate. As a result, it is important to better understand this effect and under what conditions it is observed. Therefore, in this chapter we examine boron segregation to polycrystalline $\text{Si}_{1-x-y}\text{Ge}_x\text{C}_y$ from polysilicon in detail, including its dependence on annealing conditions, carbon content, and the presence of germanium. In addition, it is important to determine what other effects the segregation process may be having. For example, if the segregation is related to the formation of boron-carbon defects, it may degrade the electrical properties of the material. For the application of polycrystalline $\text{Si}_{1-x-y}\text{Ge}_x\text{C}_y$ to MOSFET gates, a high conductivity is desirable to avoid gate depletion problems. Therefore, we examine the electrical properties of polycrystalline $\text{Si}_{1-x-y}\text{Ge}_x\text{C}_y$ and what effect thermal anneals (under conditions similar to those needed for segregation) have on them. Finally, we use the data of the observed segregation to quantitatively model the improved threshold voltage stability observed in the previous chapter.

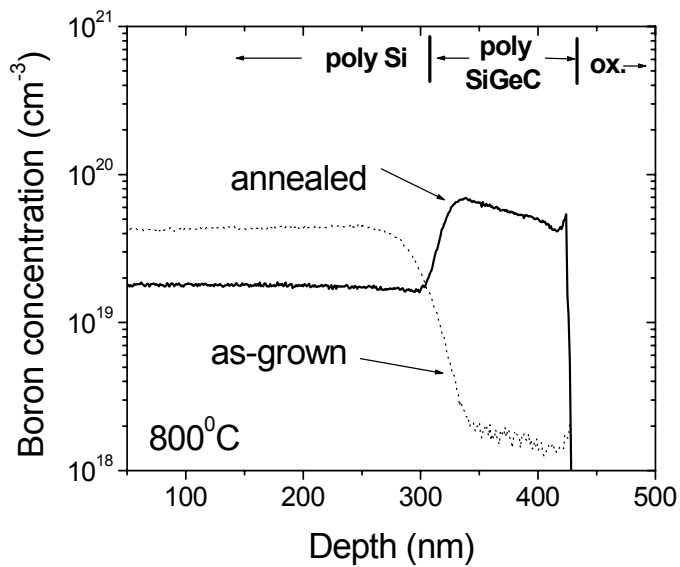
4.2 Boron segregation in polycrystalline $\text{Si}_{1-x-y}\text{Ge}_x\text{C}_y$

All samples used in this chapter were grown by Rapid Thermal Chemical Vapor Deposition (RTCVD), using germane, methylsilane, and diborane as sources for germanium, carbon, and boron, respectively. For samples containing polycrystalline $\text{Si}_{1-x-y}\text{Ge}_x\text{C}_y$ layers, polysilicon was grown at 700°C and polycrystalline $\text{Si}_{1-x-y}\text{Ge}_x\text{C}_y$ at 625°C, both using silane as a silicon source (recipes Si:2 and $\text{Si}_{1-x-y}\text{Ge}_x\text{C}_y$:2, respectively, from Appendix A). For structures containing polycrystalline $\text{Si}_{1-y}\text{C}_y$ layers, polysilicon and polycrystalline $\text{Si}_{1-y}\text{C}_y$ were both grown at 625°C with disilane using recipes Si:3 and $\text{Si}_{1-y}\text{C}_y$:1, respectively, from Appendix A. Previous work shows that for single-crystal $\text{Si}_{1-x-y}\text{Ge}_x\text{C}_y$ and $\text{Si}_{1-y}\text{C}_y$ films grown under similar conditions as those used for this study, most of the carbon is substitutional [1,2]. All layers were grown on thermally oxidized silicon substrates. Grain sizes, from plan-view TEM, were observed to be about ~40 nm.

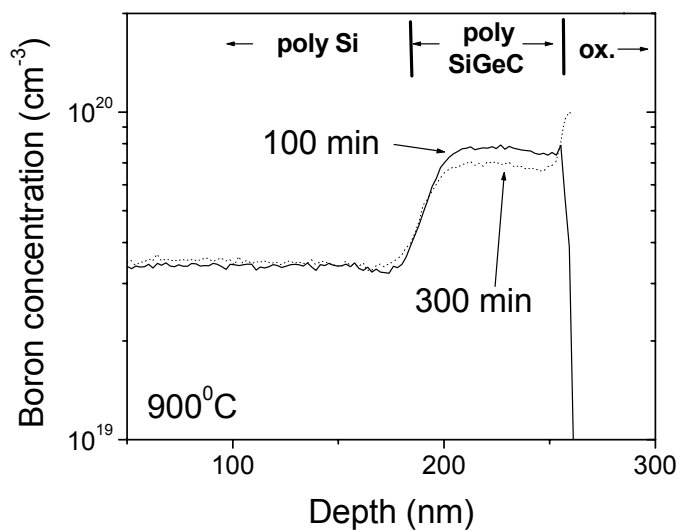
Two types of structures were grown to study segregation in polycrystalline $\text{Si}_{1-x-y}\text{Ge}_x\text{C}_y$. The first was a two-layer structure consisting of a 100 nm lightly *in-situ* boron-doped polycrystalline $\text{Si}_{0.765}\text{Ge}_{0.22}\text{C}_{0.015}$ layer followed by a 300 nm heavily *in-situ* boron-doped polysilicon layer. The second was a multi-layer structure consisting of several 50 nm polycrystalline $\text{Si}_{0.8-y}\text{Ge}_{0.2}\text{C}_y$ layers (carbon percentages varied from 0 to 1%) sandwiched between 70 nm polysilicon layers. All layers were *in-situ* doped with boron at about 10^{20} cm^{-3} . Both of these samples were annealed at temperatures between 800°C and 900°C in nitrogen to allow boron to move from the polysilicon layers into the polycrystalline $\text{Si}_{1-x-y}\text{Ge}_x\text{C}_y$ layers. Secondary Ion Mass Spectroscopy (SIMS) analysis was used to measure the boron profiles in all samples.

Boron segregation to polycrystalline $\text{Si}_{1-x-y}\text{Ge}_x\text{C}_y$ was consistently observed. As an example, Figure 4.1(a) shows SIMS profiles of the two-layer polycrystalline $\text{Si}/\text{Si}_{0.765}\text{Ge}_{0.22}\text{C}_{0.015}$ structure before and after an 800°C , 44 hour anneal. Before the anneal, the polysilicon layer is heavily doped at a level of $4 \times 10^{19} \text{ cm}^{-3}$, while the polycrystalline $\text{Si}_{0.765}\text{Ge}_{0.22}\text{C}_{0.015}$ layer is lightly doped at a level of $2 \times 10^{18} \text{ cm}^{-3}$. If there were no segregation between the layers, this profile would be expected to flatten out during the anneal. However, after annealing, boron levels have risen in the polycrystalline $\text{Si}_{0.765}\text{Ge}_{0.22}\text{C}_{0.015}$ layer to $4.6 \times 10^{19} \text{ cm}^{-3}$, while the boron concentration has decreased in the polysilicon to $1.5 \times 10^{19} \text{ cm}^{-3}$, demonstrating strong segregation to the polycrystalline $\text{Si}_{0.765}\text{Ge}_{0.22}\text{C}_{0.015}$. Defining a segregation coefficient m as the ratio of boron concentration in the polycrystalline $\text{Si}_{1-x-y}\text{Ge}_x\text{C}_y$ to the polysilicon at the interface, we find $m=4.0$ for these parameters ($\text{Ge} = 22\%$, $\text{C}=1.5\%$) and annealing conditions.

Figure 4.1(b) shows an example of boron segregation and its time dependence at 900°C . A similar structure (identical to previous sample except slightly thinner) was annealed for 100 and 300 minutes. After 100 minutes, segregation can again be seen, but is somewhat less than at 800°C ($m= 2.4$). After 300 minutes of annealing, no increase in the segregation is observed (there may be a slight decrease, but it is not known if this decrease is statistically significant). This data indicates that anneal times on the order of 900°C for 100 minutes are long enough for the segregation process to reach a quasi-equilibrium (not a true equilibrium, as the out-diffusion of carbon and germanium from the polycrystalline $\text{Si}_{1-x-y}\text{Ge}_x\text{C}_y$ layer will take place with further annealing and affect the segregation coefficient).



(a)



(b)

Figure 4.1: SIMS profiles of boron concentration vs. depth for the two-layer polycrystalline $\text{Si}/\text{Si}_{0.765}\text{Ge}_{0.22}\text{C}_{0.015}$ samples after (a) an 800°C , 44-hour anneal, and (b) 900°C anneals for 100 and 300 minutes.

The multi-layer polycrystalline $\text{Si}_{1-x-y}\text{Ge}_x\text{C}_y$ structure shows that the segregation is strongly dependent on carbon level. SIMS of this structure before and after an 800°C, 18-hour anneal are shown in Figure 4.2. Before the anneal, the polycrystalline $\text{Si}_{0.8-y}\text{Ge}_{0.2}\text{C}_y$ layers are *in-situ* doped higher than the polysilicon layers. This was unintentionally done during growth (due to the different deposition conditions for polycrystalline $\text{Si}_{1-x-y}\text{Ge}_x\text{C}_y$ vs. polysilicon - 625°C vs. 700°C, respectively), and is not attributable to a segregation effect. Without segregation, however, this profile would be expected to flatten out during the anneal. In the polycrystalline $\text{Si}_{0.8-y}\text{Ge}_{0.2}\text{C}_y$ layers with high carbon levels (0.5 and 1%), however, the boron concentration actually increases during the anneal, revealing that boron segregation to these layers is occurring. In the layers with carbon levels of 0.0% and 0.05%, the boron concentrations are below their initial values, leaving open the possibility that the peaks simply remain due to slow out-diffusion, not segregation. However, given previous reports of diffusion in polycrystalline $\text{Si}_{1-x}\text{Ge}_x$ [3], these anneal conditions should be sufficient to allow for complete out-diffusion, making the remaining peaks most likely due to segregation. In Figure 4.3, the segregation coefficients are presented as a function of carbon content. Segregation to polycrystalline $\text{Si}_{0.8}\text{Ge}_{0.2}$ was weak ($m=1.1$). It then steadily increases for carbon concentrations up to 1%. Also plotted are segregation coefficients for the same sample subjected to a 900°C 100-min anneal (instead of 800°C), showing again reduced segregation at higher temperature. Further annealing at 900°C showed no increase in segregation for this sample as well, consistent with the two-layer case. Assuming an activation energy for boron diffusion of ~3.5 eV (an upper estimate for boron diffusion in polysilicon), anneal times at 800°C of 18 hours should also be long enough to allow for

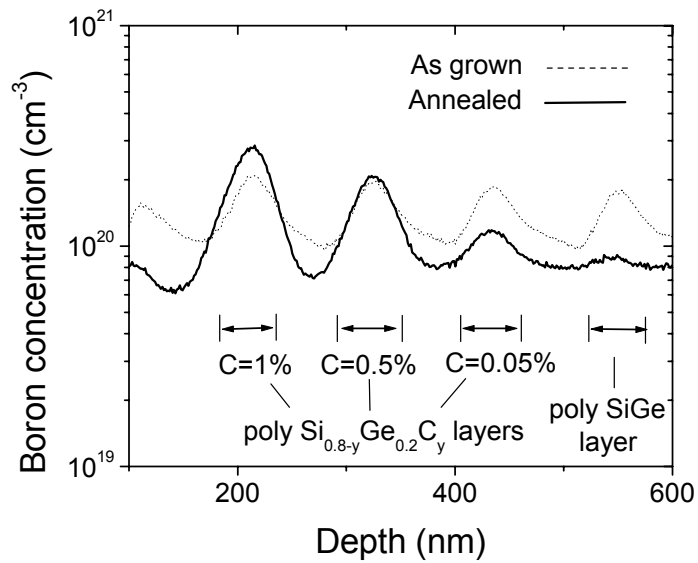


Figure 4.2: SIMS profiles of boron concentration vs. depth for the multi-layer polycrystalline $\text{Si}_{0.8-y}\text{Ge}_{0.2}\text{C}_y$ sample annealed at 800°C for 18 hours.

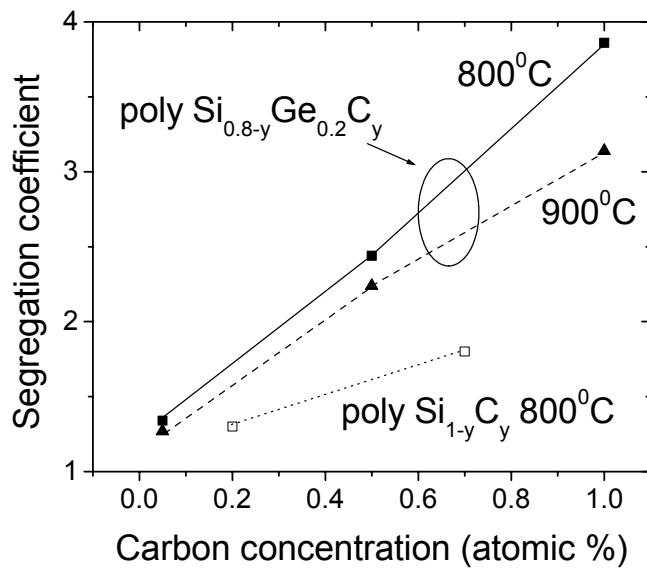


Figure 4.3: Segregation coefficients vs. carbon concentration for the multi-layer polycrystalline $\text{Si}_{0.8-y}\text{Ge}_{0.2}\text{C}_y$ (annealed at 800°C for 18 hours or 900°C for 100 min) and $\text{Si}_{1-y}\text{C}_y$ (annealed at 800°C for 22 hours) samples.

complete segregation (for layers of similar thickness). Therefore we can assume that in Figure 4.2 there has also been enough time to establish a quasi-equilibrium between the layers.

4.3 Test for SIMS artifacts

A separate experiment was carried out to confirm that the observed segregation is not attributable to a SIMS artifact associated with measuring boron in $\text{Si}_{1-x-y}\text{Ge}_x\text{C}_y$ layers with high carbon levels. For example, the carbon might be imagined to somehow raise the yield of boron as detected by SIMS from that of samples without carbon. Three samples were used for this experiment. The first was just a lightly doped ($\sim 1 \times 10^{15} \text{ cm}^{-3}$) n-type silicon substrate. The second sample consisted of an n-type substrate, on top of which was grown a $\sim 80 \text{ nm}$ $\text{Si}_{0.8}\text{Ge}_{0.2}$ layer, followed by a $\sim 50 \text{ nm}$ Si cap (all undoped). The third sample was similar to the second, except a $\text{Si}_{0.79}\text{Ge}_{0.2}\text{C}_{0.01}$ layer was used in place of the $\text{Si}_{0.8}\text{Ge}_{0.2}$. All three samples were then ion-implanted with boron at several doses and energies to create a roughly flat boron profile in each sample from a depth of about 50 nm to 300 nm. The implant conditions were identical for the three samples. No anneals were performed. SIMS measurements of boron were then taken for all three samples, expecting to see similar boron profiles in each (perhaps slightly different profiles are expected in the samples with $\text{Si}_{1-x}\text{Ge}_x$ and $\text{Si}_{1-x-y}\text{Ge}_x\text{C}_y$ layers vs. the all silicon sample, due to a different stopping coefficient for boron in $\text{Si}_{1-x}\text{Ge}_x$ vs. silicon).

If SIMS measurements exaggerate boron levels in the $\text{Si}_{1-x-y}\text{Ge}_x\text{C}_y$ layers, then an anomalous spike in the measured SIMS profile would be expected in the $\text{Si}_{1-x-y}\text{Ge}_x\text{C}_y$

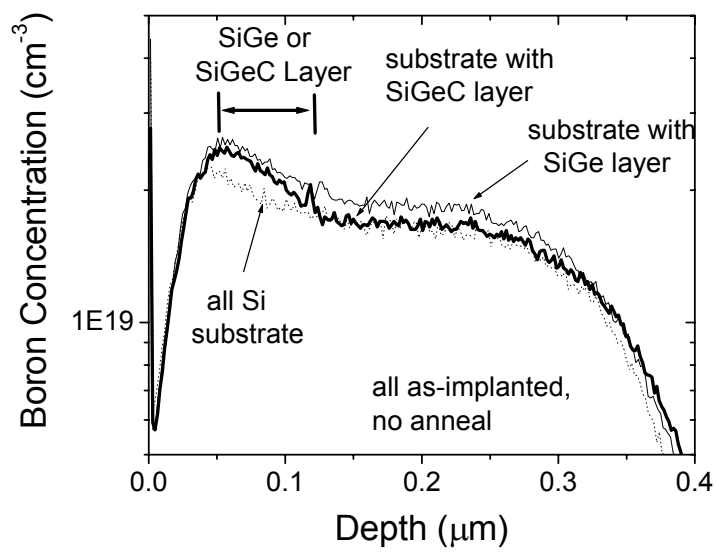


Figure 4.4: SIMS profiles of boron concentration for implanted samples.

layer of this sample. No such spike is observed, however. Figure 4.4 shows the SIMS plots of boron concentration vs. depth for the three samples. All samples have almost indistinguishable profiles, with boron levels rising quickly to $\sim 2 \times 10^{19} \text{ cm}^{-3}$ at 50 nm, leveling off, and then dropping at ~ 300 nm. In particular, no significant difference is seen between the samples with a $\text{Si}_{1-x}\text{Ge}_x$ layer vs. a $\text{Si}_{1-x-y}\text{Ge}_x\text{C}_y$ layer, indicating that SIMS measurements are not exaggerating boron levels in $\text{Si}_{1-x-y}\text{Ge}_x\text{C}_y$ layers with high carbon concentrations. This confirms that the segregation measured by SIMS as shown many times in this thesis is not a measurement artifact.

4.4 Boron segregation to polycrystalline $\text{Si}_{1-y}\text{C}_y$ (no Ge)

An additional sample was grown to study segregation in polycrystalline $\text{Si}_{1-y}\text{C}_y$, containing two *in-situ* doped ($[\text{B}] \sim 7 \times 10^{20} \text{ cm}^{-3}$) polycrystalline $\text{Si}_{1-y}\text{C}_y$ layers (carbon percentages = 0.4 and 1%) sandwiched between polysilicon layers. This sample was annealed at 800°C for 22 hours in N_2 to allow for boron redistribution. SIMS profiles of this sample before and after annealing (Figure 4.5) show that carbon by itself can cause segregation, without germanium present. Boron segregates to the polycrystalline $\text{Si}_{1-y}\text{C}_y$ layers, with coefficients of 1.3 and 1.8 for layers which had initial carbon fractions of 0.4% and 1.0%, respectively. These coefficients, however, are somewhat lower compared to polycrystalline $\text{Si}_{0.8-y}\text{Ge}_{0.2}\text{C}_y$ layers under similar conditions (Figure 4.3).

Another significant difference we observe between $\text{Si}_{1-x-y}\text{Ge}_x\text{C}_y$ and $\text{Si}_{1-y}\text{C}_y$ is that the out-diffusion of carbon from the polycrystalline $\text{Si}_{1-y}\text{C}_y$ layers is faster than from the polycrystalline $\text{Si}_{1-x-y}\text{Ge}_x\text{C}_y$ layers (Figure 4.6). After the anneal, the peak carbon

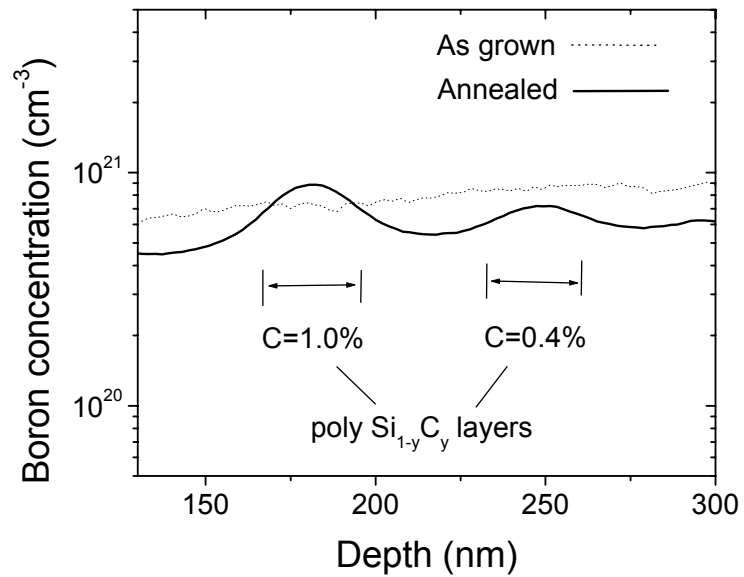
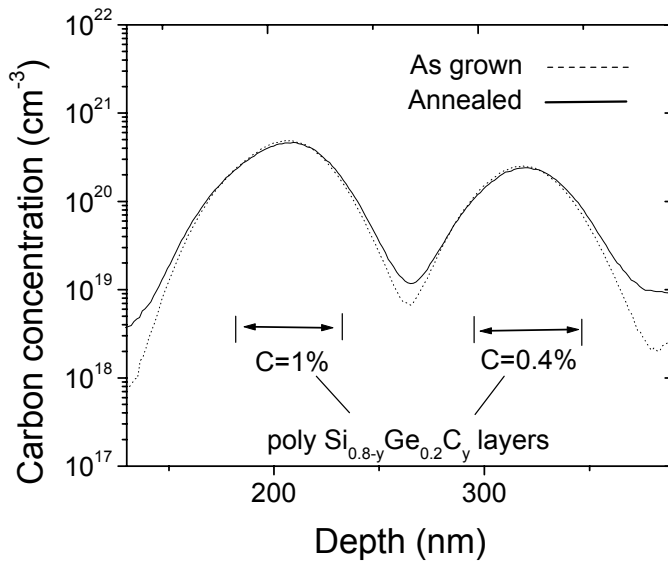
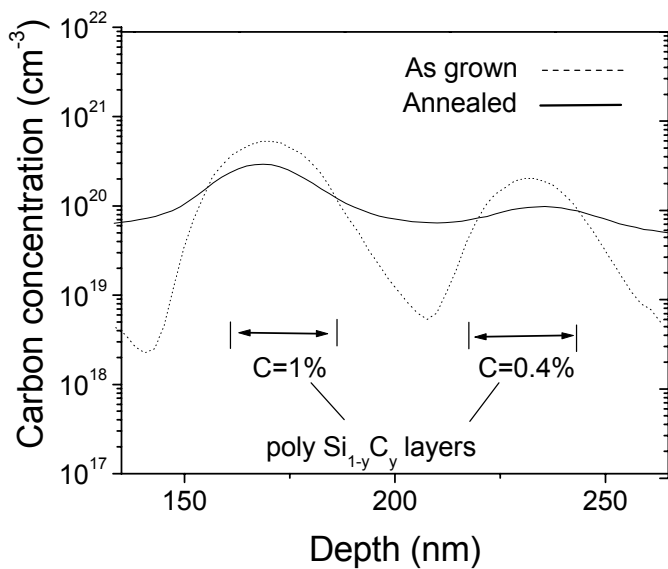


Figure 4.5: SIMS profiles of boron concentration vs. depth for the multi-layer polycrystalline $\text{Si}_{1-y}\text{C}_y$ sample annealed at 800°C for 22 hours. Carbon percentages are given for the as-grown layers.



(a)



(b)

Figure 4.6: SIMS profiles of carbon concentration vs. depth for (a) the multi-layer polycrystalline Si_{0.8-y}Ge_{0.2}C_y sample annealed at 800°C for 18 hours and (b) the multi-layer polycrystalline Si_{1-y}C_y sample annealed at 800°C for 22 hours.

percentages have decreased to 0.2% and 0.7% in the polycrystalline $\text{Si}_{1-y}\text{C}_y$ sample from their initial values of 0.4 and 1.0%, respectively. In the polycrystalline $\text{Si}_{1-x-y}\text{Ge}_x\text{C}_y$ sample, the carbon concentrations remained close to their initial values for the high carbon concentrations (0.5 and 1%). Therefore in Figure 4.3 we plotted the segregation coefficients for the polycrystalline $\text{Si}_{1-y}\text{C}_y$ layers vs. the final carbon concentrations, not the initial values. Nevertheless, the segregation coefficients are still lower than in the polycrystalline $\text{Si}_{1-x-y}\text{Ge}_x\text{C}_y$ layers. It should be noted that the peak doping levels in the $\text{Si}_{1-y}\text{C}_y$ sample are significantly higher than in the polycrystalline $\text{Si}_{1-x-y}\text{Ge}_x\text{C}_y$ sample, $7 \times 10^{20} \text{ cm}^{-3}$ vs. $2 \times 10^{20} \text{ cm}^{-3}$. Thus it is not possible to make a clear statement about the quantitative difference between boron segregation in $\text{Si}/\text{Si}_{1-y}\text{C}_y$ vs. $\text{Si}/\text{Si}_{1-x-y}\text{Ge}_x\text{C}_y$ (for example, boron clustering may be having an effect on the redistribution process [4]). It is also possible that the higher boron levels in the $\text{Si}_{1-y}\text{C}_y$ sample are responsible for the enhanced carbon diffusion. As will be discussed in Chapter 5, the presence of boron can enhance carbon diffusion in single-crystal material. However, further experiments are needed to support this hypothesis.

4.5 Electrical properties of boron-doped polycrystalline $\text{Si}_{1-x-y}\text{Ge}_x\text{C}_y$

4.5.1 Data

A separate set of samples was used to investigate the electrical properties of boron-doped polycrystalline $\text{Si}_{1-x-y}\text{Ge}_x\text{C}_y$ layers. Single layers of *in-situ* doped polycrystalline Si, $\text{Si}_{0.75}\text{Ge}_{0.25}$, and $\text{Si}_{0.75-y}\text{Ge}_{0.25}\text{C}_y$ were grown using recipes Si:2,

$\text{Si}_{1-x}\text{Ge}_x$:2, and $\text{Si}_{1-x-y}\text{Ge}_x\text{C}_y$:2 from Appendix A, all on thermally oxidized (~ 200 nm) silicon substrates. Thicknesses ranged from 150-300 nm. Doping levels ranged from 10^{18} to 10^{21} cm^{-3} and carbon levels from 0 to 1.6%. All samples were annealed at 900°C for times similar to or longer than those used to study segregation in the previous sections. This was done to examine what effect the segregation process may be having on the electrical properties (i.e. possible formation of inactive boron-carbon defects). Boron and carbon levels were determined by SIMS, and resistivity, dopant activation, and mobility measurements were taken using the four-point probe and Van der Pauw techniques at room temperature.

Figure 4.7 shows the as-deposited dopant activation (hole concentration divided by total boron as measured by SIMS) and hole mobility for polycrystalline $\text{Si}_{1-x-y}\text{Ge}_x\text{C}_y$ samples doped at a level of 2×10^{19} cm^{-3} , as a function of carbon content. The same silane, germane, and diborane flows were used for all three samples; only the methylsilane flow was varied for the different carbon levels. Boron concentrations were measured by SIMS, and showed that the boron incorporation is not significantly affected by the methylsilane flow. As-deposited polycrystalline $\text{Si}_{1-x}\text{Ge}_x$ (no carbon) has a resistivity of 7.6×10^{-2} ohm-cm and mobility of 7.1 $\text{cm}^2/\text{V-s}$, comparable to previous reports at these doping levels [3]. Polysilicon samples (doped at 1×10^{19} cm^{-3} , not shown) had similar dopant activation but lower mobilities (2.9 $\text{cm}^2/\text{V-s}$). When low carbon concentrations (0.4%) are added to polycrystalline $\text{Si}_{1-x}\text{Ge}_x$, there is a slight increase in hole concentration, but the change is less than the error bars of the measurement. There was also a small decrease in the mobility (17%). As the carbon level is increased to 1.6%, however, significant losses in both dopant activation (32%) and mobility (49%) vs.

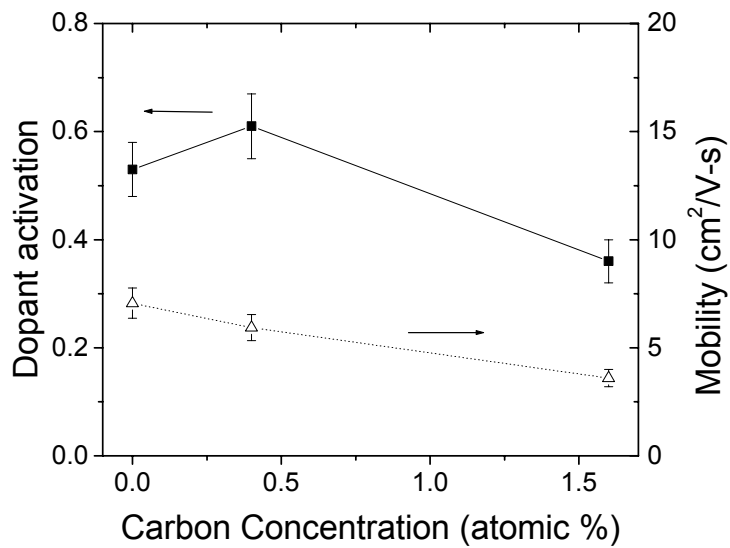


Figure 4.7: Dopant activation and mobility as a function of carbon concentration for the as-grown (no annealing) polycrystalline $\text{Si}_{0.75-y}\text{Ge}_{0.25}\text{C}_y$ single-layer samples doped with boron at $2 \times 10^{19} \text{ cm}^{-3}$.

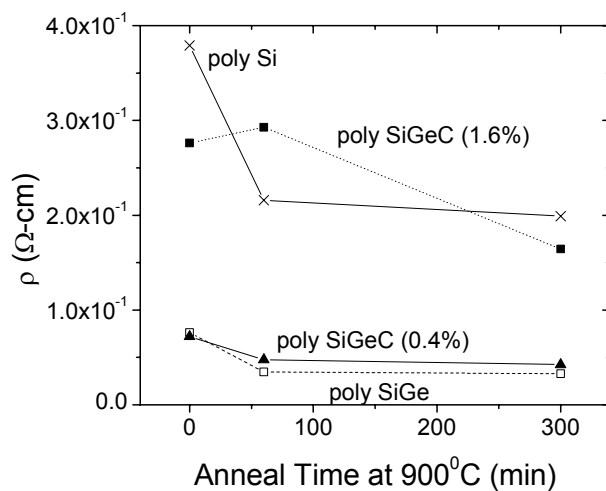
the polycrystalline $\text{Si}_{1-x}\text{Ge}_x$ sample are observed.

The electrical properties are fairly stable with annealing. Figure 4.8 shows resistivity, dopant activation, and mobility vs. annealing at 900°C for the $2 \times 10^{19} \text{ cm}^{-3}$ doped samples from Figure 4.7. The polysilicon sample doped at $1 \times 10^{19} \text{ cm}^{-3}$ is also included. Dopant activation remains mostly flat for all annealing times and carbon levels. Mobilities increase at first, presumably due to increases in grain size, and then stabilize. As a result, resistivities initially decrease and then level off. Resistivity measurements (although not Hall measurements to find mobility) were also taken out to 24 hours of annealing, and remained stable.

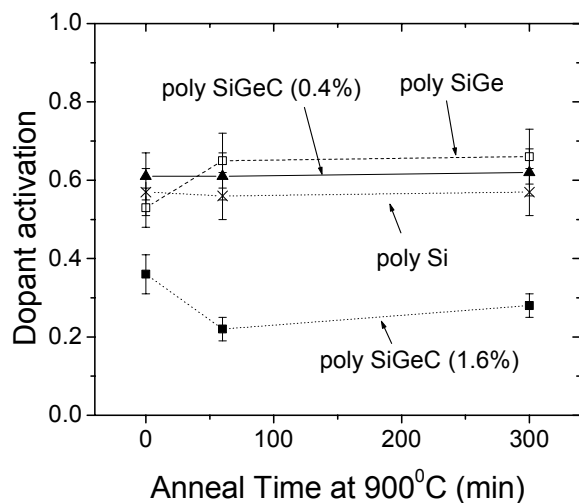
Figure 4.9 shows the resistivity of the as-grown samples as a function of doping concentration. For low carbon levels (0.4% at 10^{19} doping and 0.6% at 10^{21} doping), polycrystalline $\text{Si}_{1-x-y}\text{Ge}_x\text{C}_y$ resistivities are similar to those of the polycrystalline $\text{Si}_{1-x}\text{Ge}_x$. However, for the high carbon levels (1.6%), they are larger over the entire range of doping. The magnitude of this increase depends on doping level: it is largest at low doping ($\sim 50X$ at 10^{18} cm^{-3}) and smaller at higher doping ($\sim 2.5X$ at 10^{20} cm^{-3}). Long anneals (900°C for several hours) were performed over all doping levels and, similar to Figure 6, the resistivities initially decreased for all samples and then stabilized.

4.5.2 Discussion

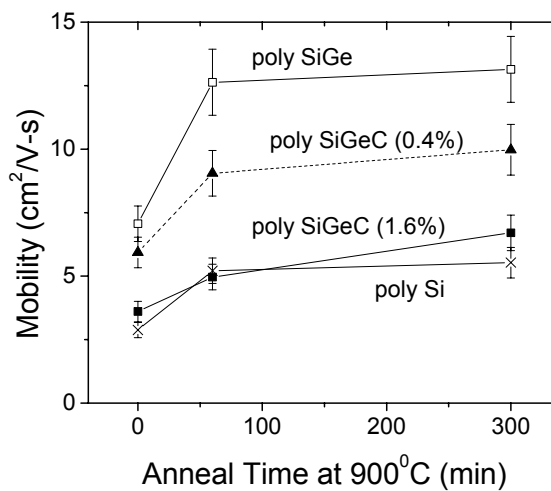
When small amounts of carbon (less than 2%) are added to single-crystal silicon or $\text{Si}_{1-x}\text{Ge}_x$, most reports have found that (for boron doping) dopant activation is not affected, but mobilities decrease by factors ranging from 11-60% [5-7]. The mobility



(a)



(b)



(c)

Figure 4.8: (a) Resistivity, (b) dopant activation, and (c) mobility as a function of anneal time at 900°C for the polycrystalline $\text{Si}_{1-x-y}\text{Ge}_x\text{C}_y$ single-layer samples doped at $2 \times 10^{19} \text{ cm}^{-3}$. Also included are the measurements for polysilicon doped at $1 \times 10^{19} \text{ cm}^{-3}$.

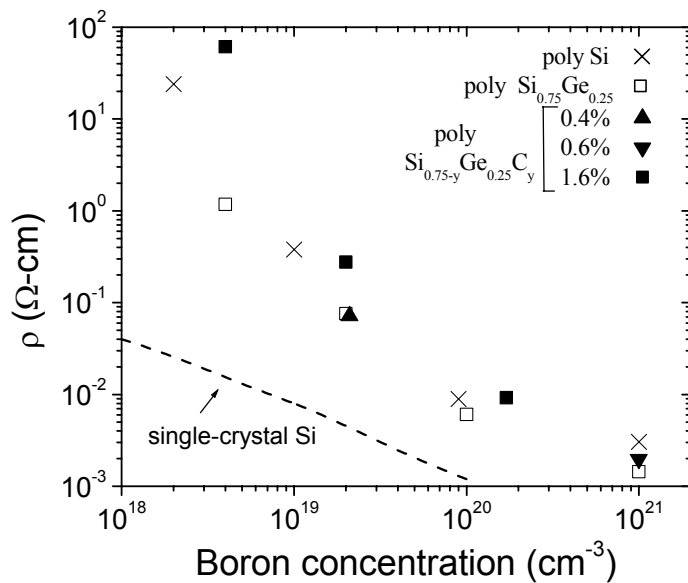


Figure 4.9: Resistivity vs. boron concentration (from SIMS) for as-grown polycrystalline Si, $\text{Si}_{0.75}\text{Ge}_{0.25}$, and $\text{Si}_{0.75-y}\text{Ge}_{0.25}\text{C}_y$ samples. Also shown is the data for single-crystal silicon (dotted line) from [8].

drop has been attributed to increased scattering due to the presence of the carbon, either by electrically active defects or alloy scattering.

Conduction in polycrystalline material is different from the single-crystal case due to (i) dopant segregation to grain boundaries, where it becomes electrically inactive, and (ii) carrier trapping at grain boundaries. The first effect (segregation) is not expected to be important for boron-doped films. While some dopants, such as phosphorus, have been observed to segregate to grain boundaries in polycrystalline Si and $\text{Si}_{1-x}\text{Ge}_x$, no such segregation is seen for boron [9, 10]. The second effect (carrier trapping), however, will have a significant impact. Grain boundaries introduce large numbers of states close to the middle of the energy gap, which can effectively trap majority carriers [11]. This itself has two effects on the conductivity. First, the trapped carriers no longer contribute to conductivity. Second, the grain boundaries become charged and potential barriers form, which impede the flow of the remaining carriers between grains and reduce the effective mobility. This becomes worse as the grain size is reduced, the trap density is increased, or the doping level is reduced. At low doping levels, the grain boundaries can trap a large fraction of the carriers and the potential barriers become very high, so the difference in resistivity vs. single-crystal layers of similar doping can be very high. As doping level is increased, the potential barriers become narrower and lower, and a smaller fraction of carriers are trapped, so the conductivity approaches that of single-crystal Si. Our overall results are consistent with these models (Figure 4.9). At the 10^{18} cm^{-3} doping level, the polysilicon resistivity is several orders of magnitude higher than in single-crystal. Resistivity decreases rapidly as boron concentration is increased above this level, and

approaches single-crystal values (with similar doping) in the 10^{20} - 10^{21} cm^{-3} range (for comparison, the single-crystal resistivity is plotted vs. boron doping in Figure 4.9 [8]).

Boron-doped polycrystalline $\text{Si}_{1-x}\text{Ge}_x$ is known to have lower resistivity than polysilicon [3, 12]. This difference has been attributed to a larger grain size and a shift of the trap states towards the valence band, resulting in less carrier trapping and an increased mobility. Our results are consistent with these observations as well, with our polycrystalline $\text{Si}_{1-x}\text{Ge}_x$ samples (doped at the 2×10^{19} cm^{-3} level) having about 2.5 times higher mobility than polysilicon (Figure 4.8(c)).

Our as-deposited polycrystalline $\text{Si}_{1-x-y}\text{Ge}_x\text{C}_y$ samples with low carbon concentration (0.4%) have similar dopant activation and only a slightly decreased mobility compared to polycrystalline $\text{Si}_{1-x}\text{Ge}_x$ (Figure 4.7). The mobility decrease may be due to the previously mentioned carbon-induced scattering seen in single-crystal films with similar carbon levels. This is not due to a decrease in compressive strain, as might occur in pseudomorphically strained layers, because these are single polycrystalline layers grown on oxides. This retention of most of the electrical properties of polycrystalline $\text{Si}_{1-x}\text{Ge}_x$ makes low-carbon polycrystalline $\text{Si}_{1-x-y}\text{Ge}_x\text{C}_y$ attractive for device applications, such as MOSFET gates. However, the layers with high carbon concentrations (1.6%) have a large decrease both in carrier activation and mobility. This was seen in one previous report, and attributed to an increase in the trap density at the grain boundaries caused by carbon [13]. An increased trap density would trap a much larger fraction of the active carriers, reducing the carrier concentration, and form larger potential barriers, reducing the mobility. The fact that resistivity difference (vs. polysilicon or polycrystalline $\text{Si}_{1-x}\text{Ge}_x$) increases more rapidly with decreasing doping

level (Figure 4.9) for the 1.6% polycrystalline $\text{Si}_{1-x-y}\text{Ge}_x\text{C}_y$ layer is consistent with this model. At low doping, a difference in trap density will have a larger effect on the resistivity because a larger fraction of the carriers are being trapped, and the potential barriers are more sensitive to the trap density. However, it cannot be ruled out that some sort of B-C defect is incorporated as-grown in the grain and directly renders the boron inactive.

The stability of the electrical properties with annealing provides insight into the mechanism of boron segregation. One potential driving mechanism is that boron is becoming trapped at a carbon-related defect. For example, silicon carbide (SiC) precipitates are known to form in $\text{Si}_{1-x-y}\text{Ge}_x\text{C}_y$ layers with similar carbon levels and annealing conditions [14, 15], and boron could become immobilized either inside or at the surfaces of these defects. A direct interaction between boron and carbon might also be occurring, such as the B-C-I cluster proposed by Liu et al [16]. Either of these defects might be expected to render the boron electrically inactive. This should be detectable by the electrical measurements in the single-layer polycrystalline $\text{Si}_{1-x-y}\text{Ge}_x\text{C}_y$ films - as they are annealed and given time to form B-C defects, one would expect to see a loss in the concentration of electrically active boron. However, as shown in Figure 4.8, this is not observed. For both the polycrystalline $\text{Si}_{0.746}\text{Ge}_{0.25}\text{C}_{0.004}$ and $\text{Si}_{0.734}\text{Ge}_{0.25}\text{C}_{0.016}$ samples, no significant loss in dopant activation is observed as a function of annealing. Thus boron is not moving to electrically inactive sites either within the grains or at the grain boundaries. For both carbon concentrations, however, under same annealing conditions, significant boron segregation is observed. This argues against boron-carbon defects or

defect complexes as the driving force for boron segregation to polycrystalline $\text{Si}_{1-x-y}\text{Ge}_x\text{C}_y$ from Si.

4.6 Effect of segregation on the suppression of boron penetration in MOS structures

As discussed in the previous chapter, the segregation of boron to polycrystalline $\text{Si}_{1-x-y}\text{Ge}_x\text{C}_y$ appears to be responsible for the reduction of boron penetration observed in those devices. Boron accumulates in the polycrystalline $\text{Si}_{1-x-y}\text{Ge}_x\text{C}_y$ layers, with less penetration through the gate oxide and into the channel. These devices thus have greater threshold voltage stability. Here, using the segregation data presented in this chapter, we model this effect quantitatively. In particular, we investigate two questions: (i) is the segregation observed here powerful enough to reduce boron penetration as found in the previous chapter, and (ii) what happens as the carbon level is varied in the polycrystalline Si/ $\text{Si}_{1-x-y}\text{Ge}_x\text{C}_y$ gate?

Using the TSUPREM4 process simulator, we performed the same simulations as discussed in Section 3.3.2 of the previous chapter, except that instead of altering the boron diffusivity, we established a segregation coefficient for boron in polycrystalline $\text{Si}_{1-x-y}\text{Ge}_x\text{C}_y$ vs. polysilicon, and kept the diffusivity fixed. In TSUPREM4, the dopant flux across an interface between two materials A and B is defined as:

$$F_{AB} = h_{AB} \left(\frac{C_A}{m_{AB}} - C_B \right) \quad (4.1)$$

where F_{AB} is the flux from material A into material B (negative if in opposite direction), C_A and C_B are the dopant concentrations in materials A and B, respectively, h_{AB} is the interface transport coefficient, and m_{AB} is the segregation coefficient. Increasing m_{AB} causes the dopant to prefer moving into material A vs. material B, and eventually if left to establish equilibrium ($F_{AB} = 0$):

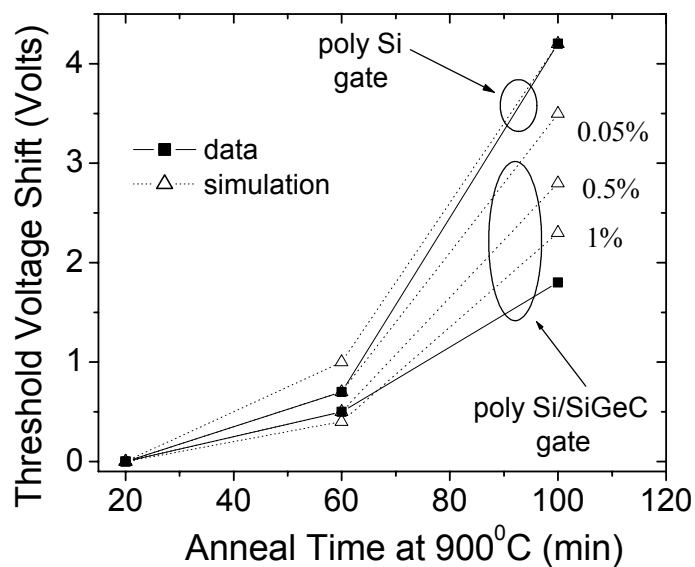
$$\frac{C_A}{C_B} = m_{AB} \quad (4.2)$$

Thus increasing the segregation coefficient causes the dopant to pile up in material A vs. B, or in our case, in polycrystalline $\text{Si}_{1-x-y}\text{Ge}_x\text{C}_y$ vs. polysilicon. If there is a third material C (e.g. oxide), we assume the segregation coefficient m_{AC} between material A and C increases by the same amount. As a result, by increasing boron segregation between polycrystalline $\text{Si}_{1-x-y}\text{Ge}_x\text{C}_y$ and polysilicon, boron will also be more likely to stay in a polycrystalline $\text{Si}_{1-x-y}\text{Ge}_x\text{C}_y$ layer vs. an oxide. This is a key assumption necessary to see the reduced boron penetration.

Similar to the previous chapter, structures identical to our MOSFETs (Figure 4.10(a)) were simulated and subjected to the same process conditions as in experiment (60 keV BF_2^+ implant at $2 \times 10^{15} \text{ cm}^{-2}$, 900°C anneals for 20, 60 and 100 minutes). The resulting dopant profiles were then inputted into the device simulator MEDICI and threshold voltages extracted. Carbon levels of 0.05%, 0.5%, and 1% in the polycrystalline $\text{Si}_{1-x-y}\text{Ge}_x\text{C}_y$ layer were modeled using segregation coefficients at 900°C taken from Figure 4.3 (1.27, 2.23, and 3.14, respectively).

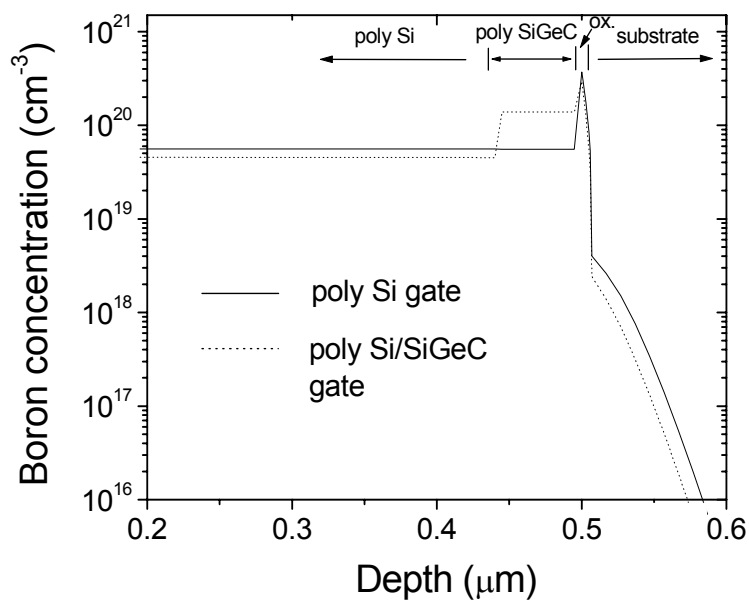
poly Si	440 nm
poly SiGeC	60 nm
gate oxide	7 nm
n-type substrate	

(a)

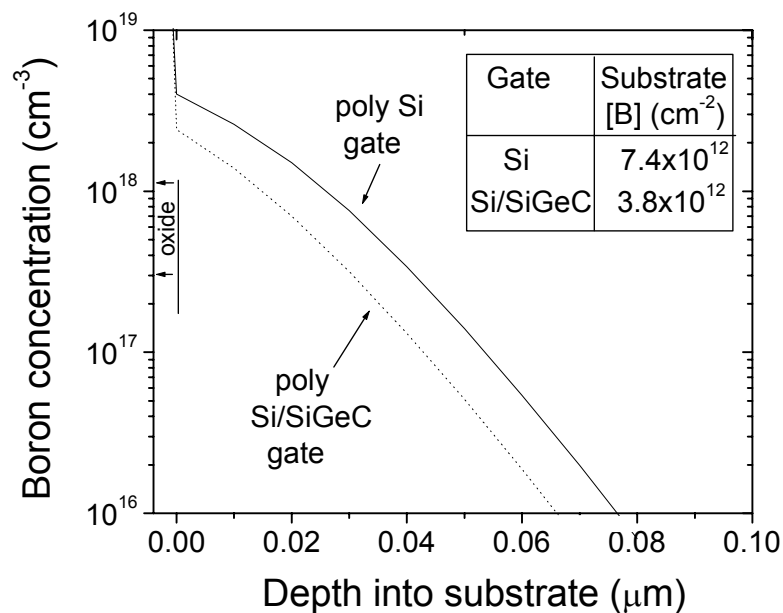


(b)

Figure 4.10: Simulated (a) structure and (b) threshold voltage shifts vs. anneal time for PMOS devices with polycrystalline Si/Si_{1-x-y}Ge_xC_y gates. Solid symbols and lines represent experimental data (for the experimental polycrystalline Si/Si_{1-x-y}Ge_xC_y sample, the carbon content was 0.35%), and open symbols and dotted lines represent the simulations.



(a)



(b)

Figure 4.11: (a) Simulated boron profiles for either a polycrystalline $\text{Si/Si}_{1-x-y}\text{Ge}_x\text{C}_y$ ($C=1.0\%$, $m=3.14$) gate or all-polysilicon gate, after 100 minutes of annealing at 900°C . (b) Blowup of the boron profiles in the substrate for the two cases shows reduced boron penetration for the polycrystalline $\text{Si/Si}_{1-x-y}\text{Ge}_x\text{C}_y$ gate structure (inset shows integrated boron in the substrate).

The simulations show that the segregation strongly suppresses boron penetration and increases threshold voltage stability, noticeable even at carbon levels of only 0.05% (Figure 4.10(b)). Larger effects are seen at carbon levels of 0.5% and 1.0%. Figure 4.11(a) shows simulated boron profiles in the gate and substrate of a high-carbon ($C=1.0\%$, $m=3.14$) polycrystalline $\text{Si}/\text{Si}_{1-x-y}\text{Ge}_x\text{C}_y$ gate device after 100 minutes of annealing, compared to an all-polysilicon gate. Boron segregation to the simulated polycrystalline $\text{Si}_{1-x-y}\text{Ge}_x\text{C}_y$ layer is clearly seen. Figure 4.11(b) shows a blowup of the boron profiles in the substrate for the two cases, showing substantially less boron penetration predicted for the polycrystalline $\text{Si}/\text{Si}_{1-x-y}\text{Ge}_x\text{C}_y$ case.

If the simulated threshold voltage results are compared to the experimental results for the polycrystalline $\text{Si}/\text{Si}_{1-x-y}\text{Ge}_x\text{C}_y$ gate (by linearly interpolating the segregation values for 0.35% carbon), we find that the simulation predicts improved threshold voltage stability, but not as much as in the physical experiment of Chapter 3. Additional effects, or limitations of the manner in which we are modeling the segregation, may be the cause of this discrepancy. For example, a reduced boron diffusivity in combination with segregation effects may play a larger role than just the lower diffusivity alone as in Chapter 3.

We conclude from this analysis that boron segregation to polycrystalline $\text{Si}_{1-x-y}\text{Ge}_x\text{C}_y$ appears capable of giving rise to the observed increase in threshold voltage stability seen in our MOSFET structures. While quantitative agreement is not exact, this mechanism has a much bigger impact than simply decreasing the boron diffusivity as in Chapter 3. Higher carbon levels (at least up to 1%) in the polycrystalline $\text{Si}_{1-x-y}\text{Ge}_x\text{C}_y$ layer provide increased resistance to boron penetration. However, as shown in Figure

4.7, high carbon concentrations will eventually degrade the conductivity of the polycrystalline $\text{Si}_{1-x-y}\text{Ge}_x\text{C}_y$ layers, resulting in a potential tradeoff between gate conductivity and threshold voltage stability.

4.7 Summary

In summary, we find that boron segregates from polysilicon to both polycrystalline $\text{Si}_{1-x-y}\text{Ge}_x\text{C}_y$ and $\text{Si}_{1-y}\text{C}_y$ layers during thermal anneals. The effect is strongly dependent on carbon, occurs with or without germanium present, and is not due to any SIMS artifacts. Electrical properties show that polycrystalline $\text{Si}_{1-x-y}\text{Ge}_x\text{C}_y$ layers with low carbon content (0.4%) retain most of the electrical properties of polycrystalline $\text{Si}_{1-x}\text{Ge}_x$. This makes low-carbon films attractive for device applications, such as MOSFET gates. Increasing the carbon level to 1.6%, however, causes significant degradations in the conductivity. The stability of the electrical properties, for all carbon levels, indicates that electrically inactive boron-carbon defects are not responsible for the segregation. The segregation appears largely responsible for the increased threshold voltage stability of our MOSFET structures from Chapter 3. The mechanism driving the segregation, however, is still not known. Therefore, in the following chapters, we investigate driving mechanisms for the segregation.

4.8 References

- [1] C.W. Liu, A. St. Amour, J.C. Sturm, Y.R.J. Lacroix, M.L.W. Thewalt, C.W. Magee, and D. Eaglesham, *Journal of Applied Physics*, vol. 80(5), 3043-3047 (1996).
- [2] M.S. Carroll and J.C. Sturm, *Applied Physics Letters*, vol. 81(7), p. 1225-1227 (2002).
- [3] C. Salm, D.T. van Veen, D.J. Gravesteijn, J. Holleman, and P.H. Woerlee, *Journal of the Electrochemical Society*, vol. 144 (10), p. 3665-3673 (1997).
- [4] S. Solmi, E. Landi, and F. Baruffaldi, *Journal of Applied Physics*, vol. 68(7), p. 3250-3258 (1990).
- [5] H.J. Osten, G. Lippert, P. Gaworzewski, and R. Sorge, *Applied Physics Letters*, vol. 71(11), p. 1522-1524 (1997).
- [6] H. J. Osten and P. Gaworzewski, *Journal of Applied Physics*, vol. 82(10), p. 4977-4981 (1997).
- [7] T. Noda, D. Lee, H. Shim, M. Sakuraba, T. Matsuura, and J. Murota, *Thin Solid Films*, vol. 380, p. 57-60 (2000).
- [8] S.M. Sze, *Physics of Semiconductor Devices* (John Wiley and Sons, New York, 1981), p. 32.
- [9] W. Qin, D.G. Ast, and T.I. Kamins, *Journal of Electronic Materials*, vol. 29(8), L13-L17 (2000).
- [10] M.M. Mandurah, K.C. Saraswat, C.R. Helms, and T.I. Kamins, *Journal of Applied Physics*, vol. 51(11), p. 5755-5763 (1981).
- [11] T. I. Kamins, *Journal of Applied Physics*, vol. 42(11), p. 4357-4365 (1971).
- [12] T.-J. King, J. P. McVittie, K.C. Saraswat, and J.R. Pfiester, *IEEE Transactions on Electron Devices*, vol. 41(2), p. 228-232 (1994).
- [13] I.M. Anteney, G.J. Parker, P. Ashburn, and H.A. Kemhadjian, *Journal of Applied Physics*, vol. 90(12), p. 6182-6189 (2001).
- [14] L.V. Kulik, D.A. Hits, M.W. Dashiell, and J. Kolodzey, *Applied Physics Letters*, vol. 72(16), p. 1972-1974 (1998).
- [15] P. Warren, J. Mi, F. Overney, and M. Dutoit, *Journal of Crystal Growth*, vol. 157, p. 414-419 (1995).
- [16] C.-L. Liu, W. Windl, L. Borucki, S. Lu, and X.-Y. Liu, *Applied Physics Letters*, vol. 80(1), p. 52-54 (2002).

Chapter 5: Boron segregation and driving mechanisms in single-crystal $\text{Si}_{1-x-y}\text{Ge}_x\text{C}_y$ and $\text{Si}_{1-y}\text{C}_y$

5.1 Introduction

In the previous chapter, boron segregation to polycrystalline $\text{Si}_{1-x-y}\text{Ge}_x\text{C}_y$ and $\text{Si}_{1-y}\text{C}_y$ was characterized, focusing on how it affects boron out-diffusion and electrical properties in MOSFET gates. In the next two chapters, the physical mechanisms driving this segregation are considered in detail. This investigation is important not just for this work, but also for the application of $\text{Si}_{1-x-y}\text{Ge}_x\text{C}_y$ alloys in general. As $\text{Si}_{1-x-y}\text{Ge}_x\text{C}_y$ is being either used or considered for a variety of applications, such as HBTs and MOSFET channels and source/drains, it is important to have a full understanding of the mechanisms by which carbon affects dopant transport, including any potential interactions between carbon and dopants. This is essential for optimizing device structures, determining if carbon has any deleterious effects on devices (such as electrical deactivation of boron through defect formation), and investigating potential new applications.

In this chapter, boron segregation in single-crystal $\text{Si}_{1-x-y}\text{Ge}_x\text{C}_y$ and $\text{Si}_{1-y}\text{C}_y$ is first studied to confirm that the segregation observed in the previous chapter is not simply due to a polycrystalline effect (i.e. an interaction of boron and carbon at grain boundaries). This also represents a simpler system to study from a theoretical point of view, as there are no grain boundaries influencing the diffusion, and properties like strain are well

known. Potential driving mechanisms for segregation are then considered. Electrical measurements, as well as a test for immobile boron, are conducted to further investigate whether boron-carbon defects are forming. Finally, the effect of boron on carbon diffusion is considered. In short, no standard models for segregation can be used to explain the segregation of boron to $\text{Si}_{1-x-y}\text{Ge}_x\text{C}_y$ and $\text{Si}_{1-y}\text{C}_y$ from silicon observed in this thesis. A model presenting gradients of silicon interstitials as a driving force for boron segregation is then developed in the next chapter.

5.2 Boron segregation to single crystal $\text{Si}_{1-x-y}\text{Ge}_x\text{C}_y$

All samples used in this chapter were grown by Rapid Thermal Chemical Vapor Deposition using SiCl_2H_2 and Si_2H_6 as silicon sources and GeH_4 , SiCH_6 , and B_2H_6 as sources for germanium, carbon, and boron, respectively. $\text{Si}_{1-x-y}\text{Ge}_x\text{C}_y$ and $\text{Si}_{1-y}\text{C}_y$ layers were grown at 625°C , while silicon was deposited at temperatures ranging from 625°C - 750°C . Previous work shows that for films grown under similar conditions most of the carbon is incorporated substitutionally [1,2]. Two structures were used to study segregation in single-crystal $\text{Si}_{1-x-y}\text{Ge}_x\text{C}_y$, shown in Figure 5.1. For both of these structures, silicon was grown using recipe Si:1, and $\text{Si}_{1-x}\text{Ge}_x$ and $\text{Si}_{1-x-y}\text{Ge}_x\text{C}_y$ recipes $\text{Si}_{1-x}\text{Ge}_x:1$ and $\text{Si}_{1-x-y}\text{Ge}_x\text{C}_y:1$, respectively, from Appendix A. For the first sample (Figure 5.1(a)), thin (15 nm) epitaxial layers of lightly-doped $\text{Si}_{0.8}\text{Ge}_{0.2}$ and $\text{Si}_{0.79}\text{Ge}_{0.2}\text{C}_{0.01}$ were sandwiched between thicker (100 nm) heavily-doped Si layers ($[\text{B}]=2\times 10^{19} \text{ cm}^{-3}$), all on top of an n-type substrate and buffer. This structure was annealed at 800°C for 28 hours to allow boron to move from the silicon into the $\text{Si}_{1-x}\text{Ge}_x$

p^+ Si	150 nm
$Si_{1-x-y}Ge_xC_y$	15 nm
p^+ Si	100 nm
$Si_{1-x}Ge_x$	15 nm
p^+ Si	100 nm
Si buffer	
Si (100) substrate	

(a)

p^+ Si	120 nm
p^+ $Si_{1-x-y}Ge_xC_y$	25 nm
p^+ Si	120 nm
p^+ $Si_{1-x}Ge_x$	25 nm
p^+ Si	120 nm

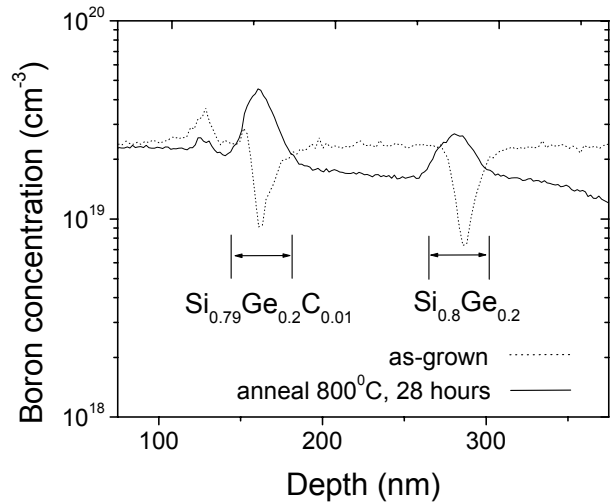
(b)

Figure 5.1: Schematic of structures used to study boron segregation in single-crystal $Si_{1-x-y}Ge_xC_y$ for (a) high-carbon content (1%) and (b) low carbon content (0.05%).

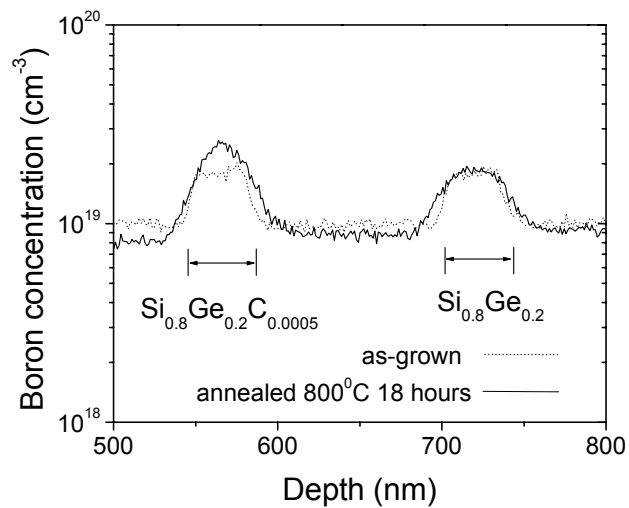
and $\text{Si}_{1-x-y}\text{Ge}_x\text{C}_y$ layers. The second sample (Figure 5.1(b)) was similar to the first, except that the $\text{Si}_{1-x}\text{Ge}_x$ and $\text{Si}_{1-x-y}\text{Ge}_x\text{C}_y$ layers were thicker (25 nm), initially doped higher (not lower) than the silicon, and the carbon level was much lower (0.05%). (There were several other layers on either side of the region of interest, which did not affect our study and are not discussed here.) This sample was annealed for 18 hours at 800°C.

Figure 5.2 shows SIMS of these two structures before and after annealing. For the first sample (Figure 5.2(a)), the $\text{Si}_{1-x}\text{Ge}_x$ and $\text{Si}_{1-x-y}\text{Ge}_x\text{C}_y$ layers initially have much less dopant than the surrounding silicon. After the anneal, however, boron has moved into these layers, and reached levels higher than the original silicon concentration. Defining a segregation coefficient m as the ratio of boron in the $\text{Si}_{1-x}\text{Ge}_x$ vs. Si after the anneal, we find $m=1.7$ for the $\text{Si}_{1-x}\text{Ge}_x$ layer. Boron segregation to $\text{Si}_{1-x}\text{Ge}_x$ is well-known, and the magnitude of this result is consistent with previous reports [3,4]. However, additional segregation occurs in the $\text{Si}_{1-x-y}\text{Ge}_x\text{C}_y$ layer ($m=2.3$), showing that carbon enhances the effect. This confirms that the enhanced segregation to polycrystalline $\text{Si}_{1-x-y}\text{Ge}_x\text{C}_y$ seen in the previous chapter is not (at least exclusively) due to polycrystalline or grain boundary effects. (Note: In the as-grown profile there is a boron peak in the top Si layer ~120 nm from the surface. This was unintentionally incorporated during growth, and should not affect the rest of the experiment.)

The second sample (Figure 5.2(b)) demonstrates a similar effect at a much lower carbon concentration (0.05%). As mentioned above, the as-grown profiles show that during growth a higher boron concentration was initially placed in the $\text{Si}_{1-x}\text{Ge}_x$ and $\text{Si}_{1-x-y}\text{Ge}_x\text{C}_y$ layers compared to the silicon. This would normally be expected to flatten out during the anneal. As shown in Figure 5.2(b), however, boron concentration in the



(a)



(b)

Figure 5.2: SIMS profiles of boron concentration before and after annealing for (a) the high-carbon sample and (b) the low-carbon sample.

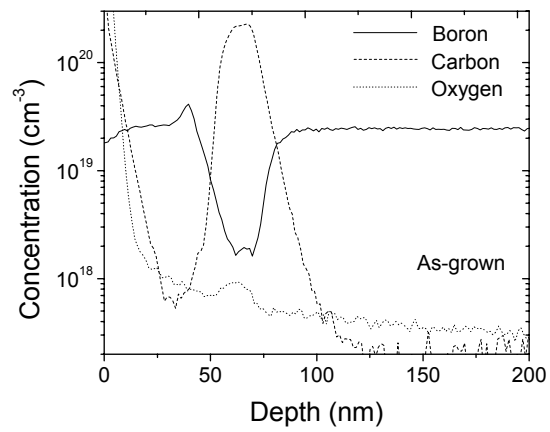
$\text{Si}_{1-x-y}\text{Ge}_x\text{C}_y$ layer actually *increases* during the anneal, again indicating segregation. It is interesting to note that although the carbon concentration is much lower in this sample, the amount of segregation is actually higher ($m=2.9$) than before.

5.3 Boron segregation to single crystal $\text{Si}_{1-y}\text{C}_y$

A third sample was grown to study boron segregation in $\text{Si}_{1-y}\text{C}_y$, whose structure and as-grown SIMS profile are shown in Figure 5.3. On top of an n-type (100) substrate, a 500 nm buffer layer was first grown, followed by a sandwich structure consisting of a thin (20 nm) $\text{Si}_{0.996}\text{C}_{0.004}$ layer in between two boron-doped ($[\text{B}] = 2 \times 10^{19} \text{ cm}^{-3}$) silicon layers. The top and bottom p^+ silicon layers were 50 nm and 150 nm thick, respectively. Silicon and $\text{Si}_{1-y}\text{C}_y$ were grown using recipes Si:1 and $\text{Si}_{1-y}\text{C}_y:1$, respectively, from Appendix A. This sample was annealed at 850°C for up to 2 hours in N_2 , and SIMS profiles were measured (Figure 5.4). After 30 minutes boron is clearly seen moving into the $\text{Si}_{1-y}\text{C}_y$ layer, although more on the top of the layer than on the bottom. After 2 hours of annealing, similar to the $\text{Si}_{1-x-y}\text{Ge}_x\text{C}_y$ case, boron segregates into the $\text{Si}_{1-y}\text{C}_y$ layer, reaching a value 1.7X higher than the surrounding silicon. Some boron is also being lost out the surface of the sample due to evaporation. Oxygen concentrations, shown in both Figure 5.3 and 5.4, are well below the boron and carbon concentrations, and no oxygen accumulation is observed in the $\text{Si}_{1-y}\text{C}_y$ layer during the anneal. This data for single-crystal $\text{Si}_{1-y}\text{C}_y$, and that in the previous section for single-crystal $\text{Si}_{1-x-y}\text{Ge}_x\text{C}_y$, clearly show boron segregation in these films. We now examine

p ⁺ Si	50 nm
Si _{0.996} C _{0.004}	20 nm
p ⁺ Si	150 nm
buffer	
n-type substrate	

(a)



(b)

Figure 5.3. (a) Structure and (b) SIMS profiles of as-deposited Si/Si_{1-y}C_y/Si sandwich structure.

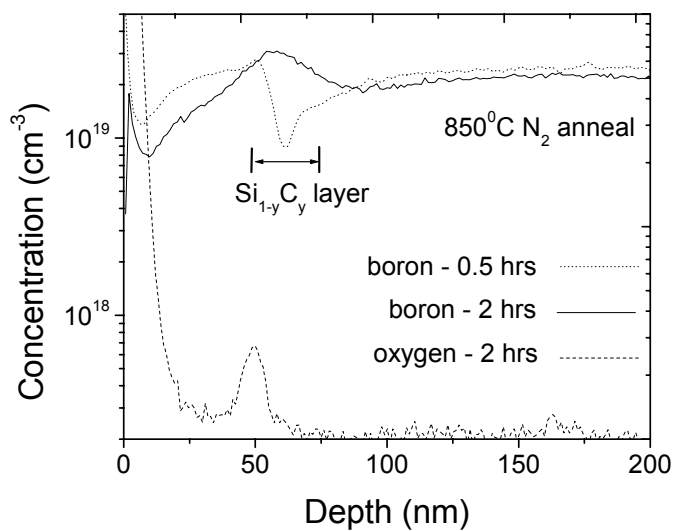


Figure 5.4. SIMS profiles of boron concentration after nitrogen annealing for 0.5 and 2 hours at 850°C for the Si/Si_{1-y}C_y sandwich structure. Oxygen concentrations, which have decreased in both the Si_{1-y}C_y and surrounding silicon after 2 hours, are also shown.

existing models for boron segregation in single-crystal $\text{Si}_{1-x}\text{Ge}_x$ and discuss their potential relevance to our observations.

5.4 Potential mechanisms for boron segregation in $\text{Si}_{1-x-y}\text{Ge}_x\text{C}_y$ alloys

5.4.1 Boron segregation to single-crystal $\text{Si}_{1-x}\text{Ge}_x$

As mentioned earlier, it is well known that boron segregates to pseudomorphic single-crystal $\text{Si}_{1-x}\text{Ge}_x$ (no carbon) from unstrained silicon. Several published reports have found segregation coefficients ranging from 1.15 to 3.0 depending on germanium content and annealing conditions [3-6]. These reports are summarized in Figure 5.5, including the data from this work. Several mechanisms have been proposed to explain this effect. These are considered in sections 5.4.2 through 5.4.4, along with what effect carbon is expected to have on them.

5.4.2 Strain energy

Pseudomorphic $\text{Si}_{1-x}\text{Ge}_x$ films undergo macroscopic compressive strain when grown on silicon, due to the increased lattice constant from the larger germanium atoms. This increases the total energy of the $\text{Si}_{1-x}\text{Ge}_x$ film. Boron atoms can relieve some of this strain because they, being smaller than silicon, will tend to shrink the lattice constant. As a result, a $\text{Si}/\text{Si}_{1-x}\text{Ge}_x$ system can reduce its total strain energy if more boron atoms are in the $\text{Si}_{1-x}\text{Ge}_x$ layer vs. the Si. This represents an energetic driving force for the

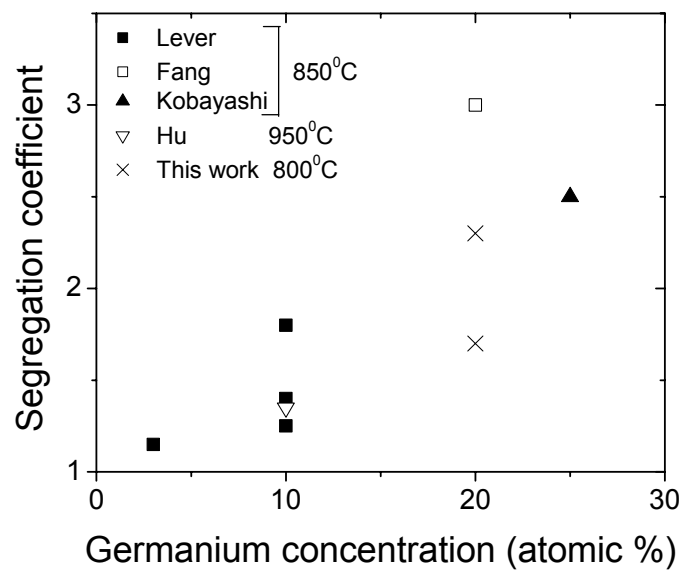


Figure 5.5. Summary of previous reports of boron segregation coefficients to strained pseudomorphic single-crystal $\text{Si}_{1-x}\text{Ge}_x$ from silicon (100) for low germanium percentages (<30%). From references [3-6].

segregation, and has been theoretically analyzed by Hu [7].

However, unlike germanium, carbon is smaller than silicon and produces the opposite strain - $\text{Si}_{1-x-y}\text{Ge}_x\text{C}_y$ films have less compressive strain than $\text{Si}_{1-x}\text{Ge}_x$ films, and $\text{Si}_{1-y}\text{C}_y$ films undergo tensile strain when grown on Si [8]. Based on strain energy arguments, one would expect to see less boron segregation to $\text{Si}_{1-x-y}\text{Ge}_x\text{C}_y$ films than to $\text{Si}_{1-x}\text{Ge}_x$. In addition, boron would tend to favor Si over tensile $\text{Si}_{1-y}\text{C}_y$. These are both opposite of what is observed. As a result, we conclude that strain energy is not the driving force for boron segregation to carbon-containing layers.

5.4.3 Bandgap effects

Pseudomorphic strained $\text{Si}_{1-x}\text{Ge}_x$ layers on Si (100) also have a reduced bandgap compared to silicon. Most of this bandgap difference appears in the valence band, resulting in ~ 7 meV/at.% Ge valence band offset [9,10]. As a result, the hole energy is reduced in strained $\text{Si}_{1-x}\text{Ge}_x$ films by this same amount. A boron atom, with its accompanying hole, will also have a lower energy in $\text{Si}_{1-x}\text{Ge}_x$ vs. Si due to this electronic energy difference.

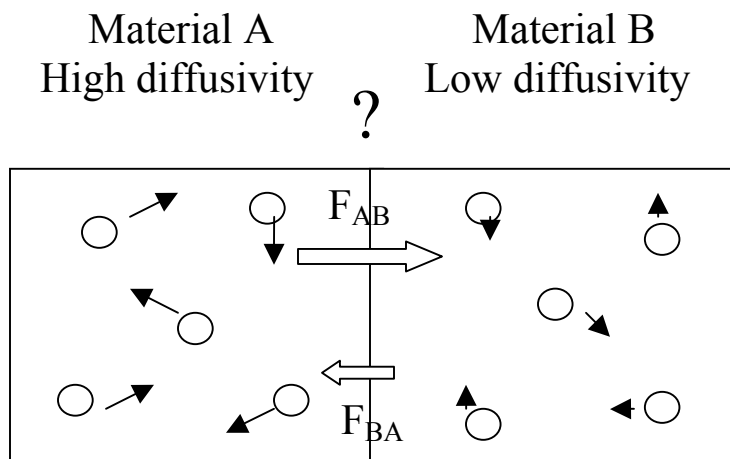
However, when substitutional carbon is added to $\text{Si}_{1-x}\text{Ge}_x$, the carbon is known to lead to a larger bandgap and a smaller valence band offset [11,12]. This would again predict less boron segregation to $\text{Si}_{1-x-y}\text{Ge}_x\text{C}_y$ compared to $\text{Si}_{1-x}\text{Ge}_x$, not more. Therefore, we conclude that carbon-induced bandgap effects are also not responsible for the segregation.

5.4.4 Direct Ge-B interactions

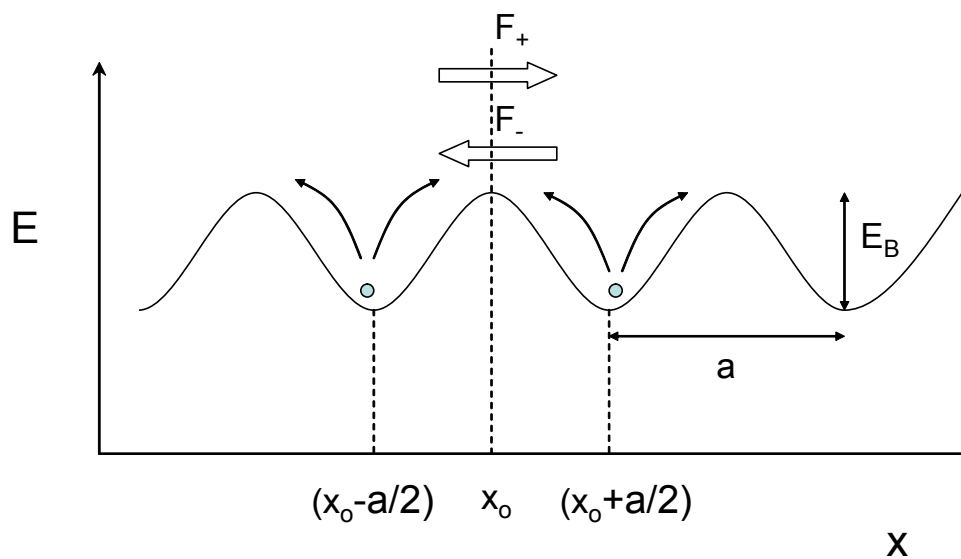
It has been proposed that a direct Ge-B interaction is responsible for boron segregation to $\text{Si}_{1-x}\text{Ge}_x$ [6]. However, the observation of segregation to both polycrystalline and single-crystal $\text{Si}_{1-y}\text{C}_y$ layers indicates that carbon itself can drive the segregation, without any Ge-B effects.

5.4.5 Effect of lower boron diffusivity

It may seem possible that simply a low diffusivity in a material causes segregation into it from a material with high diffusivity. This idea is illustrated in Figure 5.6(a). A material with a large diffusivity (A) is pictured adjacent to a material with a small diffusivity (B). The materials are assumed to be at the same temperature, and initially have the same concentration of atoms. Due to random thermal motion, the atoms in both materials will be hopping around in random directions. However, in the material with high diffusivity, they will be hopping faster than in the material with low diffusivity. A certain fraction of the boron atoms in both materials will be close to the interface, and be hopping in the direction of the interface (shown as flux arrows in the illustration). Since the atoms in material A are hopping faster than the atoms in material B, it appears that the flux across the interface from A to B (F_{AB}) will be bigger than in reverse (F_{BA}) (assuming the concentration is initially uniform). As a result, it appears there may be a net motion of boron from material A to material B, causing segregation into material B.



(a)



(b)

Figure 5.6. (a) Illustration of the appearance of segregation between two materials with different diffusivities. (b) Potential energy vs. position plot for diffusing atoms in a lattice.

Upon closer inspection, however, it can be shown that differences in diffusivity are not fundamentally the cause of segregation. A helpful way to view this is through diffusion potential diagrams, as shown in Figure 5.6(b). The (one-dimensional) potential energy of a boron atom in a lattice is plotted vs. position. The valleys represent lattice sites, which are energetically favorable for boron atoms to sit on, and the peaks the regions in between lattice sites which are a higher-energy position. In this simple model, to randomly hop from one site to another an atom must have enough energy to overcome the barrier between sites. At a given temperature, the frequency ν that an atom makes a successful hop over the barrier is inversely dependent on the size of the barrier, and given by [13]:

$$\nu = \nu_o e^{-\frac{E_B}{kT}} \quad (5.1)$$

where E_B is the barrier height, k is Boltzmann's constant, T is the temperature, and ν_o is a constant for a given temperature. Since diffusion requires this random hopping, the diffusivity will also be inversely dependent on the barrier height:

$$D = \frac{a^2 \nu_o}{2} e^{-\frac{E_B}{kT}} \quad (5.2)$$

where a is the lattice constant.

If one looks at a plane at position x_0 in the Figure 5.6(b), the flux coming from the left is proportional to the concentration of atoms there times the frequency of hopping from the left:

$$F_+ = \frac{a\nu_o}{2} C \left(x_0 - \frac{a}{2} \right) e^{\frac{-E_B}{kT}} \quad (5.3)$$

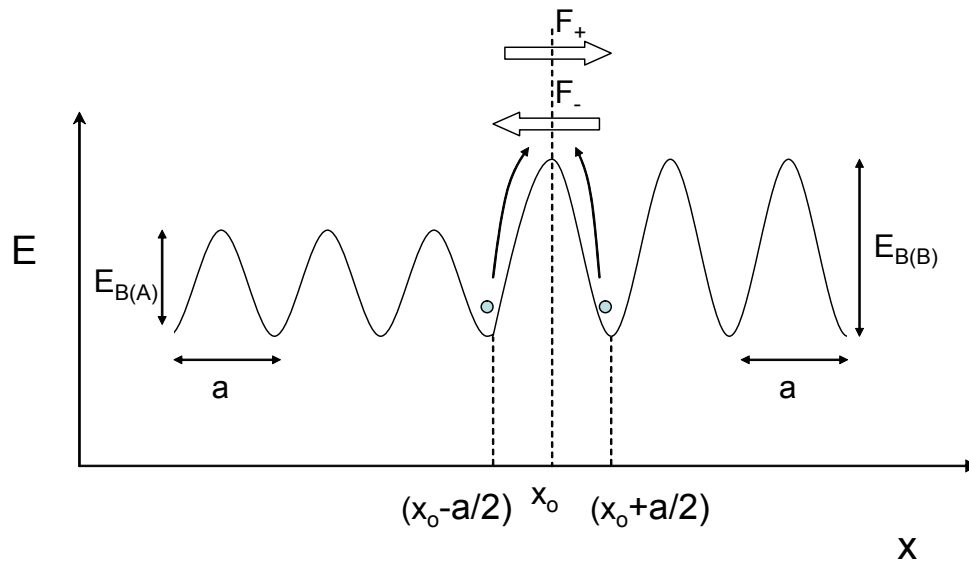
Similarly, for atoms hopping from the right:

$$F_- = \frac{a\nu_o}{2} C \left(x_0 + \frac{a}{2} \right) e^{\frac{-E_B}{kT}} \quad (5.4)$$

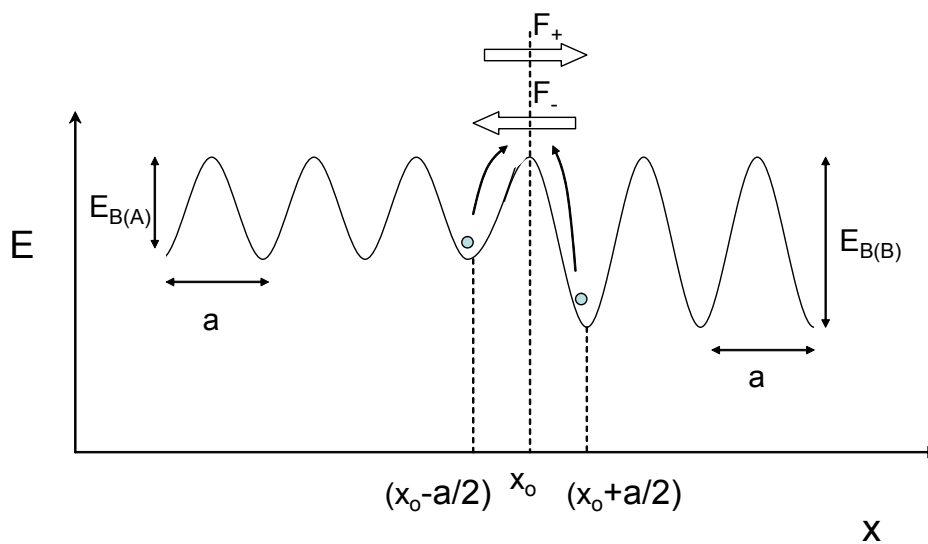
In this case, the energy barrier as seen from both sides is the same. As a result, in equilibrium ($F_+=F_-$) the concentration must be uniform, $C(x_0-a/2)=C(x_0+a/2)$.

If two materials with different diffusivities share an interface, the height of the potential barrier will change across that interface. Figure 5.7 shows two ways that this can happen. In both cases, the potential barriers in material A (high diffusivity) are lower than in material B (low diffusivity). In case (a), the valleys energies stay constant, while the peak energies change. If one considers a plane near the interface, e.g. at $x=x_0$ in the figure, the potential barriers as seen from either side are still the same. As a result, similar to the previous case, in equilibrium ($F_+=F_-$) the concentration must be uniform, $C(x_0-a/2)=C(x_0+a/2)$. There will be no segregation between the two materials, despite the difference in diffusivity.

In case (b), the valley energies change while the peak energies stay constant.



(a)



(b)

Figure 5.7. Diffusion potential energy vs. position plots for two materials with different diffusivities, where (a) the valley energy stays constant and (b) the peak energy stays constant.

Again considering a plane at the interface at $x=x_0$, the potential barrier is now different as seen from the two sides. An atom hopping from the right sees a barrier $E_{B(B)}$ while an atom hopping from the left sees a barrier $E_{B(A)}$. As a result, in equilibrium ($F_+=F_-$), the concentration on the right must be higher than the concentration on the left by the amount:

$$\frac{C\left(x_0 + \frac{a}{2}\right)}{C\left(x_0 - \frac{a}{2}\right)} = e^{\frac{E_{B(B)} - E_{B(A)}}{kT}} \quad (5.5)$$

In this case, there is segregation into the material with lower diffusivity. The difference between the two cases is the change in valley energy for case (b), which is needed for segregation to occur.

The main point of this discussion is that *a smaller diffusivity in a material does not necessarily mean there will be segregation into it*. There may be, as in Figure 5.7(b), but there also may not be, as in Figure 5.7(a). More information besides just the diffusivity is needed. As a result, in our case for segregation from silicon to $\text{Si}_{1-x-y}\text{Ge}_x\text{C}_y$, it cannot be assumed that there will be segregation just because of the lower boron diffusivity in $\text{Si}_{1-x-y}\text{Ge}_x\text{C}_y$. Ultimately, differences in chemical potential are what drive the transport of atoms. In true equilibrium, segregation will occur only when there is a lower energy for an atom in one material vs. another, not a difference in diffusion coefficient. As outlined in the previous few subsections, we do not think there is any reason to expect a decrease in energy for boron between silicon and $\text{Si}_{1-y}\text{C}_y$ (or $\text{Si}_{1-x-y}\text{Ge}_x\text{C}_y$ vs. $\text{Si}_{1-x}\text{Ge}_x$).

In Chapter 6, we will examine segregation of boron in a case which is not at equilibrium. We will see that a gradient of substitutional carbon atoms causes a gradient of silicon interstitial atoms, which in turn drives the net motion of boron atoms preferentially in one direction. This causes a buildup of boron in the regions of high substitutional carbon. This is not a true equilibrium segregation, however, because the carbon atoms are mobile (enabled in large part by the silicon interstitial atoms), and in equilibrium will move to being uniform in space. As a result, the silicon interstitial gradient, and hence boron pile-up, also goes away.

5.4.6 Boron trapping at carbon-related defects

A final possibility considered here is that boron atoms are becoming trapped at carbon-related defects. Many of the carbon concentrations and anneal conditions used in our experiments are known to lead to silicon carbide (SiC) precipitation in the films [14,15]. It is possible that boron atoms are getting trapped either in or at the surfaces of these defects. Another possibility is a direct boron-carbon cluster, like the immobile boron-carbon-interstitial cluster proposed by Liu et al [16].

One would expect to see two consequences from the formation of defects: (i) a loss of electrically active boron in the films upon annealing, since boron atoms are coming out of substitutional lattice sites and into (presumably inactive) defects, and (ii) immobilized boron that cannot diffuse anymore. Possibility (i) is examined and ruled out in section 5.5, and (ii) in section 5.6.

5.5 Electrical properties of single-crystal boron-doped $\text{Si}_{1-x-y}\text{Ge}_x\text{C}_y$ and $\text{Si}_{1-y}\text{C}_y$

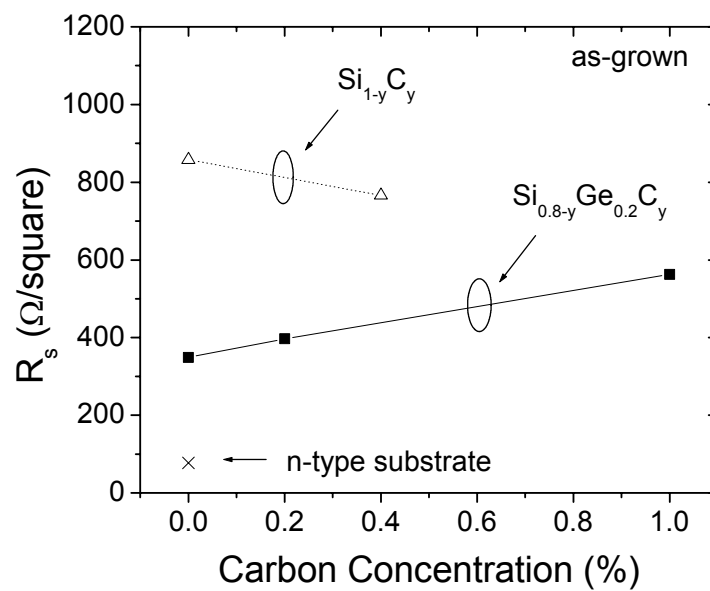
In Chapter 4 the electrical properties of polycrystalline $\text{Si}_{1-x-y}\text{Ge}_x\text{C}_y$ films were discussed. For samples with low carbon content (0.4%), no deactivation of boron was observed during thermal anneals at 900°C for up to five hours. However, large amounts of segregation were observed for these same anneal conditions, indicating that electrically inactive defects are not driving the segregation. Here, similar experiments were performed on single-crystal material.

On top of an n-type substrate and buffer, 50 nm layers of either p^+ Si, $\text{Si}_{0.8}\text{Ge}_{0.2}$, $\text{Si}_{0.8-y}\text{Ge}_{0.2}\text{C}_y$, or $\text{Si}_{1-y}\text{C}_y$ were grown, and capped with 5 nm of undoped silicon (Figure 5.8(a)). For the $\text{Si}_{1-x-y}\text{Ge}_x\text{C}_y$ samples, which were grown using dichlorosilane as a silicon source (recipe $\text{Si}_{1-x-y}\text{Ge}_x\text{C}_y:1$ from Appendix A), the boron-doping levels in our system are well characterized (using SIMS measurements) and were set to $3 \times 10^{19} \text{ cm}^{-3}$. The $\text{Si}_{1-y}\text{C}_y$ samples were grown using disilane (recipe $\text{Si}_{1-y}\text{C}_y:1$ from Appendix A). Because of the different growth conditions, the doping levels were somewhat lower. As a result, a separate silicon control was grown with disilane (recipe Si:3) for direct comparison to the $\text{Si}_{1-y}\text{C}_y$ sample.

Figure 5.8(b) shows as-grown sheet resistance as a function of carbon concentration. The values are consistent with what would be expected for 50-nm layers doped at $3 \times 10^{19} \text{ cm}^{-3}$. In addition, an n-type substrate (identical to those used for growing the doped $\text{Si}_{1-x-y}\text{Ge}_x\text{C}_y$ layers) was measured and had a sheet resistance almost an order of magnitude lower than the other samples. This indicates that the p^+ -n junction

Si cap	5 nm
p ⁺ Si _{1-x-y} Ge _x C _y	50 nm
Si buffer	50 nm
n-type substrate	

(a)



(b)

Figure 5.8. (a) Structure and (b) sheet resistance of as-grown 50 nm single-crystal $\text{Si}_{0.8-y}\text{Ge}_{0.2}\text{C}_y$ and $\text{Si}_{1-y}\text{C}_y$ samples doped with boron at $3 \times 10^{19} \text{ cm}^{-3}$.

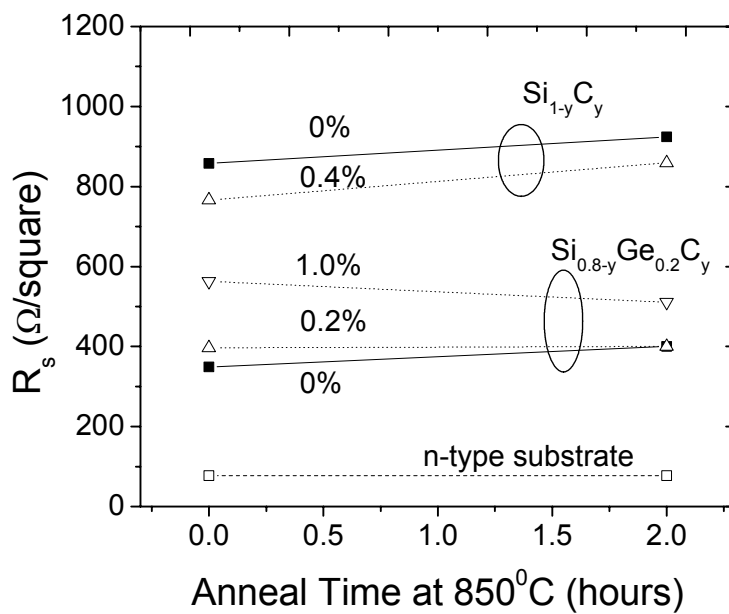


Figure 5.9. Sheet resistance vs. anneal time at 850°C for single-crystal $Si_{0.8-y}Ge_{0.2}C_y$ and $Si_{1-y}C_y$ samples.

between the boron-doped regions and the substrate is effectively isolating the $\text{Si}_{1-x-y}\text{Ge}_x\text{C}_y$ layers (electrically). For the $\text{Si}_{1-x-y}\text{Ge}_x\text{C}_y$ layers, the sheet resistance goes up with carbon concentration. This is consistent with previous reports as mentioned in Chapter 4, and may be due to a drop in mobility from carbon-induced scattering. The sheet resistance of the $\text{Si}_{0.996}\text{C}_{0.004}$ layer, however, is actually less than its silicon control. This may be due to the effect of tensile strain (estimated to be $\sim 0.2\%$) from the carbon, or just sample-to-sample variation. As can be seen, the sheet resistances of the $\text{Si}_{1-y}\text{C}_y$ samples grown with disilane are higher than the $\text{Si}_{1-x-y}\text{Ge}_x\text{C}_y$ samples, indicating that the actual doping levels in these samples were lower, closer to $1.5 \times 10^{19} \text{ cm}^{-3}$.

Most significantly, within experimental error, the sheet resistances are stable when subjected to annealing. Figure 5.9 shows sheet resistance before and after an 850°C , 2-hour anneal. This annealing condition induced significant boron segregation to a 0.4% $\text{Si}_{1-y}\text{C}_y$ layer (Figure 5.4), and assuming an activation energy for boron diffusion of $\sim 3.5 \text{ eV}$, is comparable (based on diffusion lengths) to the 800°C , 18-hour anneals which caused segregation to $\text{Si}_{1-x-y}\text{Ge}_x\text{C}_y$ layers (Figure 5.2). If the segregation is being driven by boron moving to electrically inactive defect sites, large decreases in the hole concentration would be observed (if one makes the reasonable assumption that boron which segregates into a $\text{Si}_{1-x-y}\text{Ge}_x\text{C}_y$ or $\text{Si}_{1-y}\text{C}_y$ layer behaves the same as that which was put there *in-situ* and similarly annealed). However, as can be seen, no significant loss in conductivity is observed in any of the samples, indicating the boron remains electrically active and that its segregation is not driven by its trapping at electrically inactive defects. It is theoretically possible that carbon and boron could interact to yield energy savings when both are on lattice sites, so as to maintain the electrical activity of the boron.

However, this is unlikely since they are both small atoms [16], and although it cannot be ruled out entirely, we will assume this is not happening.

5.6 Reversibility of boron segregation

In this section the possibility of boron segregating to immobile defect sites is further considered. If boron is becoming trapped at immobile carbon-related defects, then once boron has segregated to a $\text{Si}_{1-y}\text{C}_y$ layer, it should not be able to diffuse out again (assuming the defects are stable). Therefore an experiment was performed to test the reversibility of the segregation process. The same structure shown in Figure 5.3 (to study segregation to $\text{Si}_{1-y}\text{C}_y$) was first annealed at 850°C for 2 hours in N_2 , the same as for Figure 5.4 to induce segregation in that sample. In this section the sample was also subjected to an additional 2-hour dry oxidation at 850°C . The purpose of the initial N_2 anneal was, as before, to allow the boron to segregate to the $\text{Si}_{1-y}\text{C}_y$ layer. The second step (oxidation) was designed to drive the substitutional carbon out of the $\text{Si}_{1-y}\text{C}_y$ layer.

When the silicon surface is oxidized, it is known that silicon self-interstitials are injected into the sample. These silicon interstitials diffuse down to the $\text{Si}_{1-y}\text{C}_y$ layer and interact with the substitutional carbon atoms through the following reaction:

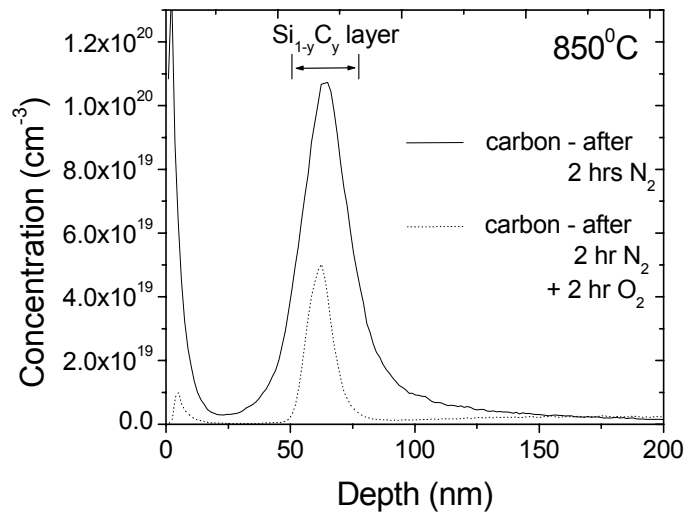


where C_S is a substitutional carbon atom, I is a silicon interstitial atom, and C_I is a carbon-silicon interstitial pair, or carbon “interstitialcy”. The resulting carbon

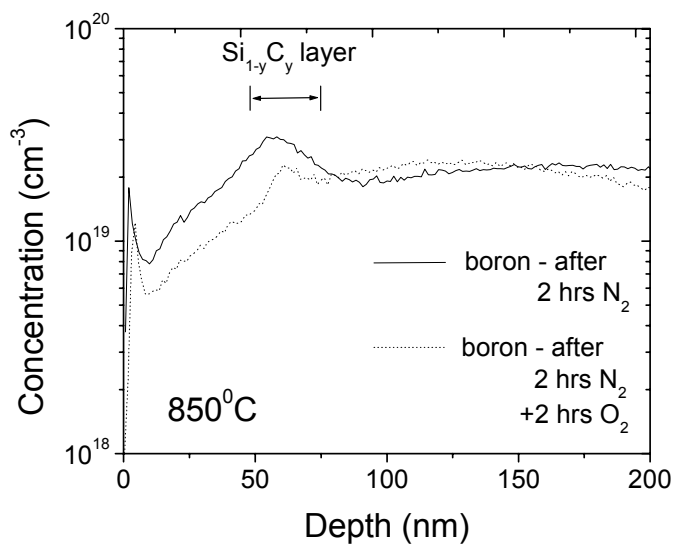
interstitialcies are very mobile and diffuse quickly compared to the substitutional carbon [17, 18]. Since the $\text{Si}_{1-y}\text{C}_y$ layer is positioned so close to the surface, they can rapidly diffuse to the surface and into the growing oxide. (SIMS profiles confirm that carbon is accumulating in the oxide.) It has been previously shown that by this mechanism almost all of the carbon can be removed from a $\text{Si}_{0.796}\text{Ge}_{0.2}\text{C}_{0.004}$ layer with the same thickness and oxidation conditions [2]. In addition, for the same rate of interstitial injection, the loss of carbon has been shown to be the same for $\text{Si}_{1-x-y}\text{Ge}_x\text{C}_y$ and $\text{Si}_{1-y}\text{C}_y$ layers [1].

In Figure 5.10, carbon and boron profiles in this sample, which was subjected to both the nitrogen anneal and oxidation, are compared to the sample from the section 5.3, which was subjected to only the N_2 anneal. It can be seen in Figure 5.10(a) that, as anticipated, most of the carbon is removed from the $\text{Si}_{1-y}\text{C}_y$ layer during the oxidation step. 84% of the integrated carbon has been removed from the region of the original $\text{Si}_{1-y}\text{C}_y$ layer, with 74% removed from the sample entirely. Figure 5.10(b) shows that, after oxidation, most of the boron segregation caused by the initial nitrogen anneal has gone away, with the profile largely flattening out. The decrease near the surface is caused by boron evaporation and/or segregation into the oxide layer on the surface.

The ability to reverse the segregation to the $\text{Si}_{1-y}\text{C}_y$ region in this structure via the oxidation step argues against the formation of immobile boron-carbon defects as the driving force for the segregation. In particular, it is unlikely that the segregation was caused by SiC precipitates, which were then caused to be removed by the oxidation. The presence of excess interstitials is known to drive the *formation* of SiC precipitates in silicon, not their removal [19]. (Note: A small residual boron peak does remain in the



(a)



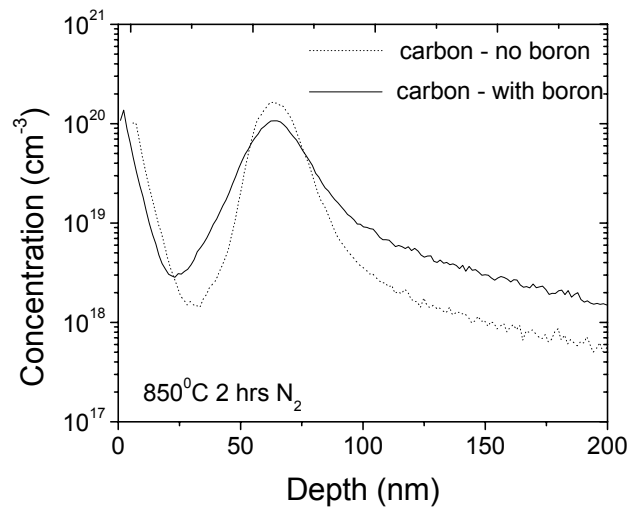
(b)

Figure 5.10. SIMS profiles of (a) carbon and (b) boron after a 2-hour nitrogen anneal at 850°C (solid lines), and after both a 2-hour nitrogen anneal and 2-hour oxidation at 850°C (dotted lines). Note the y-axis in (a) is on a linear scale.

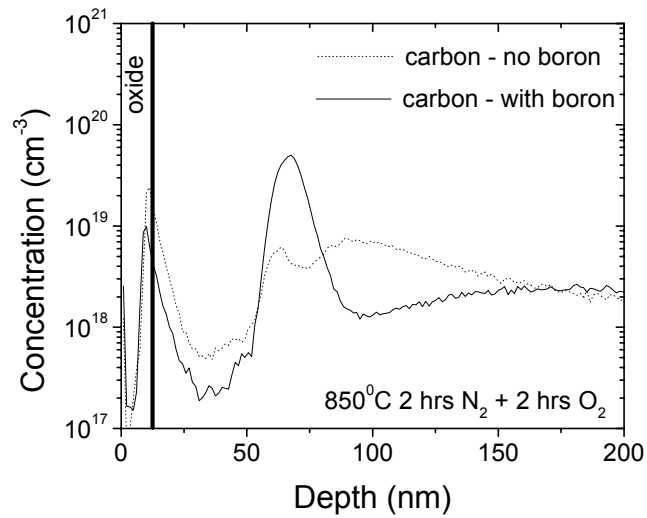
region of the original $\text{Si}_{1-y}\text{C}_y$ layer; whether this simply hasn't had enough time to diffuse away, or is potentially associated with a small number of defects, is not clear.)

5.7 Effect of boron on carbon diffusion

This chapter is concluded with a discussion of an effect that, while not directly related to boron segregation, will have an impact on the diffusion simulations performed in the next chapter. The diffusion of carbon out from the $\text{Si}_{1-y}\text{C}_y$ layer was studied, and found to be affected by the presence of boron. SIMS profiles of the carbon in the $\text{Si}/\text{Si}_{1-y}\text{C}_y$ structure from Figure 5.3 (with boron) were compared with those from a structure identical in every way, except there was no boron intentionally introduced anywhere in the sample. Figure 5.11(a) compares the carbon diffusion during just the 2-hour 850°C nitrogen anneal in the samples with and without boron (the carbon spikes near the surface in Fig. 5.11(a) are due to surface contamination during the SIMS measurement, and were not part of the sample structure). The carbon diffusion is significantly faster when boron is present. One possible explanation for this effect may be an increased level of silicon interstitials in the boron-doped sample. Heavily p^+ -doped silicon is known to have increased silicon interstitial concentrations due to Fermi level effects [20]. In our structure, boron levels are in the 10^{19} cm^{-3} range, much higher than the intrinsic carrier concentration at 850°C and sufficient to cause these effects. For example, boron diffusion, which depends on a mechanism similar to that of Equation 5.6, is increased by $\sim 10\text{X}$ at a doping level of $3 \times 10^{19} \text{ cm}^{-3}$, over that at much lower doping levels [20]. Since carbon diffusion is also enhanced by silicon interstitials, the increased



(a)



(b)

Figure 5.11. Carbon profiles in structure with boron compared to structure without boron, after (a) just the N_2 anneal, and (b) both N_2 anneal and oxidation. The concentrations in the oxide are not calibrated.

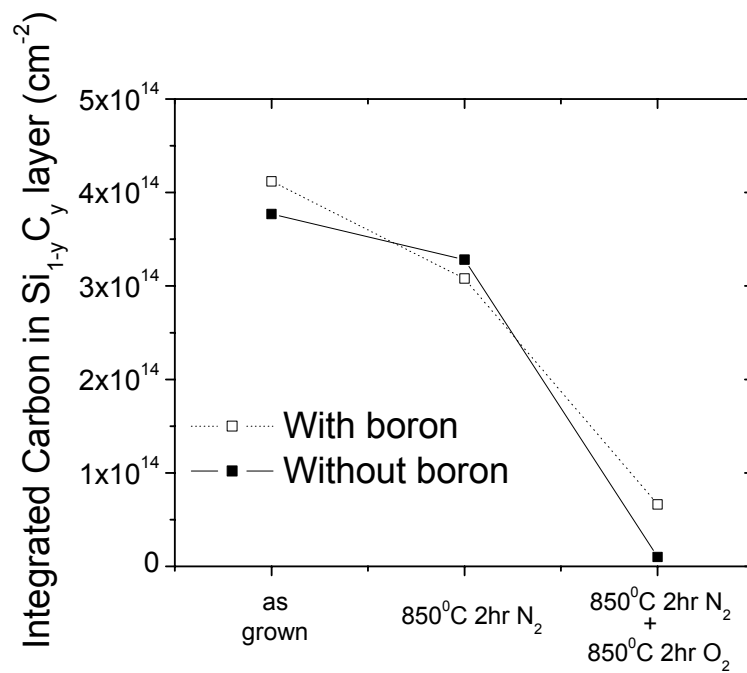


Figure 5.12. Integrated carbon (in the region initially containing the $\text{Si}_{1-y}\text{C}_y$ layer) vs. anneal time for structures with or without boron.

interstitial levels may be causing the broader carbon profile.

SIMS profiles after both the N₂ anneal and oxidation step (Figure 5.11(b)), however, show an apparent contradiction - more carbon remains in the sample with boron after oxidation, even though the carbon was diffusing away faster during the nitrogen anneal. This is represented quantitatively in Figure 5.12. The integrated carbon in the Si_{1-y}C_y layer drops faster for the boron-doped sample (due to enhanced diffusion) during the nitrogen anneal, but sees a smaller drop during the subsequent oxidation. The remaining carbon peak in Figure 5.11(b) appears immobile and may be in the form of silicon carbide (SiC) precipitates. It has been reported that carbon precipitation is enhanced by silicon interstitials [19,21]. This raises the possibility that, if boron is in fact enhancing interstitial concentrations during the N₂ anneal as suggested above, it may also be enhancing carbon precipitation by this same mechanism. Further investigation (e.g. transmission electron microscopy (TEM)) is needed to directly check for silicon carbide precipitation to support this hypothesis.

5.8 Summary

It has been shown that boron segregates into single-crystal Si_{1-x-y}Ge_xC_y and Si_{1-y}C_y alloys from silicon, similar to the polycrystalline case. Driving forces that have previously been proposed to explain boron segregation to Si_{1-x}Ge_x (without carbon), including strain and bandgap differences, do not favor enhanced segregation when carbon is added. The ability to reverse most of the segregation, by removing the carbon from the layer, argues against immobile carbon-related defects as a driving force for the

segregation. Having ruled out these possibilities, the next chapter is devoted to showing how gradients of silicon interstitials, created by high levels of substitutional carbon, can drive boron segregation to $\text{Si}_{1-x-y}\text{Ge}_x\text{C}_y$ layers.

5.9 References

- [1] M.S. Carroll and J.C. Sturm, *Applied Physics Letters*, vol. 81(7), p. 1225-1227 (2002).
- [2] M.S. Carroll, J.C. Sturm, E. Napolitani, D. De Salvador, M. Berti, J. Stangl, G. Bauer, and D.J. Tweet, *Physical Review B*, vol. 64, 073308 (2001).
- [3] T.T. Fang, W.T.C. Fang, P. B. Griffin, and J. D. Plummer, *Applied Physics Letters*, vol. 68(6), p. 791-793 (1996).
- [4] S. Kobayashi, T. Aoki, N. Mikoshiba, M. Sakuraba, T. Matsuura, and J. Murota, *Thin Solid Films*, vol. 369, p. 222-225 (2000).
- [5] S.M. Hu, D.C Ahlgren, P.A. Ronsheim, and J.O. Chu, *Physical Review Letters* **67**, 1450 (1991).
- [6] R.F. Lever, J.M. Bonar, and A.F.W. Willoughby, *Journal of Applied Physics*, vol. 83(4), p. 1988-1994 (1998).
- [7] S.M. Hu, *Physical Review B*, vol. 45 (8), p. 4498-4501 (1992).
- [8] D. De Salvador, M. Petrovich, M. Berti, F. Romanato, E. Napolitani, A. Drigo, J. Stangl, S. Zerlauth, M. Muhlberger, F. Schaffler, G. Bauer, and P.C. Kelires, *Physical Review B*, vol. 61(19), p. 13005-13013 (2000).
- [9] D.V. Lang, R. People, J.C. Bean, and A.M. Sergent, *Applied Physics Letters*, vol. 47(12), p. 1333-1335 (1985).
- [10] D.C. Houghton, G.C. Aers, S.-R. Eric Yang, E. Wang, and N.L. Rowell, *Physical Review Letters*, vol. 75(5), p. 866-869 (1995).
- [11] A. St. Amour, C.W. Liu, J.C. Sturm, Y. Lacroix, and M.L.W. Thewalt, *Applied Physics Letters*, vol. 67(26), p. 3915-3917 (1995).
- [12] C.L. Chang, L.P. Rokhinson, and J.C. Sturm, *Applied Physics Letters*, vol. 73(24), p. 3568-3570 (1998).
- [13] J.R. Manning, Diffusion Kinetics of Atoms in Crystals, Princeton: D. Van Nostrand Company, p. 10-16 (1968).
- [14] L.V. Kulik, D.A. Hits, M.W. Dashiell, and J. Kolodzey, *Applied Physics Letters*, vol. 72(16), p. 1972-1974 (1998).
- [15] P. Warren, J. Mi, F. Overney, and M. Dutoit, *Journal of Crystal Growth*, vol. 157, p. 414-419 (1995).
- [16] C.-L. Liu, W. Windl, L. Borucki, S. Lu, and X.Y. Liu, *Applied Physics Letters*, vol. 80(1), p. 52-54 (2002).
- [17] G. Davies and R.C. Newmann, "Carbon in Monocrystalline Silicon", in *Handbook on Semiconductors*, T.S. Moss, Ed., 1994, p. 1558.
- [18] R. Scholz, U. Gosele, J.-H. Huh, and T.Y. Tan, *Applied Physics Letters*, vol. 72(2), p. 200-202 (1998).
- [19] W.J. Taylor, T.Y. Tan, and U. Gosele, *Applied Physics Letters*, vol. 62(25), p. 3336-3338 (1993).
- [20] Fair, R.B., *Impurity Doping Processes in Silicon*, ed. F.F.Y. Wang, Amsterdam: North Holland (1981).
- [21] E. Napolitani, D. De Salvador, A. Coati, M. Berti, A.V. Drigo, M.S. Carroll, J.C. Sturm, J. Stangl, G. Bauer, and C. Spinella, *Nuclear Instruments and Methods in Physics Research B*, vol. 186, p. 212-217 (2002).

Chapter 6: Interstitial-gradient driven segregation to $\text{Si}_{1-x-y}\text{Ge}_x\text{C}_y$ and $\text{Si}_{1-y}\text{C}_y$ alloys

6.1 Introduction

In the previous chapter it was shown that boron segregates to single-crystal $\text{Si}_{1-x-y}\text{Ge}_x\text{C}_y$ and $\text{Si}_{1-y}\text{C}_y$, and that the mechanisms known to drive segregation to $\text{Si}_{1-x}\text{Ge}_x$, as well as carbon-related defects, are not likely driving forces. In this chapter, a new mechanism for driving boron segregation is presented, that of gradients of silicon interstitials. This is significant for technological applications, as it shows that boron can accumulate in carbon regions without forming undesirable defects. In addition, these considerations are ultimately not limited to boron, but will have implications for any dopant that diffuses by a similar mechanism, and may be helpful for understanding dopant redistribution in a variety of situations.

To understand what silicon interstitial gradients are and how they are formed, carbon diffusion in silicon is first reviewed. This is followed by a presentation of a model for simulating carbon and silicon interstitial diffusion, which quantitatively establishes the magnitude of silicon interstitial gradients as they are consumed by substitutional carbon. Then boron diffusion is considered, including how it is affected by silicon interstitials and their gradients. The physics of how these gradients can drive boron segregation is introduced. Finally, boron segregation is formally modeled and compared to experimental data.

6.2. Carbon diffusion in crystalline silicon

6.2.1 Diffusion by interstitial mechanism

To understand diffusion in single-crystal Si and $\text{Si}_{1-x}\text{Ge}_x$ lattices, it is important to consider the atomic mechanisms that drive it. Carbon (at low concentrations) and boron are both substitutional impurities in silicon - that is, they sit on substitutional lattice sites in place of a silicon atom. In order to diffuse, they must be able to randomly hop from one lattice site to another. Ordinarily this is a difficult process - substitutional carbon (or boron) atoms have a small likelihood of hopping directly to an adjacent lattice site by themselves. As a result, the diffusivity of a substitutional carbon atom is very low.

However, their mobility can be enhanced by the presence of silicon self-interstitials. A silicon self-interstitial is a silicon atom that is not on a lattice site, but instead in the interstitial space between lattice sites (Figure 6.1). Silicon self-interstitials can be thermally generated from silicon atoms jumping off lattice sites (and creating an accompanying "vacancy"), or injected from surfaces. At a given temperature, there is always some equilibrium number of silicon interstitials in the lattice; however, this concentration is very low and difficult to detect. For the temperatures used in this work (800-900°C), most reports put the concentration in the 10^{10} - 10^{12} cm^{-3} range [1].

Despite the small concentrations of silicon interstitials, they play an important role in carbon and boron diffusion. When an interstitial approaches a substitutional carbon atom, it can kick it off of its site and form a new configuration, where the lattice site is

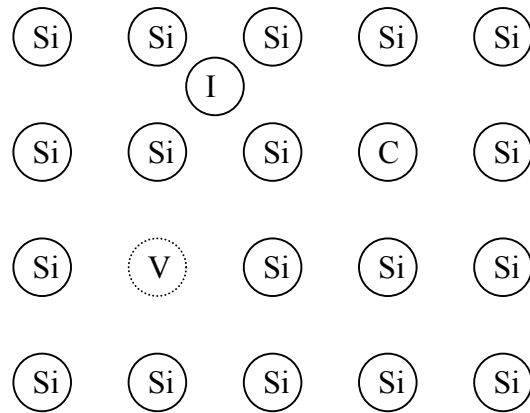


Figure 6.1: Illustration of a substitutional carbon, interstitial silicon, and vacancy in a silicon lattice.

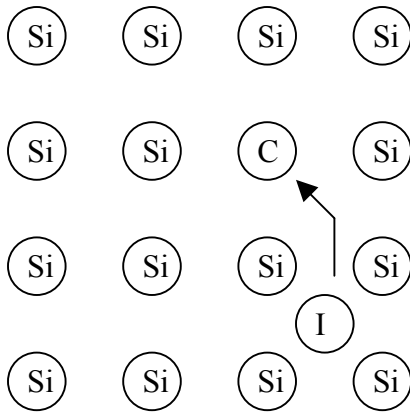
shared by the boron and silicon atom. This configuration is called a carbon interstitial or "interstitialcy" [2], and is described by the reaction:



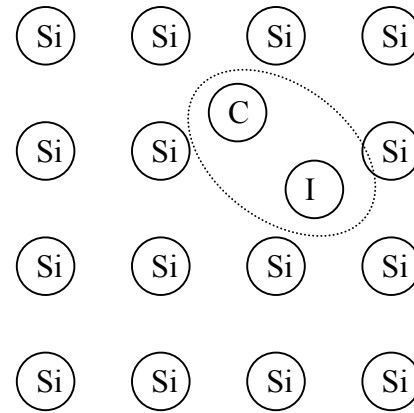
where C_S is a substitutional carbon atom, I is a silicon interstitial atom, and C_I is a carbon-silicon interstitial pair, or "interstitialcy". The carbon-interstitial pair is very mobile, and can rapidly diffuse through the lattice [2,3]. Typically this is done by the carbon atom displacing the silicon atom in the adjacent site to form a new interstitialcy pair there. The previously paired silicon atom can then return to the empty substitutional site. As a result, the interstitialcy configuration has moved to the adjacent lattice site. Eventually, the pair will dissociate, with the carbon atom returning to a substitutional site and the silicon interstitial diffusing away. To review this mechanism:

- (i) A silicon self-interstitial approaches an initially immobile substitutional carbon atom;
- (ii) "Kick-out" reaction occurs, and carbon and silicon interstitial share lattice site (C_I);
- (iii) The newly mobile C_I can diffuse through the silicon lattice;
- (iv) The pair dissociates, with carbon returning to an immobile substitutional site and the interstitial diffusing away.

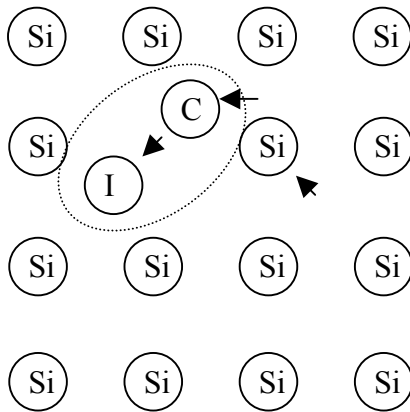
This is shown schematically in Figure 6.2. Note this process is often simplified in explanations - the "interstitialcy" is replaced by an interstitial carbon atom, which is mobile, and substitutional silicon atom.



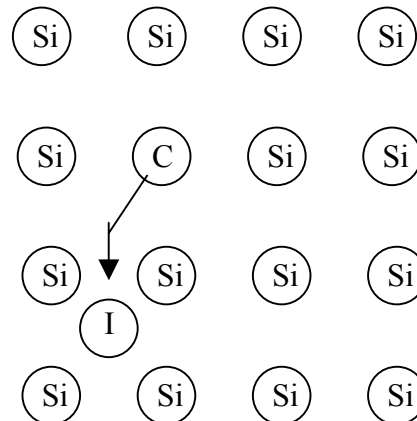
(i) Silicon interstitial (I) approaches substitutional carbon atom (C).



(ii) Carbon and interstitial react to form carbon interstitialcy.



(iii) Carbon diffuses by establishing new interstitialcy on adjacent lattice site.



(iv) Carbon interstitialcy dissociates, carbon returns to substitutional site.

Figure 6.2: Illustration of carbon diffusion by silicon interstitial-assisted mechanism. Boron diffuses in a similar way.

As substitutional carbon needs silicon interstitials to become mobile, its diffusivity depends heavily on the amount of interstitials in the lattice. If the interstitial population is low, diffusion will be slow; if the interstitial population is high, diffusion will be fast. This property was exploited in Chapter 5 to rapidly remove the carbon from a $\text{Si}_{1-y}\text{C}_y$ layer positioned close to a silicon surface. By oxidizing the silicon surface, large numbers of silicon interstitials were injected into the sample, enhancing the interstitial population and hence the carbon diffusion. The now mobile carbon, being so close to the surface, was then able to mostly diffuse out of the sample.

6.2.2 Substitutional carbon as a silicon interstitial sink

As silicon interstitials influence carbon diffusion, carbon also influences the evolution of interstitial profiles. When a carbon interstitialcy (C_I) forms, a silicon interstitial is consumed (it becomes part of the interstitialcy). At low carbon concentrations, this reaction does not significantly affect the interstitial populations. However, for high carbon concentrations, such as those used in this work, the forward of Equation 6.1 consumes so many silicon interstitials that the region quickly becomes depleted of them [3]. The carbon interstitialcies, once formed, can diffuse out of the layer and into the surrounding silicon. Here the population of substitutional carbon is low, and they will quickly dissociate (the reverse of Equation 6.1) into substitutional carbon and silicon interstitials, raising the population of interstitials in these adjacent regions. In this manner, silicon interstitials are consumed in a $\text{Si}_{1-x-y}\text{Ge}_x\text{C}_y$ layer,

transported out in the form of a carbon-interstitial pair, and released into the adjacent regions. A large deficit of silicon interstitials appears in the regions with a high concentration of substitutional carbon, and will be maintained as long as large numbers of carbon are reacting and diffusing out of the layer.

This deficit of silicon interstitials in the high carbon-region (with corresponding equilibrium concentrations in the region surrounding it some distance away) will in turn affect the carbon diffusion itself. The carbon atoms that did not initially pair with interstitials, and are left behind in the peak, find themselves in a region of reduced interstitial concentration, and diffuse very slowly. The carbon atoms that did diffuse away initially, and have moved into the tail of the profile, find themselves a region with higher interstitial concentration and diffuse readily. The peak becomes stationary while the tails continue to spread. This is in fact what is observed in experimental carbon profiles: large immobile peaks at the center of the profiles, with broad tails.

6.3 Modeling of the coupled diffusion of carbon and silicon interstitials

Previously, a complete model of coupled carbon and silicon interstitial diffusion was developed to model this process [4] using the PROPHET simulator [5], the main components of which are summarized here. Substitutional carbon is assumed to undergo 2 reactions: Equation 6.1 (kick-out) and:



where V is a vacancy. Often referred to as the Frank-Turnbull reaction [6], this describes substitutional carbon directly forming an interstitialcy on a neighboring site and leaving a vacancy behind. This equation is important in correctly modeling the carbon diffusion, and will affect the vacancy concentrations. However, as we are more interested in the silicon interstitial profiles, this process will not be discussed in detail here.

The kinetics of the above two reactions are represented by the reaction rates:

$$R_{C_sI} = K_{fI} C_s I - K_{rI} C_I \quad (6.3)$$

$$R_{C_I V} = K_{fV} C_I V - K_{rV} C_s \quad (6.4)$$

where R_{C_sI} is the reaction rate of substitutional carbon and silicon interstitials to form carbon interstitialcies, $R_{C_I V}$ is the reaction rate of carbon interstitialcies and vacancies to form substitutional carbon, K_{fI} and K_{rI} are the forward and reverse reaction constants, respectively, for Equation 6.1, and K_{fV} and K_{rV} are the forward and reverse reaction constants, respectively, for Equation 6.2.

The simultaneous reaction and diffusion of the four relevant species C_s , C_I , I , and V are then represented by four equations:

$$\frac{\partial C_s}{\partial t} = -R_{C_sI} + R_{C_I V} \quad (6.5)$$

$$\frac{\partial C_I}{\partial t} = D_{C_I} \nabla^2 C_I + R_{C_sI} - R_{C_I V} \quad (6.6)$$

$$\frac{\partial I}{\partial t} = D_I \nabla^2 I - R_{C_sI} \quad (6.7)$$

$$\frac{\partial V}{\partial t} = D_V \nabla^2 V - R_{C_i V} \quad (6.8)$$

where D_{C_i} , D_I , and D_V are the diffusivities of carbon interstitialcies, silicon interstitials, and vacancies, respectively. The diffusion of substitutional carbon is considered to be negligible, so that all of the carbon diffusion is due to the motion of carbon interstitialcies. Values for the rate constants and diffusivities were taken from [1], [2], [4], [7] and are summarized in Table 6.1.

Previously, this model was successfully used to simulate the diffusion of carbon in $\text{Si}_{1-y}\text{C}_y$ and $\text{Si}_{1-x-y}\text{Ge}_x\text{C}_y$ under a variety of conditions [4]. We find that it also can accurately model carbon diffusion (no boron present yet) in our samples. Figure 6.3 shows the SIMS profile of carbon in a structure identical to the $\text{Si}/\text{Si}_{1-y}\text{C}_y$ structure from Chapter 5 (Figure 5.3), except that no boron was present anywhere in the sample. This sample was annealed at 850°C for 2 hours in N_2 , and the resulting data compared with simulations. The profiles match very well; in particular, the pronounced diffusion in the tails of the profile, compared to the very slow diffusion in the peak, is modeled very accurately. The good match with data gives us confidence that the simulation accurately predicts the concentration profile of silicon interstitials in the regions where the carbon is out-diffusing. As can be seen, the region of high carbon concentration is severely depleted of silicon interstitials, by at least two orders of magnitude compared to the equilibrium value ($1.5 \times 10^{10} \text{ cm}^{-3}$ at 850°C). The surrounding regions actually have a slightly enhanced concentration, due to interstitials being released by the reverse of Equation 6.1 in this region.

Variable	Value
K_{fi}	$3.5e-5 \exp(-1.77/kt)$ [cm ³ /sec]
K_{ri}	$4.7e19 \exp(-2.78/kT)$ [1/sec]
K_{fv}	$3.02e-7 \exp(-0.87/kT)$ [cm ³ /sec]
K_{rv}	$1.67e19 \exp(-5.38/kT)$ [1/sec]
D_i	$51 \exp(-1.77/kT)$ [cm ² /sec]
D_v	$0.03 \exp(-1.8/kT)$ [cm ² /sec]
D_{Ci}	$0.44 \exp(-0.87/kT)$ [cm ² /sec]
I^*	$2.9e24 \exp(-3.18/kT)$ [cm ⁻³]
V^*	$1.71e24 \exp(-2.0/kT)$ [cm ⁻³]

Table 6.1: Variable coefficients used for coupled carbon-silicon interstitial diffusion simulations. I^* and V^* are the equilibrium values (used for surfaces and initial conditions) for interstitials and vacancies, respectively.

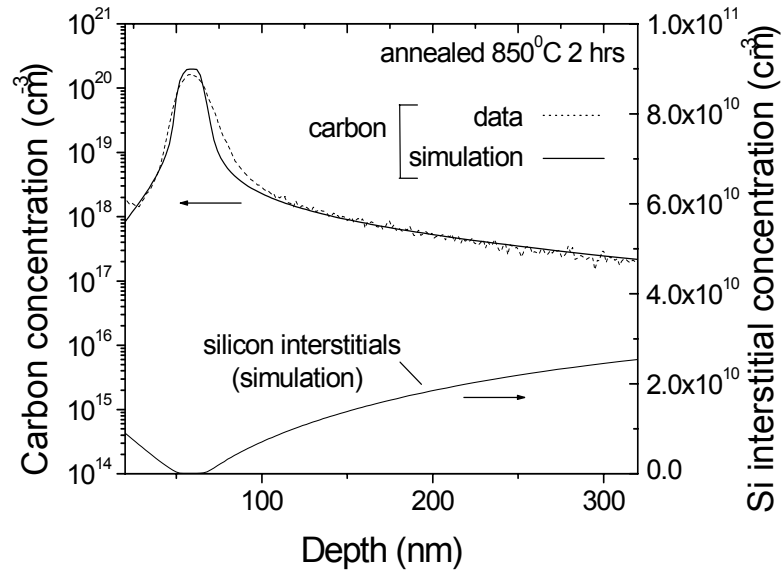


Figure 6.3: Comparison of carbon diffusion SIMS data and simulation for Si/Si_{1-y}C_y structure similar to that in Figure 5.3, except with no boron doping, annealed at 850°C for 2 hours. The fit is very good, particularly in the tail regions of the carbon profile. Note the large silicon interstitial undersaturation in the Si_{1-y}C_y region predicted by the simulation.

6.4 Boron diffusion in silicon

In this and the next section, we will show that gradients of silicon interstitial atoms, caused by gradients of substitutional carbon, can cause an effective segregation of boron atoms to regions of high substitutional carbon concentration. Note that we assume no difference in the internal energy of substitutional boron atoms between silicon and $\text{Si}_{1-y}\text{C}_y$ (or $\text{Si}_{1-x-y}\text{Ge}_x\text{C}_y$) layers, as described earlier in section 5.4.5.

6.4.1 Diffusion by interstitial mechanism

As mentioned above, boron diffusion depends on silicon interstitials in a similar manner as carbon. Substitutional boron atoms diffuse very slowly. However, similar to Equation 6.1, substitutional boron (B_S) can react with silicon self-interstitials (I) to form mobile boron-interstitial pairs, or boron "interstitialcies" (B_I) [8]:



These mobile interstitialcies then diffuse and dissociate as illustrated in Figure 6.2.

It is typically assumed that this reaction and its inverse occur much faster than the diffusion process, and hence can always be considered in equilibrium [9]:

$$k_B B_S I = B_I \quad (6.10)$$

where k is a reaction constant. Since the boron interstitialcies dominate the diffusion process, the diffusion flux of boron atoms F_B is given by:

$$F_B = -D_{BI} \frac{dB_I}{dx} = -D_{BI} \frac{d(kIB_s)}{dx} \quad (6.11)$$

where Equation 6.10 was substituted in for the boron interstitialcy concentration, and D_{BI} is their diffusivity. Normalizing the silicon interstitial concentration by its equilibrium value I_0 , an equilibrium diffusivity D_{B0} can be defined as:

$$D_{B0} = -D_{BI} k I_0 \quad (6.12)$$

Assuming that only a small fraction of boron atoms are paired with interstitials ($B_{Total} = B_S + B_I \sim B_S$), the boron flux can then be expressed as:

$$F_B = -D_{B0} \frac{d}{dx} \left(\frac{I}{I_0} B_{Total} \right) \quad (6.13)$$

If the concentration of silicon interstitials (I) is assumed to be uniform with position, it can be taken out of the derivative, and the diffusivity becomes:

$$D_B = D_{B0} \frac{I}{I_0} \quad F_B = -D_B \frac{dB}{dx} \quad (6.14)$$

where $B=B_{\text{Total}}$. In this case, the diffusivity depends directly on the concentration of silicon interstitials. This is very similar to the carbon case. If it is enhanced, as in the case of oxidation enhanced diffusion (OED)[10] or transient enhanced diffusion (TED)[11], boron diffusion increases dramatically. If it is decreased, diffusion decreases dramatically. Indeed, boron diffusion has been used as a measure of the local interstitial concentration in a region [12].

It is for this reason that boron diffusion is so slow in single-crystal $\text{Si}_{1-x-y}\text{Ge}_x\text{C}_y$ layers. As shown in Figure 6.3, the interstitial concentration in a $\text{Si}_{1-y}\text{C}_y$ layer with high carbon content is extremely small. Boron atoms inside this region do not have interstitials to pair with and diffuse, and therefore move very slowly. However, as will be discussed in the next section, interstitial profiles can also have other effects on boron diffusion.

6.4.2 Boron segregation to regions of low interstitial concentration

To obtain Equation 6.14 the concentration of silicon interstitials was assumed to be uniform with position. However, as can be seen in Figure 6.3, this is not always true. At the edges of a $\text{Si}_{1-x-y}\text{Ge}_x\text{C}_y$ layer, there is a steep gradient in the silicon interstitial profile. In this case, Equation 6.13 must be expressed as [13,14]:

$$F_B = -D_{B0} \frac{I}{I_0} \frac{dB}{dx} - D_{B0} B \frac{d}{dx} \left(\frac{I}{I_0} \right) \quad (6.15)$$

The first term on the right represents the standard diffusion flux of boron, driven by gradients in boron concentration. The second term states that a flux of *boron* atoms will also result from a gradient in *interstitial* atoms, even if no gradient in boron exists. In particular, the flux will be in the direction of a negative gradient. As a result, boron will be driven from regions of high interstitial concentration to regions of low interstitial concentration - or in our case, into a $\text{Si}_{1-x-y}\text{Ge}_x\text{C}_y$ layer. This provides a mechanism to drive boron segregation into $\text{Si}_{1-x-y}\text{Ge}_x\text{C}_y$ or $\text{Si}_{1-y}\text{C}_y$ layers from Si based solely on point-defect diffusion considerations.

6.5 Modeling of boron segregation due to interstitial gradients

6.5.1 Test structure for simulations

We use the PROPHET simulations described above to quantitatively model the effect of the interstitial gradients on boron profiles. In particular, we are interested in knowing if the flux produced by the second term in Equation 6.15 is powerful enough to drive a significant amount of boron into a $\text{Si}_{1-x-y}\text{Ge}_x\text{C}_y$ layer. All of the carbon and interstitial models remained identical to those used above for Figure 6.3, and boron diffusion was added as described by the Equation 6.15, using coefficients from [15] for the equilibrium boron diffusivity D_{B0} . In particular, *no direct boron-carbon interactions were assumed*.

A test structure (not modeled after an experimental sample) was first created in the simulator, consisting of three box-shaped 20-nm $\text{Si}_{1-y}\text{C}_y$ layers of $y= 0.1, 0.2,$ and 0.4% carbon surrounded and separated by 200 nm silicon layers. All silicon and $\text{Si}_{1-y}\text{C}_y$ layers were initially doped with a uniform boron concentration of $1 \times 10^{19} \text{ cm}^{-3}$. This was then subjected to a (simulated) 850°C , 14-hour anneal. Plots of silicon interstitials and boron after the anneal are shown in Figure 6.4, with the location of the $\text{Si}_{1-y}\text{C}_y$ layers indicated by the arrows. First, it can be seen that, as expected, the carbon layers are creating large undersaturations of silicon interstitials. The magnitude of the undersaturation (compared to the adjacent silicon) increases as the carbon concentration increases, starting at $\sim 1.2\text{X}$ for 0.1% carbon and increasing to $\sim 14\text{X}$ for 0.4% carbon. Second, and most significantly, strong boron segregation to the regions of interstitial undersaturation is also observed. This increases with carbon level (due to the increasing interstitial undersaturation), starting at 1.6 for 0.1% carbon and increasing to 4.7 for 0.4% carbon. These levels are comparable to the amount of segregation we observed in both our single-crystal and polycrystalline $\text{Si}_{1-x-y}\text{Ge}_x\text{C}_y$ and $\text{Si}_{1-y}\text{C}_y$ samples, confirming that interstitials gradients alone (without any direct boron-carbon interactions) are powerful enough to drive the boron segregation. Note, however, that this is not a true equilibrium segregation effect, as it relies on the non-equilibrium process of carbon reacting with interstitials and out-diffusing. Once the carbon has finished diffusing out of the layer, the interstitial undersaturation, and hence boron segregation, will go away. Figure 6.5 shows the time dependence of the segregation. After 2 hours, both significant interstitial

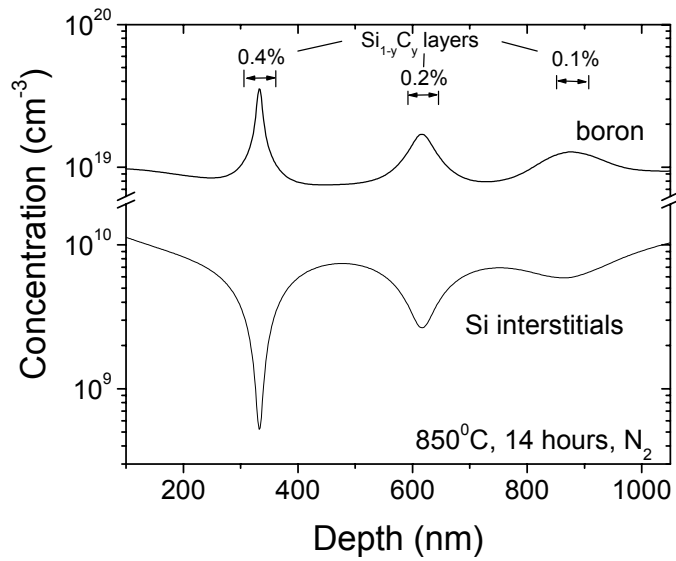


Figure 6.4: Boron and silicon interstitial profiles for the simulation test structure (not experimental data) after an 850°C, 14 hour anneal, showing strong boron segregation to the regions of low interstitial concentration.

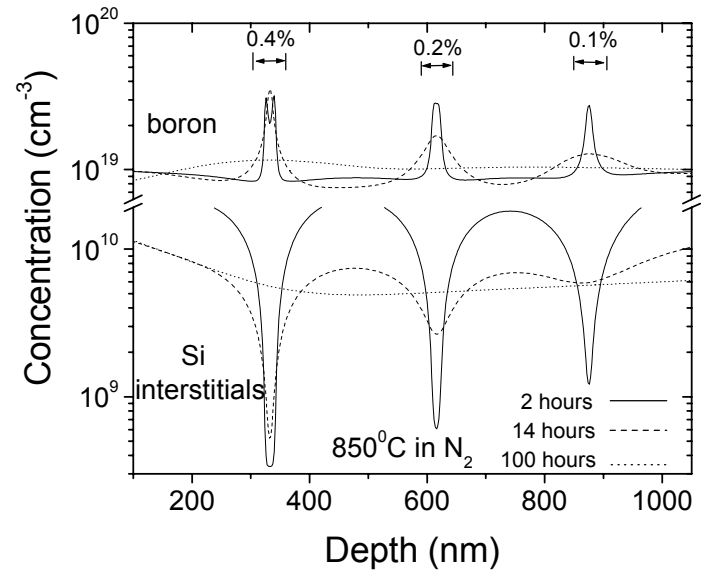


Figure 6.5: Time dependence of the boron and silicon interstitial profiles for the simulation test structure (not experimental data) after 2, 14, and 100 hour anneals at 850°C, showing the non-equilibrium nature of the segregation.

undersaturation and boron segregation have already occurred. This remains but is slightly decreased after 14 hours, and after 100 hours has almost completely gone away. This is consistent with the data from Figure 5.10, where after the carbon was removed (in this case by oxidizing the surface) most of the segregation went away.

6.5.2 Comparison of simulation with data

These simulations were then applied to model the boron profiles we measured in our experiments. Two samples were chosen for analysis: one with low carbon content (0.05%) and one with high carbon content (0.4%).

The segregation observed in Figure 5.2 for a 0.05% $\text{Si}_{1-x-y}\text{Ge}_x\text{C}_y$ layer was first simulated (800°C 18 hours). The initial boron and carbon profiles were taken from the SIMS data and used as initial conditions for the simulation. Figure 6.6 shows a comparison of the modeled and experimental boron profiles after annealing. The agreement is fairly close. These results should be interpreted with some caution, however: germanium effects (which are known to influence both boron diffusion and segregation) are not included in the simulation, nor is the effect of boron on carbon diffusion discussed on section 5.7. It is nonetheless clear, however, that interstitial gradients created by the carbon are a strong driving force for boron segregation in our samples.

The $\text{Si}/\text{Si}_{1-y}\text{C}_y$ structure from Figure 5.4 with $y=0.4\%$ was also simulated in the same manner as the previous case. Figure 6.7 shows plots of boron concentration after the 850°C 2 hour anneal, comparing data vs. simulation. The simulation again clearly

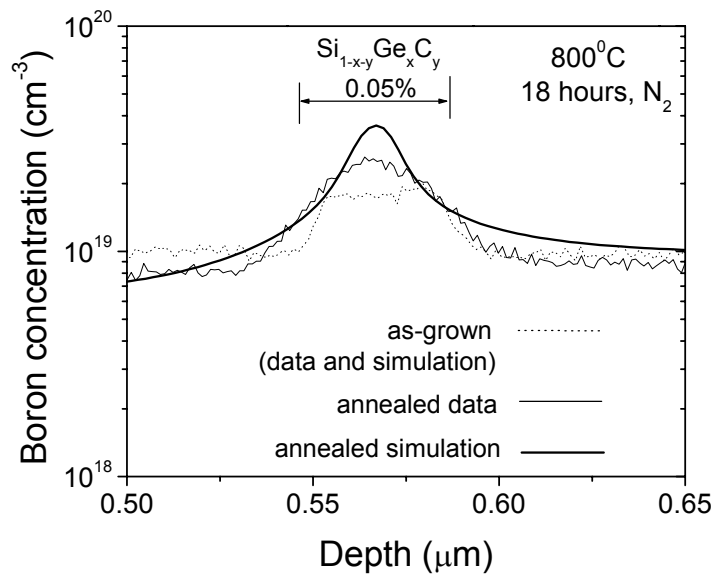


Figure 6.6: Comparison of boron segregation simulation and SIMS data for low carbon sample annealed at 800°C for 18 hours.

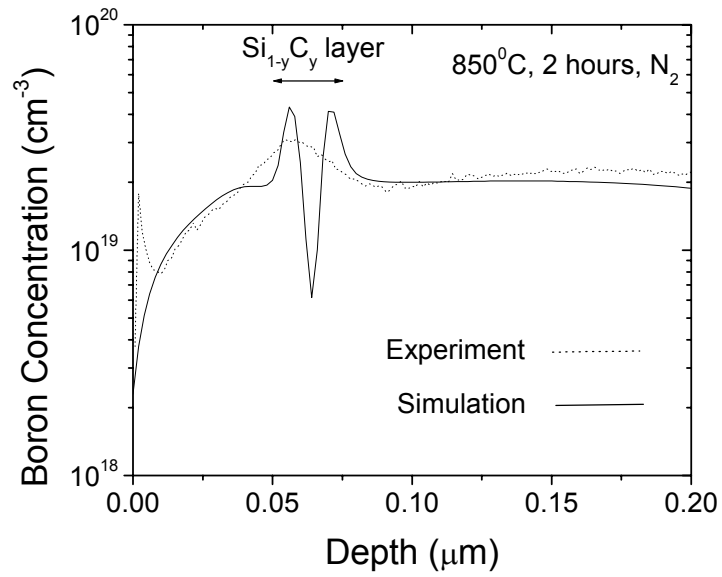


Figure 6.7: Comparison of boron segregation predicted by simulation vs. SIMS data for the high carbon sample.

shows that boron is beginning to segregate to the $\text{Si}_{1-y}\text{C}_y$ layers. However, the extremely low diffusion coefficient of the boron in the center of the $\text{Si}_{1-y}\text{C}_y$ layers prevents boron from diffusing all the way into it. The experimental data, however, shows boron segregating all the way into the layer. The discrepancy may be due to inaccuracies in the model parameters, or due to the effects of boron on carbon diffusion (and hence the interstitial profiles) discussed in Chapter 5, which are not accounted for in the model. In addition, in the experiment the true boron profiles might not be as uniformly distributed as the data appears due to broadening in the SIMS measurement.

6.6 Relevance of interstitial gradient models for boron segregation in polycrystalline layers

The segregation seen in polycrystalline $\text{Si}/\text{Si}_{1-x-y}\text{Ge}_x\text{C}_y$ structures in Chapter 4 is qualitatively similar to that studied here for single-crystal material. As a result, we would like to be able to conclude that the segregation in polycrystalline material is driven by the same interstitial gradient mechanism described in the previous section. Diffusion in polycrystalline material, however, differs from single-crystal material, most notably because of grain boundary effects. It therefore becomes less clear how effective the interstitial gradients seen in single-crystal silicon are in driving boron segregation to polysilicon. One critical issue is whether interstitial oversaturations or undersaturations have been observed in polysilicon, and whether these interstitials affect neighboring regions by moving along and/or across grain boundaries.

With regard to this question, several authors have observed excess interstitials being generated in polysilicon by both oxidation [16] and ion-implantation [17], and that they can travel through material of similar thickness as the layers used in this thesis (hundreds of nanometers) and affect boron diffusion in neighboring regions. As a result, it appears that silicon interstitial gradients can be created in polycrystalline silicon in a similar manner as in single-crystal silicon. However, further work is needed before we can clearly conclude that interstitial gradients are the main physical effect driving segregation in polycrystalline material. In particular, whether these gradients effect boron redistribution in a similar manner as in single-crystal silicon is not entirely known. For example, fast diffusion along grain boundaries could work against segregation. This and the interstitial transport issues will all depend on the microstructure of the layers – for example, whether there is a columnar grain structure in which single grains go across the layer boundaries through the entire film.

6.7 Summary

For the first time, silicon interstitial gradients have been shown to be a strong driving force for boron segregation to $\text{Si}_{1-x-y}\text{Ge}_x\text{C}_y$ and $\text{Si}_{1-y}\text{C}_y$ layers. PROPHET simulations, based on established diffusion theory for boron and carbon in silicon, show that they can drive segregation comparable to that seen in experiment. Good agreement with the data from Chapter 5 is seen at low carbon levels in $\text{Si}_{1-x-y}\text{Ge}_x\text{C}_y$; however, for higher carbon levels in $\text{Si}_{1-y}\text{C}_y$, while segregation is predicted, diffusion profiles are more difficult to match. Other effects, such as the effect of boron on carbon diffusion, may

have to be considered for a complete model of the system. Based on other known phenomena, there is a reasonable basis to expect silicon interstitial gradients to be responsible for segregation in polycrystalline material as well.

6.8 References

- [1] H. Bracht, N.A. Stolwijk, and H. Mehrer, *Physical Review B*, vol. 52, p 16542 (1995).
- [2] G. Davies and R.C. Newmann, "Carbon in Monocrystalline Silicon", in *Handbook on Semiconductors*, T.S. Moss, Ed., 1994, p. 1558.
- [3] R. Scholz, U. Gosele, J-Y. Huhm and T.Y. Tan, *Applied Physics Letters*, vol. 72(2), p. 200-202 (1998).
- [4] M.S. Carroll, Ph.D. Thesis, Princeton University (2001).
- [5] M. R. Pinto, D.M. Boulin, C.S. Rafferty, R.K. Smith, W.M. Coughran, I.C. Kizilyalli, and M.J. Thoma, *Tech. Dig. Int. Electron Devices Meeting*, p. 923-926 (1992).
- [6] R. F. Scholz, U. Gosele, J.Y. Huh, and T.Y. Tan, *Applied Physics Letters*, vol. 74, p. 392 (1999).
- [7] H. Bracht, E.E. Haller, and R. Clark-Phelps, *Physical Review Letters*, vol. 81, p. 393 (1998).
- [8] G.D. Watkins, *Physical Review B*, vol. 12, p 5824 (1975).
- [9] H. Rucker, B. Heinemann, W. Ropke, R. Kurps, D. Kruger, G. Lippert, and H.J. Osten, *Applied Physics Letters*, vol. 73 (12), p. 1682-1684 (1998).
- [10] H.-J. Gossmann, T.E. Haynes, P.A. Stolk, D.C. Jacobson, G.H. Gilmer, J.M. Poate, H.S. Luftman, T.K. Mogi, and M.O. Thompson, *Applied Physics Letters*, vol. 71(26), p. 3862-3864 (1997).
- [11] P.A. Stolk, H.-J. Gossmann, D.J. Eaglesham, D.C. Jacobson, C.S. Rafferty, G.H. Gilmer, M. Jaraiz, J.M. Poate, H.S. Luftman, and T.E. Haynes, *Journal of Applied Physics*, vol. 81(9), p. 6031-6050 (1997).
- [12] M.S. Carroll, J.C. Sturm, and T. Buyuklimanli, *Physical Review B*, vol. 64, 085316 (2001).
- [13] C.S. Rafferty, H.-H. Vuong, S.A. Eshraghi, M.D. Giles, M.R. Pinto, and S.J. Hillenius, *IEDM Technical Digest*, p. 311-314 (1993).
- [14] S.M. Hu, *Materials Science and Engineering R – Reports*, vol. 13 (3-4), p. 105-192 (1993).
- [15] Fair, R.B., *Impurity Doping Processes in Silicon*, ed. F.F.Y. Wang, Amsterdam: North Holland (1981).
- [16] D. Tsoukalas and D. Kouvatsos, *Applied Physics Letters*, vol. 68(11), p. 1549-1551 (1996).
- [17] A. Berthold, A. vom Felde, M. Biebl, and H. von Philipsborn, *Tech. Dig. Int. Elec. Dev. Mtg.*, 1994, p. 509-512.

Chapter 7: Conclusion

7.1 Summary

As the dimensions of modern silicon-based devices continue to shrink, the ability to make extremely sharp doping profiles that are stable throughout the fabrication process becomes essential. The introduction of small amounts of substitutional carbon to silicon or $\text{Si}_{1-x}\text{Ge}_x$ provides a very attractive means to control unwanted diffusion and increase device performance. In this work, we demonstrated that polycrystalline $\text{Si}_{1-x-y}\text{Ge}_x\text{C}_y$ gate layers can substantially reduce unwanted boron penetration out of the gates in scaled p-channel MOSFETs. Devices with polycrystalline $\text{Si}_{1-x-y}\text{Ge}_x\text{C}_y$ gate layers have substantially improved threshold voltage stability compared to conventional silicon or $\text{Si}_{1-x}\text{Ge}_x$ -gated devices, and comparable device performance. Boron segregation to the polycrystalline $\text{Si}_{1-x-y}\text{Ge}_x\text{C}_y$ gate layers appears to be the dominant mechanism for the reduced boron out-diffusion from the gate.

In order to integrate polycrystalline and single-crystal $\text{Si}_{1-x-y}\text{Ge}_x\text{C}_y$ and $\text{Si}_{1-y}\text{C}_y$ alloys into modern devices, an understanding of dopant diffusion and segregation effects is needed. As a result, the segregation of boron into $\text{Si}_{1-x-y}\text{Ge}_x\text{C}_y$ and $\text{Si}_{1-y}\text{C}_y$ alloys was studied in detail. Boron was shown to segregate to both polycrystalline and single-crystal $\text{Si}_{1-x-y}\text{Ge}_x\text{C}_y$ and $\text{Si}_{1-y}\text{C}_y$, revealing that neither germanium or grain boundaries are needed for it to occur. In addition, the electrical properties of both polycrystalline and single-crystal films are stable with annealing, indicating electrically inactive carbon-related defects are not driving the segregation. This is fortuitous for device applications.

Segregation to single-crystal $\text{Si}_{1-y}\text{C}_y$ is also largely reversible, indicating that the boron is not becoming immobilized at defects (i.e. SiC precipitates). A new mechanism for dopant segregation into $\text{Si}_{1-x-y}\text{Ge}_x\text{C}_y$ films, that of silicon interstitial gradients, was presented and found capable of driving segregation comparable to that seen in experiment. This discovery may also be relevant for other dopants that diffuse by similar mechanisms.

7.2 Future work

Much of the work studying diffusion in $\text{Si}_{1-x-y}\text{Ge}_x\text{C}_y$ alloys has involved studying how carbon affects boron diffusion. However, in this work we found that boron can also have an impact on carbon diffusion - in particular, it appears to enhance both its diffusion and precipitation. This is an important effect to study, as high levels of boron and carbon are often found together in devices (i.e. in the base of an HBT) and carbon precipitation is known to have deleterious effects on devices. TEM measurements are needed to look for enhanced carbon clustering in the presence of boron to confirm if this is happening. It will also be important to understand the dependence of this effect on boron doping level and annealing conditions (i.e. oxidation) to determine if this could negatively impact devices. From a theoretical standpoint, the effects of boron on carbon diffusion are important for developing a full model of diffusion in $\text{Si}_{1-x-y}\text{Ge}_x\text{C}_y$ alloys. For example, as seen in Chapter 6, these effects appear necessary to accurately predict boron segregation to $\text{Si}_{1-y}\text{C}_y$ layers. Ultimately, a full coupled diffusion/reaction model

including silicon interstitials, vacancies, carbon, and boron (with extrinsic enhancement effects) will be necessary.

Finally, while it is clear how silicon interstitial gradients can drive boron segregation in single-crystal material, further work is needed to model this effect in polycrystalline material. In particular, how the grain boundaries affect the interstitial populations and the transport of interstitials between grains must be determined. Experimental work is also needed to determine whether boron diffusion depends on silicon interstitials in a similar manner as in single-crystal silicon, and how this is impacted by the grain boundaries and microstructure of the polycrystalline films.

Appendix A: Growth Conditions for Alloy Layers Used in This Thesis

Recipe	Temp. (°C)	Press. (Torr)	Gas Flow Rates (sccm)				Ge% C%	Growth rate (nm/min)	B ₂ H ₆ flow rate (sccm)	[B] (cm ⁻³)		
			H ₂	DCS	SiH ₄ (10% in Ar)	Si ₂ H ₆ (10% in H ₂)					GeH ₄ (0.8% in H ₂)	SiCH ₆ (1% in H ₂)
Si:1	750	6	3000	26	0	0	0	0	0	11	30 ppm in H ₂	2.5x10 ¹⁹
Si:2	700	6	3000	0	100	0	0	0	0	10	5	1.0x10 ¹⁹
											10	2.5x10 ¹⁹
											25	5.5x10 ¹⁹
Si:3	625	6	3000	0	0	50	0	0	0	23	200	7.0x10 ²⁰
SiGe:1	625	6	3000	26	0	0	100	0	0	6	0.5	2.0x10 ¹⁷
											5	4.0x10 ¹⁸
											50	3.4x10 ¹⁹
											100	6.0x10 ¹⁹
SiGe:2	625	6	3000	0	100	0	100	0	0	10	10	5.0x10 ¹⁹
SiGeC:1	625	6	3000	26	0	0	100	0-10	20	6	0.5	3.0x10 ¹⁷
											5	4.0x10 ¹⁸
											50	4.0x10 ¹⁹
SiGeC:2	625	6	3000	0	100	0	100	0-10	27	10	0.5	2.0x10 ¹⁸
											5	2.0x10 ¹⁹
											10	6.0x10 ¹⁹
SiC:1	625	10	3000	0	0	50	0	20-40	0.4-1.0	23	200	7.0x10 ²⁰

Appendix B: Sample RTCVD Growth Sequences

B.1. Polycrystalline Si/Si_{0.8765}Ge_{0.12}C_{0.0035} gate structure

Wafer # 2830, structure shown in Figure 3.2(a). Deposited on 7 nm gate oxide.

Comments: Dichlorosilane used to grow top ~ 200 nm of the gate to minimize use of silane, which deposits more readily on the chamber quartz tube.

SEQUENCER TABLE # 0

0	CONTROL ON&	Turn on control
1	SCAN(0.3)	and Scan simultaneously
2	SET(SP7,0)&	Lamp power = zero
3	SEP(SP4,0)&	Lamp(PID) control off
4	SET(SP0,0.6)	Zero loop counter
5	SET(DO0,0)&	
6	SET(DO1,0)&	H ₂ select off
7	SET(DO2,1)&	SiH ₄ select on
8	SET(DO3,1)&	GeH ₄ select on
9	SET(DO4,0)&	B ₂ H ₆ select off
10	SET(DO5,0)&	PH ₃ select off
11	SET(DO7,1)&	DCS select on
12	SET(DO6,1)&	SiCH ₆ select on
13	SET(DO9,0)&	SiH ₄ inject off
14	SET(DO10,0)&	GeH ₄ inject off
15	SET(DO11,0)&	B ₂ H ₆ inject off
16	SET(DO12,0)&	PH ₃ inject off
17	SET(DO13,0)&	DCS/Si ₂ H ₆ inject off
18	SET(DO14,0)&	SiCH ₆ inject off
19	SET(AO0,0.61)	H ₂ flow = 3 lpm
20	SET(DO15,1)	Vacuum On
21	SET(DO1,1)&	Hydrogen Select On
22	SET(AO1,0.16)&	SiH ₄ flow = 100 sccm
23	SET(AO2,0.21)&	GeH ₄ flow = 100 sccm
24	SET(AO3,0.0)&	B ₂ H ₆ high flow = 0 sccm
25	SET(AO14,0.0)&	B ₂ H ₆ low flow = 0 sccm
26	SET(AO4,0.0)&	PH ₃ high flow = 0 sccm
27	SET(AO5,0.0)&	PH ₃ low flow = 0 sccm
28	SET(AO6,0.534)&	DCS flow = 26 sccm
29	SET(AO7,0.4)&	SiCH ₆ flow = 4 sccm
30	SET(AO8,0.0)&	Pump out
31	SEQUENCER ON(0.3,1,0)	Start sequence #1

SEQUENCER TABLE # 1

0	SET(SP1,1)&	Set layer number
1	SET(SP2,0.0)&	Reset loop number
2	SEQUENCER ON(0.3,6,0)	Call cleaning sequence
3	WAITUNTIL(SP2>0.5)	Cleaning sequence
4	SET(SP2,0.0)	Reset loop counter
5		
6	SEQUENCER ON(0.3,5,0)	Call poly layers sequence
7	WAITUNTIL(SP2>0.5)	Poly layers sequence
8	SET(SP2,0.0)	Reset loop counter
9		
10	SET(SP4,0.0)	Lamp(PID) control off
11	RAMP(SP7,-0.4,0.0)	Ramp lamps to zero
12	SEQUENCER ON(0.3,7,0)	Call reload sequence
13	SET(SP2,0.0)	Reset loop counter
14	END	End
15		
16		
17		
18		
19		
20		
21		
22		
23		
24		
25		
26		
27		
28		
29		
30		
31		

SEQUENCER TABLE # 5

0	WAITUNTIL(AI24>0.5)	Press GO for poly layers
1		
2	SET(SP5,3.51)	Set temp = 700 deg C
3	SET(SP4,1.0)	Turn lamp(PID) control on
4	WAIT(60)	Wait 1 minute to stabilize
5		
6	SET(DO9,1)	SiH4 inject on
7	WAIT(10)	Growing wetting layer
8	SET(DO9,0)	SiH4 inject off
9		
10		
11	SET(SP5,2.85)	Set temp = 625 deg C
12	WAIT(30)	wait 30 sec
13	SET(DO9,1)	SiH4 inject on
14	SET(DO10,1)	GeH4 inject on
15	SET(DO14,1)	SiCH6 inject on
16	WAIT(250)	Growing poly SiGeC layer
17	SET(DO10,0)	GeH4 inject off
18	SET(DO14,0)	SiCH6 inject off
19	SET(DO3,0)	GeH4 select off
20	SET(DO6,0)	SiCH6 select off
21	SET(SP5,3.51)	Set temp = 700 deg C
22	WAIT(210)	Growing SiH4 poly Si layer
23	SET(DO9,0)	SiH4 inject off
24	SET(DO2,0)	SiH4 select off
25	SET(SP5,4.23)	Set temp = 750 deg C
26	SET(DO13,1)	DCS inject on
27	WAIT(1800)	Growing DCS poly Si layer
28	SET(DO13,0)	DCS inject off
29	SET(DO7,0)	DCS select off
30		
31	SET(SP2,1.0)	Reset loop control

SEQUENCER TABLE # 6

0	WAITUNTIL(AI24>0.5)	Press GO for cold values
1	SET(SP3,1)	Get cold value
2	WAIT(1)	Wait 1 second
3	SET(SP3,0)	Latch cold values
4		
5	SET(AO8,0.6)	Set pressure = 6 Torr
6	WAITUNTIL(AI28>0.55)	Pressure stabilizing
7		
8	RAMP(SP7,0.4,0.18)	Ramp lamps to 18%
9	WAIT(120)	Wait 2 minutes
10		
11	SET(SP2,1.0)	Reset loop control
12		
13		
14		
15		
16		
17		
18		
19		
20		
21		
22		
23		
24		
25		
26		
27		
28		
29		
30		
31		

SEQUENCER TABLE # 7

0	SET(SP7,0)	Lamps off
1	SET(DO13,0)&	DCS inject off
2	SET(DO12,0)&	PH3 inject off
3	SET(DO11,0)&	B2H6 inject off
4	SET(DO10,0)&	GeH4 inject off
5	SET(DO9,0)&	SiH4 inject off
6	SET(DO14,0)&	SiCH6 inject off
7	SET(DO6,0)&	SiCH6 select off
8	SET(DO7,0)&	DCS select off
9	SET(DO5,0)&	PH3 select off
10	SET(DO4,0)&	B2H6 select off
11	SET(DO3,0)&	GeH4 select off
12	SET(DO2,0)&	SiH4 select off
13	SET(DO1,0)	H2 select off
14	SET(AO8,0.0)	Pump out
15	SET(AO7,0.0)&	SiCH6 flow = 0.0 sccm
16	SET(AO6,0.0)&	DCS flow = 0.0 sccm
17	SET(AO14,0.0)&	B2H6 low flow = 0.0 sccm
18	SET(AO3,0.0)&	B2H6 high flow = 0.0 sccm
19	SET(AO2,0.0)&	GeH4 flow = 0.0 sccm
20	SET(AO1,0.0)&	SiH4 = 0.0 sccm
21	SET(AO0,0.0)&	H2 flow = 0.0 lpm
22	WAITUNTIL(AI28<0.5)	Pump out
23	SET(DO15,0)	Vacuum off
24	SEQUENCER OFF(0)	Sequencer 0 off
25	SEQUENCER OFF(1)	Sequencer 1 off
26	SEQUENCER OFF(2)	Sequencer 2 off
27	SEQUENCER OFF(3)	Sequencer 3 off
28	SEQUENCER OFF(4)	Sequencer 4 off
29	SEQUENCER OFF(5)	Sequencer 5 off
30	SEQUENCER OFF(6)	Sequencer 6 off
31	SEQUENCER OFF(7)	Sequencer 7 off

B.2. Single-crystal Si/Si_{0.996}C_{0.004}/Si segregation structure

Wafer # 3360, structure shown in Figure 5.3(a).

Comments: The high flow phosphine control was used for flowing high diborane flows, due to problems with the diborane control cable.

SEQUENCER TABLE # 0

0	CONTROL ON&	Turn on control
1	SCAN ON(0.3)	and Scan simultaneously
2	SET(SP7,0)&	Override power to zero
3	SEP(SP4,0)&	Turn off PID control
4	SET(SP0,0.6)	Zero loop counter
5	SET(DO0,0)&	N2 select off
6	SET(DO1,0)&	H ₂ select off
7	SET(DO2,0)&	SiH ₄ select off
8	SET(DO3,0)&	GeH ₄ select off
9	SET(DO4,1)&	B ₂ H ₆ select on
10	SET(DO5,0)&	PH ₃ select off
11	SET(DO6,1)&	SiCH ₆ select on
12	SET(DO7,1)&	DCS select on
13	SET(DO8,0)	Si ₂ H ₆ select off
14	SET(DO9,0)&	SiH ₄ inject off
15	SET(DO10,0)&	GeH ₄ inject off
16	SET(DO11,0)&	B ₂ H ₆ inject off
17	SET(DO12,0)&	PH ₃ inject off
18	SET(DO13,0)&	DCS/Si ₂ H ₆ inject off
19	SET(AO0,0.21)	H ₂ flow = 1 slpm
20	SET(DO15,1)	Vacuum On
21	SET(DO1,1)&	Hydrogen Select On
22	SET(AO1,0.0)&	SiH ₄ flow = 0 sccm
23	SET(AO2,0.0)&	GeH ₄ flow = 0 sccm
24	SET(AO14,0.0)&	B ₂ H ₆ low flow = 0 sccm
25	SET(AO4,0.2)&	B ₂ H ₆ high flow = 100 sccm
26	SET(AO5,0.0)&	PH ₃ low flow = 0 sccm
27	SET(AO6,0.534)&	DCS flow = 26 sccm
28	SET(AO7,0.2)&	SiCH ₆ flow = 20 sccm
29	SET(AO8,0.0)&	Pump out
30	SEQUENCER ON(0.3,1,0)	Start sequence #1
31		

SEQUENCER TABLE # 1

0	SET(SP1,1)&	Set layer number
1	SET(SP2,0.0)&	Reset loop number
2	SEQUENCER ON(0.3,6,0)	Call cleaning sequence
3	WAITUNTIL(SP2>0.5)	Cleaning sequence
4	SET(SP2,0.0)	Reset loop control
5		
6	SEQUENCER ON(0.3,5,0)	Call buffer layer sequence
7	WAITUNTIL(SP2>0.5)	Buffer layer sequence
8		
9	SET(SP5,4.29)	Set temp = 750 deg C
10	SET(SP4,1.0)	Feedback on
11	SET(SP2,0.0)	Reset loop control
12	WAIT(30)	Stabilize
13	SET(DO11,1)	B2H6 inject on
14	WAIT(900)	Growing Si layer 1
15	SET(DO11,0)	B2H6 inject off
16		
17	SET(SP5,2.93)	Set temp = 625 deg C
18		
19		
20	SEQUENCER ON(0.3,4,0)	Call SiC layer sequence
21	WAITUNTIL(SP2>0.5)	SiC layer sequence
22	SET(SP2,0.0)	Reset loop control
23		
24	SET(SP4,0.0)	Feedback off
25	RAMP(SP7,-0.4,0.0)	Loop check
26	SEQUENCER ON(0.3,7,0)	Call reload sequence
27		
28		
29		
30		
31		

SEQUENCER TABLE # 4

0	SET(AO8,1.0)	Pressure = 10 Torr
1	SET(DO13,0)	DCS inject off
2	SET(DO7,0)	DCS select off
3	WAIT(15)	Close DCS manual valve
4	SET(DO8,1)	Si2H6 select on
5	SET(AO15,0.5)	Si2H6 flow = 50 sccm
6	WAIT(45)	Open Si2H6 manual valve
7		
8	SET(DO13,1)	Si2H6 inject on
9	WAIT(20)	
10	SET(DO14,1)	SiCH6 inject on
11	WAIT(45)	
12	SET(DO14,0)	SiCH6 inject off
13	SET(DO6,0)	SiCH6 select off
14	WAIT(20)	
15	SET(DO13,0)	Si2H6 inject off
16	SET(DO8,0)	Si2H6 select off
17	WAIT(15)	Close Si2H6 manual valve
18	SET(DO7,1)	DCS select on
19	SET(AO6,0.534)	DCS flow = 26 sccm
20	WAIT(15)	Open DCS manual valve
21	SET(AO8,0.6)	Pressure = 6 Torr
22	SET(SP5,4.29)	Set temp = 750 deg C
23	SET(DO13,1)	DCS inject on
24	SET(DO11,1)	B2H6 inject on
25	WAIT(240)	Growing cap layer
26	SET(DO13,0)	DCS inject off
27	SET(DO7,0)	DCS select off
28	SET(DO11,0)	B2H6 inject off
29	SET(DO4,0)	B2H6 select off
30	SET(SP2,1.0)	
31	END	

SEQUENCER TABLE # 5

0		
1	WAITUNTIL(AI24>0.5)	Press GO for buffer layer
2	SET(AO11,1)	Low pressure select
3		
4	SET(AO8,0.6)	Set pressure = 6 Torr
5	WAITUNTIL(AI28>0.55)	Pressure stabilizing
6		
7		
8		
9	SET(DO13,1)	DCS inject on
10	WAIT(300)	Growing buffer layer 1
11	SET(DO13,0)	DCS inject off
12		
13		
14		
15	RAMP(SP7,-0.4,0.0)	Lamps off
16	WAITUNTIL(AI24>0.5)	Press GO for cold values
17		
18		
19	SET(SP3,1)	Get cold values
20	WAIT(1)	
21	SET(SP3,0)	Latch cold values
22	RAMP(SP7,0.4,0.27)	ramp lamps to 27%
23	WAIT(30)	Reheat wafer
24	SET(DO13,1)	inject DCS
25	WAIT(60)	
26		
27		
28		
29	RAMP(SP7,-0.4,0.20)	Lamps down to 20%
30	WAIT(15)	Si at 20%
31	SET(SP2,1.0)	Reset loop control

SEQUENCER TABLE # 6

0	WAITUNTIL(AI24>0.5)	Press GO for clean
1	SET(AO11,0)&	High pressure select
2	SET(AO8,0.25)	Pressure = 250 Torr
3	SET(AO0,0.817)&	H2 flow = 4 lpm
4	WAITUNTIL(AI29>250)	Pressure stabilize
5		
6		
7		
8		
9		
10		
11		
12		
13		
14		
15		
16		
17	RAMP(SP7,0.4,0.27)	Ramp lamps to 27%
18	WAIT(120)	2 minute clean
19	SET(AO8,0.22)	Pump out gradually
20	WAIT(10)	
21	SET(AO8,0.17)	
22	WAIT(10)	
23	SET(AO8,0.12)	
24	WAIT(10)	
25	SET(AO8,0.07)	
26	WAIT(10)	
27	SET(AO8,0.0)	
28	SET(AO0,0.61)	H2 flow = 3 lpm
29		
30		
31	SET(SP2,1.0)	Reset loop control

SEQUENCER TABLE # 7

0	SET(SP7,0)	Lamps off
1	SET(DO13,0)&	DCS inject off
2	SET(DO12,0)&	PH3 inject off
3	SET(DO11,0)&	B2H6 inject off
4	SET(DO10,0)&	GeH4 inject off
5	SET(DO9,0)&	SiH4 inject off
6	SET(DO7,0)&	DCS select off
7	SET(DO5,0)&	PH3 select off
8	SET(DO4,0)&	B2H6 select off
9	SET(DO3,0)&	GeH4 select off
10	SET(DO2,0)&	SiH4 select off
11	SET(DO1,0)	H2 select off
12	SET(AO8,0.0)	Pump out
13	SET(AO7,0.0)&	SiCH6 flow = 0.0 sccm
14	SET(AO6,0.0)&	DCS flow = 0.0 sccm
15	SET(AO5,0.0)&	PH3 low flow = 0.0 sccm
16	SET(AO4,0.0)&	B2H6 high flow = 0.0 sccm
17	SET(AO14,0.0)&	B2H6 low flow = 0.0 sccm
18	SET(AO2,0.0)&	GeH4 flow = 0.0 sccm
19	SET(AO1,0.0)&	SiH4 = 0.0 sccm
20	SET(AO0,0.0)&	H2 flow = 0.0 lpm
21	WAITUNTIL(AI28<0.5)	Pump out
22	SET(DO15,0)	Vacuum off
23		
24	SEQUENCER OFF(0)	Sequencer 0 off
25	SEQUENCER OFF(1)	Sequencer 1 off
26	SEQUENCER OFF(2)	Sequencer 2 off
27	SEQUENCER OFF(3)	Sequencer 3 off
28	SEQUENCER OFF(4)	Sequencer 4 off
29	SEQUENCER OFF(5)	Sequencer 5 off
30	SEQUENCER OFF(6)	Sequencer 6 off
31	SEQUENCER OFF(7)	Sequencer 7 off

Appendix C: Publications and Presentations Resulting From This Thesis

Journal Articles

1. E. J. Stewart, M. S. Carroll, and J. C. Sturm, "Boron Segregation in Single-Crystal $\text{Si}_{1-x-y}\text{Ge}_x\text{C}_y$ and $\text{Si}_{1-y}\text{C}_y$ alloys", submitted to *Journal of the Electrochemical Society*.
2. E. J. Stewart, M. S. Carroll, and J. C. Sturm, "Boron Segregation and Electrical Properties in Polycrystalline $\text{Si}_{1-x-y}\text{Ge}_x\text{C}_y$ and $\text{Si}_{1-y}\text{C}_y$ alloys", to be published in *Journal of Applied Physics* (2004).
3. E.J. Stewart, M.S. Carroll, and J.C. Sturm, "Suppression of Boron Penetration in P-Channel MOSFETs Using Polycrystalline $\text{Si}_{1-x-y}\text{Ge}_x\text{C}_y$ Gate Layers", *IEEE Electron Devices Letters*, vol. 22(12), pp. 574-576 (2001).

Refereed Conference Papers

1. E.J. Stewart and J.C. Sturm, "Boron Segregation and Out-Diffusion in Single-Crystal $\text{Si}_{1-y}\text{C}_y$ ", *Materials Research Society Symposium Proceedings*, vol. 765, p. 223-228 (2003).
2. E.J. Stewart and J.C. Sturm, "Boron Segregation to Polycrystalline and Single-Crystal $\text{Si}_{1-x-y}\text{Ge}_x\text{C}_y$ and $\text{Si}_{1-y}\text{C}_y$ ", to be published in *Applied Surface Science*.
3. E.J. Stewart, M.S. Carroll, and J.C. Sturm, "Boron Segregation and Electrical Properties in Polycrystalline $\text{Si}_{1-x-y}\text{Ge}_x\text{C}_y$ ", *Materials Research Society Symposium Proceedings*, vol. 669, J6.9 (2001).
4. E.J. Stewart, M.S. Carroll, C.L. Chang, and J.C. Sturm, "Threshold Voltage Stability of P-channel MOSFETs with Heavily Boron-Doped $\text{Si}_{1-x-y}\text{Ge}_x\text{C}_y$ Gate Layers", *ULSI Process Integration II*, C.L. Claeys, F. Gonzalez, J. Murota, and K. Saraswat (eds.), The Electrochemical Society, Inc., pp. 519-532 (2001).
5. (Invited) J.C. Sturm, M.S. Carroll, M. Yang, J. Gray, and E.J. Stewart, "Mechanisms and Applications of the Control of Dopant Profiles in Silicon Using $\text{Si}_{1-x-y}\text{Ge}_x\text{C}_y$ Layers Grown by RTCVD", *Proceedings of the Electrochemical Society*, vol. 2000-9, p. 309-320 (2000).

Conference Presentations

1. E.J. Stewart and J.C. Sturm, "Boron Segregation and Out-Diffusion in Single-Crystal $\text{Si}_{1-y}\text{C}_y$ ", Materials Research Society Spring Meeting, San Francisco, CA, April 2003.
2. E.J. Stewart and J.C. Sturm, "Boron Segregation to Polycrystalline and Single-Crystal $\text{Si}_{1-x-y}\text{Ge}_x\text{C}_y$ and $\text{Si}_{1-y}\text{C}_y$ ", International SiGe Technology and Device Meeting, Nagoya, Japan, January 2003.
3. E.J. Stewart, M.S. Carroll, and J.C. Sturm, "Boron Segregation and Electrical Properties in Polycrystalline $\text{Si}_{1-x-y}\text{Ge}_x\text{C}_y$ ", Materials Research Society Spring Meeting, San Francisco, CA, April 2001.
4. E.J. Stewart, M.S. Carroll, C.L. Chang, and J.C. Sturm, "Threshold Voltage Stability of P-channel MOSFETs with Heavily Boron-Doped $\text{Si}_{1-x-y}\text{Ge}_x\text{C}_y$ Gate Layers", 199th Meeting of the Electrochemical Society, Washington, D.C., March 2001.
5. (Invited) J.C. Sturm, M.S. Carroll, M. Yang, J. Gray, and E.J. Stewart, "Mechanisms and Applications of the Control of Dopant Profiles in Silicon Using $\text{Si}_{1-x-y}\text{Ge}_x\text{C}_y$ Layers Grown by RTCVD", Electrochemical Society Meeting, Toronto, Canada, May 2000.
6. E.J. Stewart, C.L. Chang, M.S. Carroll, and J.C. Sturm, "Boron segregation in Polycrystalline $\text{Si}_{1-x-y}\text{Ge}_x\text{C}_y$ Alloys", 41st Electronic Materials Conference, Santa Barbara, CA, June 1999.